https://doi.org/10.15388/vu.thesis.202
https://orcid.org/0000-0002-6249-2181

VILNIUS UNIVERSITY
CENTER FOR PHYSICAL SCIENCES AND TECHNOLOGY

Darya
MEISAK

Hybrid multifunctional composites with nanoinclusions and structures for electromagnetic applications

DOCTORAL DISSERTATION

Technological sciences,
Materials Engineering (T 008)

VILNIUS 2021

This dissertation was written between 2017 and 2021 at Vilnius University.

Academic supervisor:

Dr. Jan Macutkevic (Vilnius University, Technological sciences, Materials Engineering, T 008).

This doctoral dissertation will be defended in a public meeting of the Dissertation Defence Panel:

Chairman – **Prof. Habil. Dr. Gintaras Valušis** (Center for Physical Science and Technology, Technological sciences, Materials Engineering, T 008).

Members:

Doc. Dr. Renata Butkutė (Center for Physical Science and Technology, Technological sciences, Materials engineering, T 008).

Prof. Dr. Liutauras Marcinauskas (Kaunas University of Technology, Technological sciences, Materials Engineering, T 008).

Prof. Habil. Dr. Ludmila Matzui (Kiev University in Ukraine, Technological sciences, Materials Engineering, T 008).

Doc. Dr. Tomas Šalkus (Vilnius University, Technological sciences, Materials Engineering, T 008).

The dissertation shall be defended at a public meeting of the Dissertation Defence Panel at 15.00 on 20th September 2021 at National Center for physical science and technology, B336 room.

Address: Sauletekio av. 3, Vilnius, Lithuania.

The text of this dissertation can be accessed at the libraries of Vilnius university and Center for Physical Science and Technology, as well as on the website of Vilnius University: www.vu.lt/lt/naujienos/ivykiu-kalendorius

https://doi.org/10.15388/vu.thesis.202
https://orcid.org/0000-0002-6249-2181

VILNIAUS UNIVERSITETAS
FIZINIŲ IR TECHNOLOGIJOS MOKSLŲ CENTRAS

Darya
MEISAK

Hibridiniai multifunkciniai kompozitai su nanodariniais ir struktūros elektromagnetiniams taikymams

DAKTARO DISERTACIJA

Technologiniai mokslai,
Medžiagų inžinerija (T 008)

VILNIUS 2021

Disertacija rengta 2017– 2021 metais Vilniaus universitete.

Mokslinis vadovas:

Dr. Jan Macutkevič (Vilniaus universitetas, technologiniai mokslai, medžiagų inžinerija, T 008).

Gynimo taryba:

Pirmininkas – Prof. habil. dr. Gintaras Valušis (Fizinių ir technologijos mokslų centras, technologiniai mokslai, medžiagų inžinerija, T 008).

Nariai:

Doc. dr. Renata Butkutė (Fizinių ir technologijos mokslų centras, technologiniai mokslai, medžiagų inžinerija, T 008).

Prof. dr. Liutauras Marcinauskas (Kauno technologijos universitetas, technologiniai mokslai, medžiagų inžinerija, T 008).

Prof. habil. dr. Ludmila Matzui (Kijevo universitetas, Ukraina, technologijos mokslai, medžiagų inžinerija, T 008).

Doc. dr. Tomas Šalkus (Vilniaus universitetas, technologijos mokslai, medžiagų inžinerija, T 008).

Disertacija ginama viešame Gynimo tarybos posėdyje 2021 m. rugsėjo mėn. 20 d. 15 val. Nacionalinio fizinių ir technologijų mokslų centro B336 auditorijoje.

Adresas: Saulėtelio al. 3,Vilnius, Lietuva.

Disertaciją galima peržiūrėti Vilniaus universiteto ir Fizinių ir technologijos mokslų centro bibliotekose, ir VU interneto svetainėje adresu: https://www.vu.lt/naujienos/ivykiu-kalendoriu

ACKNOWLEDGMENTS

This thesis would not have been possible without the support and help of certain people at Vilnius University and the Institute for Nuclear Problems BSU, Minsk. I will try to express my vast gratitude to each of them in a few words.

I am sincerely grateful to doctor Jan Macutkevic for the opportunity to work under his scientific supervision for four years. Thank you very much for all ideas, advice, patience, huge assistance in obtaining and interpreting the results, writing the articles and finally this thesis.

I would also like to thank professor Jūras Banys for help, support, perfect research conditions and other nice things.

Special thanks must be given to doctor Polina Kuzhir and doctor Dzmitry Bychanok for providing a great positive impact on me at the beginning of my scientific career, for their patience, continuous support, quick response to any issues, as well as for help in writing and editing the articles included in this thesis.

Thanks to my friends and colleagues I met at INP BSU: Gleb Gorokhov, Alesia Paddubskaya, Artyom Plyushch, Nadzezhda Volynets, Yaraslau Padrez, Lizaveta Shashkova for a great time spent together inside and outside the laboratory.

The great appreciation goes to my colleagues in Vilnius University (without particular order): Maksim Ivanov, Sergejus Balčiūnas, Šarūnas Svirskas, Ieva Kranauskaitė, Džiugas Jablonskas, Robertas Grigalaitis, Vidmantas Kalendra, Martynas Kinka, Dzmitry Adamchuk, Vadzim Haronin for support and friendly atmosphere in the lab.

To professor Rumiana Kotsilkova for providing printed samples.

Finally, I want to acknowledge my parents and my brother Ilya, as well as all my friends outside the scientific community for their patience and moral support.

CONTENTS

INTRODUCTION

Nanoscale objects properties investigations, their production methods, characterization, and control have been promising, intensively developing scientific direction for already several decades. One of the reasons for the great demand for nanosized particles is their ability to adjust the properties of polymers through incorporation, leading to the creation of new composite materials with enhanced desired characteristics. Moreover, the rise of the particles surface area with the reduction of their size (from micro- to nanoscale)[1,2] promotes more effective interactions between the filler particles, as well as between the intermixed phases, that favorably affects mechanical strength, thermal stability[3–6], etc.

Electrically conductive polymer composites occupy an exclusive position in composite technologies, since they can be used as structural, electronic, and sensory materials. For these purposes, an ordinary and obvious solution is to choose various nanocarbon forms as fillers, which, despite their already rather broad research history[7–10], have not been able to lose their popularity. Besides, the conductivity control ability of the final composite product through the polymer and nanocarbon filler selection, the variation of their relative content and the processing methods conditions makes the application range extremely wide: antistatic materials[11], conductive films and coatings[12,13], solar cells and biosensors[14], electromagnetic shielding materials[15–19], etc. However, nanoparticles of non-carbon origin (such as goethites, ferrites, metal particles, etc.) are also gaining interest as additives in polymer matrices. Usually, the scientists attention is focused on the magnetic and ferromagnetic properties of these materials, which have been successfully demonstrated in such application areas as magnetic recording media devices[20], ferrofluid[21], for biomedical applications (magnetic resonance imaging, tissue engineering, drug delivery, etc.)[22,23], and as electromagnetic absorbers due to magnetic losses[24–28]. Nevertheless, magnetic nanoparticles investigations in terms of electrical properties may also be interesting to make them applicable (along with very popular carbon inclusions) as conductive materials.

One of the goals of modern materials science is the development of composites with enhanced electrical conductivity accompanied by superior mechanical properties, but such requirements represent conflicting scenarios. This problem is particularly typical for nanocarbon materials, including carbon nanotubes (CNTs), despite their high aspect ratio, which is much more conducive to forming of conductive pathways in the polymer matrix at low percolation threshold[29–33]. CNTs have a tendency to agglomerate[34–36] in the

polymer due to the strong Van der Waals interactions, which translates into the need to increase their content that negatively affects the mechanical properties (the material becomes porous and weak). Alternatively, the simultaneous usage of various nanofiller combinations may be a facile and promising strategy to effectively boost the electrical properties of composites. Such manipulations consequence maybe not only a mixture of individual fillers advantages, but also the synergistic effects emergence. The properties synergy is not magic, but simply the result of preventing nanofiller agglomeration due to the favorable formation of co-supporting networks based on several types of inclusions[37,38]. Usually, the electrical properties synergy is accompanied by the percolation threshold decrease. Despite numerous studies on both carbon/carbon[35,37,39–41] and carbon/non-carbon[42–49] hybrid polymer systems, the possible activity space in this direction still remains wide.

Among a wide application range of electrically conductive composites, a significant place is occupied by microwave electromagnetic shielding and absorbing. The electromagnetic response can be manipulated not only by the selection a material with certain bulk properties, but also by the creation of structures on its basis of complex geometry, with a special individual components ordering, as well as with a functionally dependent refractive index[50,51]. With the thermoplastic polymers discovery and additive technologies[52,53] development, it has become possible to easily, quickly and economically create three-dimensional structures of different shapes[54], which opens up possibilities for the design, in particular, of microwave devices (absorbers, matched loads). For instance, the waveguide matched load, often in the form of a long wedge or pyramid[55], is a common example of a device that absorbs electromagnetic energy without reflecting the incident electromagnetic wave. The periodic pyramidal structures based on dielectric lossless materials as broadband absorbers have been extensively studied before; they are known as anechoic chambers[56–60]. However, replacing a dielectric lossless material with a conductive lossy material offers the possibility of absorbers and matched loads miniaturization.

This work is devoted to the investigation of several epoxy-based composite systems: (i) binary with different magnetic particles ($Fe_2O_3 \cdot H_2O$, $MnFe_2O_4$, Ni@C) and (ii) ternary hybrids with a combination of magnetic particles and multi-walled carbon nanotubes (MWCNTs). Experimental investigations are focused on the dielectric/electrical properties of these materials over wide frequency and temperature ranges. Besides, the robust design of compact

microwave absorbers and waveguide matched loads based on a conductive lossy composite is demonstrated.

Aims and tasks of the work

The main aim of the current work is to investigate the dielectric properties of epoxy-based binary composites with magnetic inclusions, and to find synergy effects between two fillers in ternary hybrid composite systems. Another aim is to find the relation between microwave electromagnetic response and size geometry of pyramidal periodic structure based on conductive lossy material in order to get superior shielding efficiency performance.

The tasks of the current work to achieve the aims are*:*

1. To study the dielectric properties of epoxy-based composites filled with three types of magnetic nanoparticles ($Fe_2O_3 \cdot H_2O$, $MnFe_2O_4$, Ni@C) in wide frequency and temperature ranges.
2. To study the dielectric properties of the ternary hybrid epoxy-based composite systems with MWCNTs and small additives of magnetic particles.
3. To investigate experimentally and via simulations the microwave electromagnetic response of a pyramidal periodic structure based on a conductive lossy material.

Scientific novelty

1. The dielectric properties experimental study of several epoxy-based binary composite systems with different types of magnetic nanoparticles ($Fe_2O_3 \cdot H_2O$, $MnFe_2O_4$, Ni@C) in wide frequency and temperature ranges was performed. The electrical percolation thresholds for each system were determined. The behavior features of the temperature and frequency spectra of the dielectric permittivity and electrical conductivity of the composites both below and above the percolation threshold were demonstrated and explained.
2. The dielectric properties experimental study of ternary hybrid epoxy/MWCNT/$MnFe_2O_4$ and epoxy/MWCNT/Ni@C composite systems in wide frequency and temperature ranges was performed. In both

systems, when the MWCNTs are in a pre-percolation state, at certain small amounts of the magnetic component, a pronounced electrical properties synergy was demonstrated. The observed synergy explanation through the MWCNTs dispersion improvement due to the favorable formation of a co-supporting network by two types of nanofillers was applied.

3. A pyramidal periodic structure based on conductive lossy material as an effective compact microwave absorber and waveguide matched load was considered. The shielding efficiency optimization method, which takes into account the material properties, the required frequency range, and the structure geometry, was successfully used at the pre-experimental step to evaluate the pyramids parameters. The shielding efficiency of the pyramids with the estimated optimal parameters was experimentally demonstrated as 20 dB for both reflected and transmitted signals in the microwave frequency range.

Author's contribution

The dielectric investigations presented in the thesis were performed by the author personally under the supervision of dr. Jan Macutkevic. She also produced all the epoxy-based composites in the Nanoelectromagnetics laboratory of Institute for Nuclear Problems BSU. The model for electromagnetic properties simulations of pyramidal structures was developed with dr. Dzmitry Bychanok. The published articles were written by the author with the great discussion support of J. Macutkevic, P. Kuzhir, J. Banys, D. Bychanok and other co-authors.

Statements presented for the defense

1. The percolation threshold of spherical particles in the polymer matrix can vary significantly: in the $MnFe_2O_4$/epoxy composite system, the percolation concentration is close to 30 vol.%, which is in agreement with theoretical predictions, while the Ni@C/epoxy composite system demonstrates a much lower critical fraction in the range between 10 and 15 vol.%. Polymer-filler interaction difference leads to Ni@C particle ability to form a percolation network at lower concentrations.

2. The electromagnetic properties of epoxy-based composites with MWCNTs in the pre-percolation state are significantly improved over a wide temperature range by the addition of certain small amounts of magnetic inclusions due to the enhanced particle distribution by the creation of a favorable co-supporting network.
3. The perspective of using conductive lossy materials for microwave devices miniaturization was demonstrated by the pyramidal periodic structure example. To predict the remarkable shielding efficiency, the evaluation model of the optimal geometry parameters of the pyramids (taking into account their bulk characteristics and the considered frequency range) at the pre-experimental step was proposed.

List of publications included into the thesis

1. D. Meisak, J. Macutkevic, D. Bychanok, A. Selskis, J. Banys, P. Kuzhir, Broadband dielectic properties of Fe_2O_3 H_2O nanorods/epoxy resin composites, Journal of Nanomaterials 2019 (2019), 9756920.
2. D. Meisak, J. Macutkevic, A. Selskis, J. Banys, P. Kuzhir, Dielectric properties and electrical percolation in $MnFe_2O_4$/epoxy resin composites, Physica Status Solidi (a) 217(6) (2019), 1900526.
3. D. Meisak, J. Macutkevic, A. Plyushch, P. Kuzhir, A. Selskis, J. Banys, Dielectric relaxation in the hybrid epoxy/MWCNT/$MnFe_2O_4$ composites, Polymers 12(3) (2020), 697.
4. D. Meisak, E. Gurnevich, A. Plyushch, D. Bychanok, V. Georgiev, R. Kotsilkova, P. Kuzhir, Robust design of compact microwave absorbers and matched loads based on DC-conductive 3D-printable filament, Journal of Physics D: Applied Physics 53(30) (2020), 305301.
5. D. Meisak, J. Macutkevic, A. Selskis, P. Kuzhir, J. Banys, Dielectric relaxation spectroscopy and synergy effects in epoxy/MWCNT/Ni@C composites, Nanomaterials 11(2) (2021), 555.

List of conference presentations

1. Dielectric properties of Fe_2O_3 H_2O/Epoxy resin composites. D. Meisak, J. Macutkevic, D. Bychanok, G. Gorokhov, P. Kuzhir, Multi-Functional Nano-Carbon Composites Materials Network – 2018, March 8-9, Vilnius, Lithuania.

2. Broadband investigations of dielectric properties Fe_2O_3 H_2O/epoxy resin composites. D. Meisak, J. Macutkevic, D. Bychanok, G. Gorokhov, P. Kuzhir, Modern Multifunctional Composites – 2018, May 11, Vilnius, Lithuania.
3. Electromagnetic properties of Fe_2O_3 H_2O-based polymer materials. D. Meisak, J. Macutkevic, D. Bychanok, G. Gorokhov, P. Kuzhir, Fundamental and applied nanoelectromagnetics – 2018, June 5-7, Minsk, Belarus.
4. Dielectric properties of epoxy resin composites based on magnetic nanoparticles. D. Meisak, J. Macutkevic, J. Banys, Nanomeeting – 2019, May 21-24, Minsk, Belarus.
5. Synergy effects in hybrid MWCNT/$MnFe_2O_4$/epoxy resin composites. D. Meisak, J. Macutkevic, J. Banys, P. Kuzhir, Polymer composites and tribology – 2019, June 25-28, Gomel, Belarus.
6. The $MnFe_2O_4$ nanoparticles effect on dielectric properties of multiwall carbon nanotube based epoxy resin composites. D. Meisak, J. Macutkevic, J. Banys, P. Kuzhir, MultiComp – 2019, September 12-13, Prague, Czech Republic.
7. The $MnFe_2O_4$ nanoparticles influence on the dielectric properties of multiwall carbon nanotube based epoxy resin composites. D. Meisak, J. Macutkevic, J. Banys, Interaction of radiation with solids – 2019, September 30 – October 3, Minsk, Belarus.
8. Dielectric properties of hybrid MWCNT/$MnFe_2O_4$/epoxy resin composites. D. Meisak, J. Macutkevic, J. Banys, P. Kuzhir, Lietuvos Nacionalinė Fizikos Konferencija – 2019, October 3-5, Kaunas, Lithuania.
9. The manganese ferrite effect on dielectric propertis of MWCNT-based epoxy resin composites. D. Meisak, J. Macutkevic, J. Banys, P. Kuzhir, Functional Materials and Nanotechnologies – 2020, November 23-26, Vilnius, Lithuania.

Other papers

1. D. Bychanok, G. Gorokhov, D. Meisak, A. Plyushch, P Kuzhir, A. Sokal, K. Lapko, A. Sanchez-Sanchez, V. Fierro, A. Celzard, C. Gallagher, A. P. Hibbins, F. Y. Ogrin, C. Brosseau, Exploring carbon nanotubes/$BaTiO_3$/Fe_3O_4 nanocomposites as microwave absorbers, Progress In Electromagnetic Research 66 (2016), 77-85.

2. D. Bychanok, G. Gorokhov, D. Meisak, P. Kuzhir, S. Maksimenko, Y. Wang, Z. Han, X. Gao, H. Yue, Design of carbon nanotube-based broadband radar absorber for Ka-band frequency range, Progress in electromagnetic research M 53 (2017), 9-16.
3. D. Bychanok, S. Li, G. Gorokhov, K. Piasotski, D. Meisak, P. Kuzhir, E. A. Burgess, C. P. Gallagher, F. Y. Ogrin, A. P. Hibbins, A. Pasc, A. Sanchez-Sanchez, V. Fierro, A. Celzard, Fully carbon metasuface: Absorbing coating in microwaves, Journal of Applied Physics 121(16) (2017), 165103.
4. D. Bychanok, A. Liubimau, K. Piasotski, G. Gorokhov, D. Meisak, I. Bochkov, P. Kuzhir, Effective carbon nanotube/phenol formaldehyde resin based double-layer absorbers of microwave radiation: design and modeling, Physica Status Solidi B 255(1) (2018), 1700224.
5. D. Bychanok, P. Angelova, A. Paddubskaya, D. Meisak, L. Shashkova, M. Demidenko, A. Plyushch, E. Ivanov, R. Krastev, R. Kotsilkova, F. Y. Ogrin, P. Kuzhir, Teraherz absorption in graphite nanoplatelets/polylactic acid composites, Journal of Physics D: Applied Physics 51(14) (2018), 145307.
6. G. Spinelli, P. Lamberti, V. Tucci, R. Kotsilkova, S. Tabakova, R. Ivanova, P. Angelova, V. Angelov, E. Ivanov, R. Di Maio, C. Silvestre, D. Meisak, A. Paddubskaya, P. Kuzhir, Morphological, rheological and electromagnetic properties of nanocarbon/poly(lactic) acid for 3D printing: solution blending vs. melt mixing, Materials 11(11) (2018), 2256.
7. M. Shuba, D. Yuko, G. Gorokhov, D. Meisak, D. Bychanok, P. Kuzhir, S. Maksimenko, P. Angelova, E. Ivanov, R. Kotsilkova, Frequency and density dependencies of the electromagnetic parameters of carbon nanotube and graphene nanoplatelet based composites in the microwave and terahertz ranges, Materials Research Express 6(9) (2019), 095050.
8. G. Spinelli, P. Lamberti, V. Tucci, R. Kotsilkova, E. Ivanov, D. Menseidov, C. Naddeo, V. Romano, L. Guadagno, R. Adami, D. Meisak, D. Bychanok, P. Kuzhir, Nanocarbon/poly(lactic) acid for 3D printing: effect of fillers content on electromagnetic and thermal properties, Materials 12(15) (2019), 2369.

1. LITERATURE OVERVIEW

1.1 Complex parameters of the medium

The state of excitation which is established in space by the presence of electric charges is said to constitute an electromagnetic field. It is represented by two vectors: the electric vector $\vec{E}$ and the magnetic induction $\vec{B}$. To describe the effect of the field on matter, it is necessary to introduce the second set of vectors: the electric current density $\vec{j}$, the electric displacement $\vec{D}$, and the magnetic vector $\vec{H}$. Then these five vectors listed above are interconnected by Maxwell's equations, which in the case of an isotropic medium in the SI units have the following form[61,62]:

$$rot\vec{H} = \vec{j} + \frac{\partial \vec{D}}{\partial t} \tag{1.1}$$

$$rot\vec{E} = -\frac{\partial \vec{B}}{\partial t} \tag{1.2}$$

$$div\vec{D} = \rho \tag{1.3}$$

$$div\vec{B} = 0 \tag{1.4}$$

$$\vec{j} = \sigma\vec{E} \tag{1.5}$$

$$\vec{D} = \varepsilon_a\vec{E} \tag{1.6}$$

$$\vec{B} = \mu_a\vec{H} \tag{1.7}$$

where ρ is the electric charge density, σ is the electric conductivity; ε_a is the absolute dielectric permittivity; μ_a is the absolute magnetic permeability. Let's introduce the relative permittivity ε and permeability μ as $\varepsilon_a = \varepsilon\varepsilon_0$ and $\mu_a = \mu\mu_0$, respectively, where ε_0 and μ_0 are the permittivity and permeability of the vacuum, respectively.

In the case of charges absence (ρ=0), using Maxwell's equations (1.1)-(1.7), one can obtain the wave motion equations for each field vector separately by excluding the remaining vectors. Thus, the wave motion equation for the $\vec{E}$ vector has the following form (the wave motion equation for the $\vec{H}$ vector has a similar form):

$$\nabla^2\,\vec{E} = \varepsilon_a\mu_a\frac{\partial^2\vec{E}}{\partial t} + \mu_a\,\sigma\frac{\partial\vec{E}}{\partial t} \tag{1.8}$$

The search of a solution of Equation (1.8) is carried out as a plane harmonic wave of a complex form, which in the case of its propagation along the x axis with a v velocity takes the form:

$$\vec{E} = \vec{\mathcal{E}}\exp[i\omega(t - x/v)] \tag{1.9}$$

where $\vec{\mathcal{E}}$ is the vector amplitude and ω is the angular frequency of this wave.

For equation (1.9) to be a solution of equation (1.8), the following condition must be satisfied:

$$\frac{\omega^2}{v^2} = \omega^2 \varepsilon_a \mu_a - i\omega\mu_a\sigma \quad (1.10)$$

For the case of vacuum ($\sigma = 0$, $v = c$), equation (1.10) is transformed into the:

$$c^2 = 1/\varepsilon_0\mu_0 \quad (1.11)$$

Multiplying equation (1.10) by equation (1.11) and dividing by ω^2, it turns out the following:

$$n^2 = \frac{c^2}{v^2} = \frac{\varepsilon_a\mu_a}{\varepsilon_0\mu_0} - i\frac{\mu_a\sigma}{\omega\varepsilon_0\mu_0} = \varepsilon\mu - i\frac{\mu\sigma}{\omega\varepsilon_0} = (n' - in'')^2 = \varepsilon^*\mu^* \quad (1.12)$$

where n is the dimensionless parameter of the medium, which is known as the complex refractive index, n' is the real part of the refractive index, n'' is the imaginary part of the refractive index (or the extinction coefficient). The $\varepsilon^* = \varepsilon - i\frac{\sigma}{\omega\varepsilon_0} = \varepsilon' - i\varepsilon''$ is the complex dielectirc permittivity; $\mu^* = \mu' - i\mu''$ is the complex permeability.

Taking into account (1.12), equation (1.9) for a plane harmonic wave takes the form:

$$\vec{E} = \vec{\mathcal{E}}\exp\left[i\omega t - i\frac{2\pi n}{\lambda}x\right] = \vec{\mathcal{E}}\exp\left[-\frac{2\pi n''}{\lambda}x\right]\exp\left[i\omega t - i\frac{2\pi n'}{\lambda}x\right] \quad (1.13)$$

where $\lambda = 2\pi c/\omega$ is the wavelength, and the significance of n'' emerges as being a measure of the absorption in the medium.

1.2 Electromagnetic response simulation of multi-layered systems by matrix method

The normal incidence of an electromagnetic wave on a plane-parallel layer of material is accompanied by its successive reflections from each boundary (two boundaries in the case of one layer), and the layer properties are determined by the summation of these waves. The consideration is limited to thin layers, when the path difference between the beams is less than the radiation wavelength (the long-wave approach). Using the Maxwell's equations (Equations (1.1)-(1.7)) directly can give the values of the electric and magnetic fields at the boundaries of the layer. If the electromagnetic waves are plane in form according Equation (1.9), then these fields can be represented in matrix notation as follows[61,62]:

$$\begin{bmatrix} E_1 \\ H_1 \end{bmatrix} = \begin{bmatrix} \cos(k\tau) & i\frac{k_0}{k}sin(k\tau) \\ i\frac{k}{k_0}sin(k\tau) & \cos(k\tau) \end{bmatrix} \begin{bmatrix} E_2 \\ H_2 \end{bmatrix} \quad (1.14)$$

where E_1, H_1 and E_2, H_2 are the electric and magnetic fields at the first and second boundaries of the layer with thickness of τ; k and k_0 are the wavenumbers inside the layer with refractive index n (according Equation (1.12)) and in air (refractive index $n_0 = 1$). In the case of free space, the wavenumbers are written as $k = \frac{2\pi n}{\lambda}$ and $k_0 = \frac{2\pi n_0}{\lambda}$, while inside a waveguide system of width a, they are defined in the form: $k = \frac{2\pi}{\lambda a}\sqrt{n^2a^2 - \frac{\lambda^2}{4}}$ and $k_0 = \frac{2\pi}{\lambda a}\sqrt{n_0^2a^2 - \frac{\lambda^2}{4}}$, where ν is the frequency; $c = 3 \cdot 10^8$ m/s is vacuum light speed. The first term in the right part of Equation (1.14) is known as the characteristic matrix of the layer.

The result obtained can easily be transformed to the case of two or more layers placed sequentially one after the other (multi-layered system). In the case of a N-layer system, the characteristic matrix of the whole structure is simply the product of the individual matrices of each layer taken in the correct order. Then the reflection R and transmission T coefficients of such structure take the form:

$$R = S_{11}^2 = \frac{(n_0 - \frac{C}{B})^2}{(n_0 + \frac{C}{B})^2} \quad (1.15)$$

$$T = S_{21}^2 = \frac{4n_0^2}{(n_0 + \frac{C}{B})^2} \quad (1.16)$$

where

$$\begin{bmatrix} B \\ C \end{bmatrix} = \left\{ \prod_{t=1}^{N} \begin{bmatrix} \cos(k_t\tau) & i\frac{k_0}{k_t}sin(k_t\tau) \\ i\frac{k_t}{k_0}sin(k_t\tau) & \cos(k_t\tau) \end{bmatrix} \right\} \begin{bmatrix} 1 \\ n_0 \end{bmatrix} \quad (1.17)$$

and S_{11} and S_{21} are the relative amplitudes of the reflected and transmitted signals, respectively. Equation (1.17) is the particular case with the refractive index of air n_0 in the right part, but generally this refractive index corresponds to the last layer.

The long-wave approach method described above can be useful in the case of the electromagnetic response simulations of more complex structures. Having performed the homogenization procedure for such structures, they can be considered as multi-layered systems with a spatially distributed refractive index[63,64]. The homogenization procedure means the refractive indices averaging in each infinitely thin layer of multi-layered system[51,65].

1.3 Percolation theory

Percolation theory is the simplest, not exactly solved model for multiphase materials description[66,67]. This theory found broadest application as a powerful tool to describe of the physical properties of heterogeneous materials. Dramatic changes in the physical properties of a heterogeneous medium (e.g. composite material) occur when filler particles form a percolating network (by coming into contact with each other) throughout the system, particularly when the difference between the properties of the constitutive phases is large. This happens when the volume fraction p of filler particles (minor phase) approaches a critical value p_c called the percolation threshold. The behaviour of the conductivity versus inclusions volume fraction close to the percolation threshold of the conducting constituent is defined by the following laws[19,68–72]:

$$\begin{cases} \sigma = \sigma_1 (p_c - p)^{-s}, & p < p_c \\ \sigma = \sigma_2 (p - p_c)^{t}, & p > p_c \end{cases} \tag{1.18}$$

where s and t are critical exponents; σ_1 is the electrical conductivity of the insulating matrix and σ_2 is the electrical conductivity of inclusions. Since the percolation model is independent of the nature of the filler particles and the nature of the insulating host matrix, it can be applied to most polymers filled with different kind of electrically conductive inclusions.

The behaviour of the dielectric permittivity near the percolation threshold is also extraordinary[71,73,74] and is given by the following power law[66,68,71,72,75,76]:

$$\varepsilon' \propto (p_c - p)^{-t} \tag{1.19}$$

A qualitative interpretation of this phenomenon may be as follows. Near the percolation threshold the conducting clusters are separated by thin dielectric regions. Each pair of the nearest clusters forms a capacitor whose effective surface tends to infinity near the percolation threshold. Then the effective capacity of the system also diverges. These factors can contribute to the enhancement of the dielectric permittivity of the systems near the percolation threshold.

1.4 Maxwell-Wagner relaxation

The dipole relaxation analogue for heterogeneous materials (particularly for composites based on insulating matrices and conducting inclusions) is Maxwell-Wagner relaxation[77–80]. In this case, the polarization mechanism consists in the accumulation of moving charge carriers at the interfacial boundaries under the external electric field. Such a spatial redistribution of charge carriers strongly affects the overall polarizability of the material, and, therefore, the latter can exhibit a very large effective dielectric permittivity.

One of the possible way to describe Maxwell-Wagner relaxation is the impedance formalism, in frame of which the complex impedance $Z^* = Z' - iZ''$ is determined as follows[81,82]:

$$Z^* = \frac{1}{i\omega\varepsilon_0\varepsilon^*} = \frac{1}{i\omega\varepsilon_0(\varepsilon' - i\varepsilon'')} = \left(\frac{\varepsilon''}{\varepsilon'^2 + \varepsilon''^2} - i\frac{\varepsilon'}{\varepsilon'^2 + \varepsilon''^2}\right)\frac{1}{\omega\varepsilon_0} \quad (1.20)$$

where the real (Z') and imaginary (Z'') parts of Z^* are separately expressed as

$$Z' = \frac{\varepsilon''}{\varepsilon'^2 + \varepsilon''^2}\frac{1}{2\pi\nu\varepsilon_0} \quad (1.21)$$

$$Z'' = \frac{\varepsilon'}{\varepsilon'^2 + \varepsilon''^2}\frac{1}{2\pi\nu\varepsilon_0} \quad (1.22)$$

The complex impedance of heterogeneous systems with Maxwell-Wagner relaxation cannot be described using a single RC-circuit (a capacitor C and a resistor R connected in series), when the relaxation time would be determined by the simple expression $\tau = RC$. Instead, the Z^* spectra need to be modelled by an infinite chain of RC circuits connected in series. Then the relaxation time distribution $f(\tau)$ can be found using the Tikhonov regularization technique.

1.5 Relaxation time distribution determination

In an external electric field, the polarization, and hence relaxation time distribution of the heterogeneous system depends on system constituent components, their shape, size, and dispersion in the matrix (the agglomerates presence). Therefore, the relaxation time distribution function $f(\tau)$, as well as $f(\tau)$ versus temperature can provide very valuable information about collective phenomena in composites.

The procedure used for calculating the relaxation time distribution is described in detail in[83,84]. In short, it consists in solving an integral equation with known frequency dependence of the complex impedance $Z^*(\omega)$:

$$Z^*(\omega) = Z_\infty + \Delta Z \int_{-\infty}^{\infty} \frac{f(\tau)}{1+i\omega\tau} d(\lg \tau) \quad (1.23)$$

where Z_∞ is the impedance at the high-frequency limit, ΔZ is difference between the static impedance (low frequency impedance) and the high-frequency limit of impedance.

The method of solving integral equation (1.23) is the discretization and Tikhonov regularization. The first step - discretization - consists in transforming the integral equation (1.23) to the linear non-homogeneous algebraic equations set. Since the number of equations in this set exceeds the number of variables, it cannot be solved directly. Thereby, the second step is necessary: the introduction of a minimization condition according to the Tikhonov regularization procedure. The regularization parameter α appears, which is responsible for smoothing noisy data. Then finding a truthful relaxation time distribution $f(\tau)$ is reduced to the correct determination of regularization parameter α, besides, the limiting of the minimization problem by fixing the static impedance and/or the high-frequency limit of impedance can also help.

1.6 Hybrid composites systems

A composite material (or composite) is a heterogeneous system consisting of two or more distinct phases with a pronounced interphase boundary[85]. This intentional combination of several constituents leads to a new material that can exhibit properties that do not necessarily appear in the individual components. If the number of phases is more than two, the hybrid composite definition is introduced. In the case of polymer hybrid composites, they are systems, where two or more types of fillers are placed in a single matrix or one filler is introduced to a mixture of different matrices[86–88]. Obviously, in hybrid composites, a combination of various properties, as well as their synergy effects due to the favorable distribution of particles and the interaction between them, can be expected[37]. Mixing inorganic or organic fillers origin of different geometrical features, such as shape, size, and aspect ratio, allows obtaining composites with controlled desired properties. Fillers may assume a geometrical form of fibers, flakes, rods, platelets, spheres, and other irregular particles[89]. A schematic illustration of a unique network based on two fillers of different geometries responsible for the properties synergy in a hybrid composite is shown in Figure 1.1.

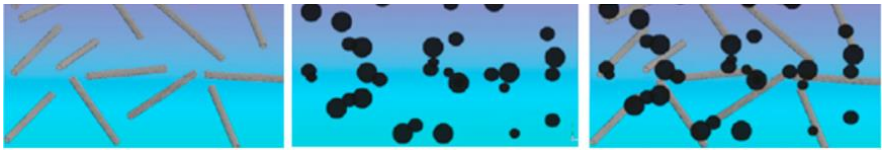

a b c

Figure 1.1: Schematic illustration of the network in (a,b) composites with one filler and (c) hybrid composite[90].

By comparison with monofiller system, hybrid composites have the following main advantages[86,90]:

1. Improving filler dispersion;
2. Forming hybrid filler networks with better filler-filler connection/interaction;
3. Lowering the percolation threshold;
4. Improving mechanical[91,92], piezoresistive properties and thermal conductivities[35,93];

The existence of synergy between different types of fillers, inorganic or organic, shows great potential and could significantly increase applications of such nanomaterials.

1.6.1 Synergy definition

The definition of "synergy" can be introduced as a deviation from the simple rule of mixtures[94], since the early theoretical treatments of the hybrid effect according to this rule showed a contradiction with the experimental results[95]. Rule of mixtures is given by a mathematical expression that describes the property of a heterogeneous composite as the sum of the weighted volume average of the component properties in isolation[96]:

$$\bar{\rho} = \frac{1}{(\sum_{i=0}^{n} V_i)} \sum_{i=0}^{n} \rho_i V_i \qquad (1.24)$$

where $\bar{\rho}$ is the homogenized property of interest, V_i is the corresponding volume of the part that has the specific property ρ_i.

However, the rule of mixtures does not take into account the interfacial adhesion between the filler and the matrix, as well as the interaction of fillers, therefore it cannot be used directly to predict the properties of the hybrid

composite. In each case for a hybrid composite, the experimental results should be considered. A positive hybrid effect (synergy) occurs when the real properties of the composite are better than the values calculated from the rule of mixtures, whereas a negative hybrid effect corresponds to the opposite situation. Thus, synergy takes place in the case of the elements set whose combination gives a total effect that is greater than the sum of the effects of the individual elements (elements increase the effectiveness of each other in combination).

1.6.2 The occurrence mechanisms of electrical conductivity synergy in ternary systems

In electrical conductivity point of view in ternary systems, synergy is achieved through the use of two conductive fillers with distinct geometric shapes, aspect ratios, and individual conductivity values. The synergy of electrical properties is accompanied by the decrease of the percolation threshold compared to monofiller systems. Even if one of the fillers is insulating or poorly conductive, the percolation threshold may decrease due to the volume exclusion effect[97,98] and the improved dispersion of the second highly conductive filler[99]. Reviewing numerous researches[86,90,100] in this area, the following conclusion can be done: a filler with a large aspect ratio (i.e. the main filler) has priority in the formation of a network of conductive pathways at content close to its percolation threshold in monofiller case, while another filler acting as a "spacer" is able to improve the dispersion of the main filler in the matrix.

In this regard, to understand the mechanisms of synergy effects in the ternary composite containing one filler with a large aspect ratio (such as fibers or rods) and the second filler with a much smaller one (such as sphere or platelets), two theoretical situations are possible.

The first case consists in a significant change of the network structure of the first filler by the second one. A fractal-like structure of the first filler (e.g. carbon nanotubes - CNTs) is equipped with many redundant shoulders in the network that do not contribute to the effective conductive pathway (so-called "dead" branches). It means only a certain amount of MWCNTs are involved in charge transport. The addition of the second filler aggregates leads to the formation of new conductive pathways between "dead" MWCNT branches. Since the tunneling distance between CNTs determines the total conductivity in the monofiller CNTs/polymer composites[101], an increase in the conductivity

of the CNTs-based hybrid composite can be a direct result of the reduction of the tunneling distances due to the placement of a second filler between carbon nanotubes[39].

The second case occurs when the second filler is incorporated into the conductive "active" CNT pathways, then the final conductivity should mainly be preserved or decreased. An exception is a situation when the CNTs are in a pre-percolation state, then the putting of the second filler between them can contribute to the final conducting network formation.

1.6.3 Electrical percolation theory in ternary composites

The change in the electrical conductivity with increasing concentrations of the electrically conducting filler is nonlinear and described by the classical percolation theory (see subchapter 1.3). However, for hybrid (ternary) composites with two different filler types, Equation (1.18) is no longer valid to describe the relation between the percolation threshold and each filler concentration. A new theoretical model based on the excluded volume theory has been proposed[102]. According to this model, the percolation thresholds of each kind of filler in the corresponding monofiller (binary) composites obey the following relation[102]:

$$\frac{V_A}{p_c^A} + \frac{V_B}{p_c^B} = 1 \qquad (1.25)$$

where V_A and V_B are the volume fractions of filler A and B, respectively; and. p_c^A and p_c^B are the percolation thresholds of filler A and B in the corresponding monofiller composites, respectively. Equation (1.25) indicates that if its left part is equal to 1, the conductive fillers begin to percolate in the matrix; if its left part is greater than 1, the conductive fillers combine with each other, and the material becomes conductive; if its left part is less than 1, the fillers separately disperse in the matrix, and percolative network is absent. The considered model has been repeatedly successfully applied to composites with various systems of mixed fillers[102–106]. Equation (1.25) can be used for predicting the electrical properties of ternary composites with two fillers, providing that the percolation concentrations for the corresponding monofiller systems are known. Moreover, for the convenience of practical use, the volume fraction can be generalized as the weight fraction.

However, a lot of experimental researches show the occurrence of the percolation even if the left part of Equation (1.25) is less than 1[40,86,107,108]. In

this case, when the percolation occurs at concentrations lower than predicted by Equation (1.25), the synergy effect of electrical properties takes place.

1.7 Magnetic nanoparticles as additives in polymers for electromagnetic shielding applications: recent progress

Magnetic nanoparticles (such as goethite $Fe_2O_3 \cdot H_2O$ nanorods, manganese ferrite $MnFe_2O_4$, Ni@C core-shell nanoparticles, etc.) and polymer composites on their basis are usually interesting from magnetic and ferromagnetic properties point of view, therefore have already found numerous applications[21–23,109,110]. However, investigations of these particles in terms of electrical properties can also be interesting, because it allows to expand the application range, in particular, to use them as conductive materials too. For this reason, it is important to determine the electrical percolation threshold of polymer composite systems filled with magnetic nanoparticles. Moreover, due to the combination of magnetic and dielectric losses, such materials can be promising for electromagnetic shielding applications.

Investigations of polymer composites with goethite ($Fe_2O_3 \cdot H_2O$) nanorods are rare enough[111], however, due to high nanorods aspect ratio, they can be attractive in shielding area similarly to iron nanowires[112,113] or iron fibers[114,115]. Yang et al[112] showed that epoxy-based composites filled with iron nanowires of high concentrations exhibit superior absorption properties (>97% of incident power at few mm of thickness) in microwave 7-14 GHz frequency range compared to composites with iron nanoparticles. Wu et al[114] investigated the microwave (2.60-3.95 GHz) dielectric and magnetic losses of composites with iron fibers in epoxy resin matrix depending on the fiber diameter: both types of losses decrease with increasing fiber diameter (or decreasing aspect ratio). Moreover, Wu et al[115] showed the reflection coefficient of 1.0 mm-thick epoxy-based sample with 20 vol.% of iron fibers: less than -8 dB in 9.7-14.5 GHz and less than -5 dB in the 8-18 GHz frequency ranges.

Manganese ferrite ($MnFe_2O_4$) is an excellent inorganic candidate for the role of magnetic inclusions in polymer composites due to its electrical, optical, magnetic, and catalytic properties[116]. Magnetic properties (in particular, the saturation magnetization, the ferrimagnetic to paramagnetic transition) of manganese ferrite depend on particle sizes[117,118], their forms[119,120] and, for

example, modifications by carbon[22,121]. Moreover, $MnFe_2O_4$-based polymer composites both monofiller[122–125] and hybrid[126–128] cases have already demonstrated a high level of electromagnetic shielding performance. Chakraborty et al[122] got the results of -8 dB for a reflection loss at 10.5 GHz for nano-size manganese ferrite reinforced conductive polypyrrole composites. Lakshmi et al[123] considered the composite system based on manganese ferrite, chemically modified with polymethyl methacrylate and polyaniline, and demonstrated the value of shielding efficiency due to the transmittance as -44 dB in 8-12 GHz frequency range. According to Hosseini et al[124,125] investigations, composites based on manganese ferrite in polyaniline matrix show a minimum reflection loss of -15.3 dB at 10.4 GHz, while in polypyrrole matrix – around -12 dB at 11.3 GHz (sample thickness in both cases is close to 1.5 mm). Reduced graphene oxide – manganese ferrite hybrids with multiwalled carbon nanotubes inside polyvinylidene fluoride matrix demonstrated high absorption and a total electromagnetic shielding of -38 dB at 18 GHz as reported in[126].

Carbon-coated Ni nanoparticles (Ni@C), being superparamagnetic or ferromagnetic, are also promising for the design of microwave absorbing devices due to the presence of magnetic losses[27,28]. According to the study of Zhang et al[28,129], the composites based on carbon-coated Ni nanocapsules inside paraffin matrix demonstrate the maximum reflection loss of -32 dB at 13 GHz with 2 mm in thickness. Wu et al[130] investigated microwave absorption properties of paraffin-based composites with carbon-coated nickel nanocapsules depending on particles size: sample with the average particle size of 25 nm exhibits reflection loss value of -32 dB at 11.6 GHz, and with increase particle size the reflection loss decreases. High microwave absorption of Ni/Graphitic carbon core-shell powder in elastomeric rubber matrix was also demonstrated by Saini et al[131]: the sample with the highest content of 70 wt.% shows reflection loss value of -48 dB at 17 GHz at the thickness of 1 mm. Similar polymer-based composite systems filled with such as carbon-coated Co[132,133], Mg[134], Fe[135,136] nanoparticles have also exhibited significant attenuation of microwave electromagnetic radiation.

2. EXPERIMENTAL TECHNIQUE

2.1 Dielectric permittivity measurements

2.1.1 Low frequency range (20 Hz - 1 MHz)

In the low frequency range, the most common used method of the dielectric permittivity measurements is the plane parallel capacitor method. The method is based on comparison of the capacitor capacitance filled with sample and the capacitance of an empty capacitor[80,137]. By measuring the capacitance (C) and loss tangent ($tg\delta = \varepsilon''/\varepsilon'$) of the sample, the dielectric permittivity can be recalculated using the following formulas:

$$\begin{cases} \varepsilon' = \frac{(C_s - C_0)d}{\varepsilon_0 S} + 1 \\ tg\delta = \frac{C_s tg\delta_s - C_0 tg\delta_0}{C_s - C_0} \end{cases} \quad (2.1)$$

where C_s and $tg\delta_s$ are the capacitance and tangent losses of the system with the sample, C_0 and $tg\delta_0$ are the capacitance and tangent losses of the system without the sample, d is the distance between the capacitor plates (sample thickness), S is the area of the sample, ε_0 is the dielectric permittivity of vacuum.

Low frequency (20 Hz – 1 MHz) measurements of the complex dielectric permittivity were performed using LCR HP4284A meter. For heating mode (300 – 500 K) in all experiments a home made furnace was used, for cooling mode (25 – 300 K) closed-cycle cryostat or liquid nitrogen were used. All temperature measurements were performed with a heating/cooling rate of around 1 K/min. The silver paste was used to improve the contacts between electrodes and the sample.

At higher frequencies, the measurement system errors become significant, and therefore the described above method is no longer suitable.

2.1.2 Coaxial line technique (1 MHz - 3 GHz)

The coaxial line method is the most convenient method for the dielectric measurements in the 1 MHz – 3 GHz frequency range. The coaxial dielectric spectrometer based on vector network analyzer Agilent 8714ET capable of complex reflection coefficient R^* measurement was used. The small samples were placed at the end of the coaxial line between the inner conductor and the short piston, which formed a capacitor[138].

The complex reflection coefficient is related to the impedance of the sample by the following equation:

$$R^* = \frac{Z_s^* - Z_0}{Z_s^* + Z_0} \quad (2.2)$$

where R^* is the complex reflection coefficient, Z_S^* is the complex impedance of the sample, Z_0 is the impedance of the transmission line (50 Ω).

In the quasi-static case, when the electric field is homogeneously distributed inside the sample (the dielectric permittivity of the sample is low), the plane capacitor model is applicable[138]. In the frame of this model, the relation between impedance and capacitance of the plane capacitor is as follows:

$$Z_S^* = \frac{1}{i\omega C^*} = \frac{d}{i\omega \varepsilon^* \varepsilon_0 S} \quad (2.3)$$

Then, from Equations (2.2)-(2.3) the real and imaginary parts of the complex dielectric permittivity ε^* of the sample can be calculated.

In general case, when the electric field components are described through the Bessel functions, the calculations of the sample dielectric permittivity are presented in[138]. It can be demonstrated, that the capacitance of the dynamic capacitor reads:

$$C = \frac{\varepsilon'^{1/2} r J_1(\frac{2\pi}{\lambda}\varepsilon'^{1/2} r)}{\frac{2\pi}{\lambda} d J_0(\frac{2\pi}{\lambda}\varepsilon'^{1/2} r)} \quad (2.4)$$

where r is the radial coordinate.

However, from the low-frequency end, the range is unlimited, while from the high-frequency end (above 3 GHz), there are some difficulties related to the coaxial line itself. The limit is determined by the following condition:

$$\lambda > \pi(r_3 + r_4) \quad (2.5)$$

where r_3 and r_4 are the radii of the inner and outer conductors of the coaxial line, λ is the wavelength of radiation.

2.1.3 Microwave frequency range

A vector analyzer MICRAN R4M-18 with 16×8 mm^2 and a scalar network analyzer Elmika R2-408R with 7.2×3.4 mm^2 waveguide systems were used for microwave measurements in 12-18 GHz and 26-37 GHz frequency ranges, respectively. Both setups allow to directly get the frequency dependencies of the scattering parameters, transmitted/input (S_{21}) and reflected/input (S_{11}) signals. The S-parameters can then be transformed into the dielectric permittivity of the sample. The procedure of this transformation depends on

the experimental technique used. Two different techniques are available: the thin-rod method and the full fill waveguide method. Each technique details are discussed in the current subchapter.

Full fill waveguide method

The full fill method consists in measuring the electromagnetic response of the sample of rectangular parallelepiped shape with a thickness of τ and cross-section equal to the waveguide cell. A schematic representation of the waveguide space with the sample inside is shown in Figure 2.1.

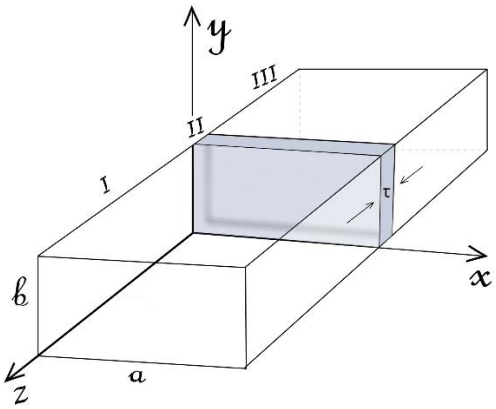

Figure 2.1: Schematic representation of the waveguide space with the sample inside.

In this case, the waveguide space can be conventionally divided into three regions: I - the region where the incident radiation falls on the sample, II - the region filled with the sample, III - the region where transmitted signal propagates after passing through the sample. Then the equations of the waves in the waveguide for these regions write[139,140]:

$$\begin{cases} \psi_I = \cos\left(\frac{\pi x}{a}\right)\left[C_1 e^{ik_0 z} + C_2 e^{-ik_0 z}\right], z \le 0, \\ \psi_{II} = \cos\left(\frac{\pi x}{a}\right)\left[C_3 e^{ikz} + C_4 e^{-ikz}\right], 0 \le z \le \tau, \\ \psi_{III} = \cos\left(\frac{\pi x}{a}\right)\left[C_5 e^{ik_0 z}\right], z \ge \tau, \end{cases} \quad (2.6)$$

where expressions for wavenumbers k_0 and k in the waveguide were introduced in subchapter 1.2.

Using the following boundary conditions for regions I-III[61]:

$$\begin{cases} \psi_I|_0 = \psi_{II}|_0, \\ \psi_{II}|_\tau = \psi_{III}|_\tau, \\ \frac{\partial \psi_I}{\partial z}|_0 = \frac{\partial \psi_{II}}{\partial z}|_0, \\ \frac{\partial \psi_{II}}{\partial z}|_\tau = \frac{\partial \psi_{III}}{\partial z}|_\tau. \end{cases} \quad (2.7)$$

one can obtain expressions for the unknown coefficients C_i and, therefore, for the S-parameters:

$$S_{11} = \frac{C_2}{C_1} = \frac{-[(k_0/k)^2-1]\sin(k\tau)}{-2i(k_0/k)cos(k\tau)-[(k_0/k)^2+1]\sin(k\tau)} \quad (2.8)$$

$$S_{21} = \frac{C_5}{C_1} = \frac{-2(k/k_0)[cos(k_0\tau)-i\sin(k_0\tau)]}{-2(k/k_0)cos(k\tau)+i[(k/k_0)^2+1]\sin(k\tau)} \quad (2.9)$$

Thus, numerically solving the equations system (2.8)-(2.9) by using the experimentally measured frequency dependences of the S_{11} and S_{21} parameters, it is possible to obtain the complex dielectric permittivity $\varepsilon^* = \varepsilon' - i\varepsilon''$ spectra. However, this method is only suitable for samples with low ε' and ε'' values when the transmitted/input S_{21} signal is non-zero.

Thin cylindrical rod method

According to the considered method, the cylindrical rod-like sample with a diameter of around 1 mm is placed in the center of the waveguide perpendicularly to the broad waveguide wall (or parallel to the electric field vector of the dominant TE_{10} mode) as shown in Figure 2.2. The place in the center of the waveguide is ideal for the sample to be placed since the fundamental mode has a single maximum there.

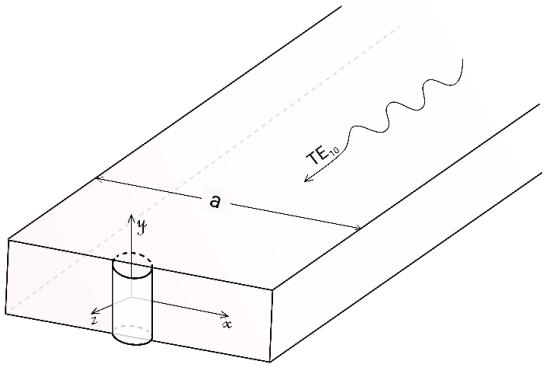

Figure 2.2: Schematic representation of the rectangular waveguide with the cylindrical rod-like sample inside.

Complex dielectric permittivity can be estimated, similarly to the previous method, from measured electromagnetic response coefficients (S_{11} and S_{21}). For this case, the waveguide space can also be divided into three regions I-III (see Figure 2.3), where the intrinsic TE_{10} wave propagates from the region I to region III. Then, by determining all the field components (in regions I and III, in region II outside and inside the cylinder) and by setting up the boundary conditions for all regions and at all discontinuity surfaces, it is possible to find the system of linear equations:

$$\begin{cases} S_{11} = f(\varepsilon', \varepsilon'') \\ S_{21} = f(\varepsilon', \varepsilon'') \end{cases} \tag{2.10}$$

The system (2.10) can be numerically solved and the complex dielectric permittivity can be found. The details of the described procedure are presented in [138,141].

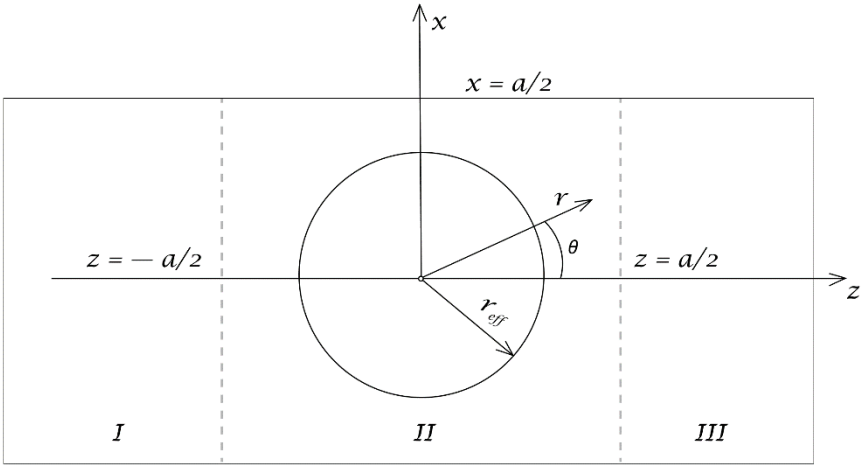

Figure 2.3: Schematic representation of the rectangular waveguide with the cylindrical rod-like sample inside (top view).

2.1.4 Teraherz frequency range

Time-domain terahertz-transmission spectroscopy (TDTTS) method was used for dielectric measurements in the frequency range from 100 GHz to 3 THz[142]. These measurements were performed using a time-domain THz spectrometer T-SPEC series (Ekspla Ltd.) based on a femtosecond fiber laser (wavelength 1 μm, pulse duration less than 150 fs) and a GaBiAs

photoconductive terahertz emitter and detector. The experimental setup is presented in Figure 2.4.

The TDTTS method consists in the measurement of a reference waveform $E_r(t)$ through the empty diaphragm without sample and signal waveform $E_s(t)$ through the sample attached to the diaphragm. Using the Fast Fourier Transform, the time-domain functions $E_r(t)$ and $E_s(t)$ are transformed into frequency-domain functions $E_r(\omega)$ and $E_s(\omega)$, after that the complex transmission function is defined as[142,143]:

$$T(\omega) = \frac{E_s(\omega)}{E_r(\omega)} \tag{2.11}$$

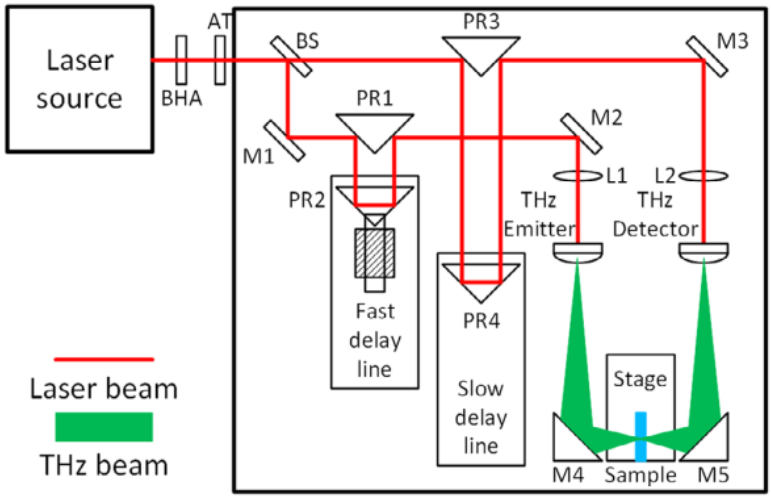

Figure 2.4: Schematic representation of the TDTTS setup[143].

In the case of a homogeneous sample, the complex refraction index $n = n' + in''$ is related to the complex transmission as[142]:

$$T(\omega) = \frac{4n \exp[i\omega(n-1)d/c]}{(n+1)^2} \sum_{k=0}^{m} \left[\left(\frac{n-1}{n+1}\right) \exp(i\omega nd/c)\right]^{2k} \tag{2.12}$$

where d is the sample thickness, c is the light velocity and m is the number of reflections in the sample. The value of the coefficient m can be easily determined experimentally (at least for thick samples), since the reflections in the sample form separate pulses in the measured signal.

The complex transmission function (2.12) can be divided into two real equations for the modulus $|T|$ and phase φ (can be determined experimentally) with two real variables n' and n'' (e.g. the simplest particular case when m=0)[142]. The equations can then be solved numerically for n' and n''. The

same algorithm is in principle valid for the case of $m \neq 0$, however slightly more complicated expressions are obtained, but they can be also solved numerically

All described above experimental techniques allow to measure the effective dielectric permittivity $\varepsilon_{eff} = \varepsilon\mu = n^2$, where the predominant contribution in microwave frequency range is made by the dielectric permittivity ε, while the magnetic permeability μ is negligible for composites based on Ni@C core-shell nanoparticles[28,129–131], manganese ferrite $MnFe_2O_4$[144,145], iron nanowires[112] and iron fibers[114,115].

2.2 Sample preparation procedures

2.2.1 Monofiller composite samples

Commercial Epikote 828 epoxy resin with a density of 1.16 g/cm^3 and a triethylenetetramine hardener (TETA) were used to prepare the composites. The used polymer allows the easy dispersion of various additives and shows high mechanical and chemical resistance[11,146].

Three types of commercially available magnetic nanoparticles provided by US Research Nanomaterials, Inc were used as fillers in corresponding monofiller composite series:

1. *Goethite* ($Fe_2O_3 \cdot H_2O$ alpha, 98%, 50 nm × 10 nm) *nanorod powder* (https://www.us-nano.com/inc/sdetail/42381). It is a yellow powder with a rod-shaped structure, which is widely used in coating, plastic, paint, and pharmaceutical fields. The aspect ratio of nanorods is close to 5, as proved by scanning electron microscopy (SEM) image (see Figure 2.5a). The nanopowder density is 4.4 g/cm^3.
2. *Manganese ferrite* ($MnFe_2O_4$) *nanopowder* with spherical-shaped particles of 28 and 60 nm in size (https://www.us-nano.com/inc/sdetail/7019 and https://www.us-nano.com/inc/sdetail/595) with a density of about 5.4 g/cm^3 for both.
3. *Ni@C core-shell nanoparticles* (https://www.us-nano.com/inc/sdetail/171), which are 20 nm-thick Ni particles coated with several closely compacted carbon layers being a few nanometers

thick[147,148]. The density is 8.9 g/cm^3. The microstructure of Ni@C nanoparticles is represented in Figure 2.5b.

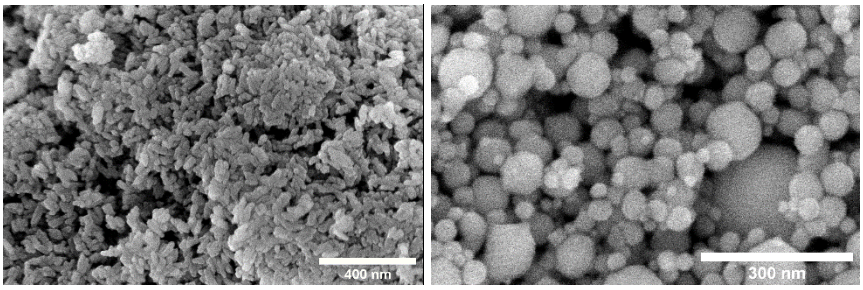

a b

Figure 2.5: Scanning electron microscopy images of (a) goethite nanorods and (b) Ni@C (carbon-coated Ni) nanoparticles.

Each type of aforementioned magnetic nanoparticles is easily dispersed in the polymer matrix and enables the production of composites with high volume concentrations.

Monofiller composite series were prepared according to the standard procedure for filler particles dispersing in a polymer matrix[149–151]. The preparation processes details of composites based on goethite nanorods and manganese ferrite completely coincide, while for Ni@C-based composites, certain steps of the procedure undergo minor differences. As the first stage, the required nanoparticle amount was mechanically crushed and stirred in ethanol (for $Fe_2O_3 \cdot H_2O$ and $MnFe_2O_4$) or isopropanol (for Ni@C) for 30 minutes. Then, nanoparticles/alcohol suspensions were treated by 1 h-ultrasonication: bath for ethanol-based ones and probe for isopropanol-based ones. Afterward, the resulting mixtures were combined with the epoxy resin and underwent additional ultrasonication by the probe for 1-2 hours. After alcohol evaporation, a hardener was added to the mixture of resin and nanoparticles, and manually mixed for 5-7 min. The hardener was added in a ratio of 1:10 with respect to the epoxy resin. The blend was poured into molds and left as such for 20 h for the curing process at room temperature, and then for 2 h in an oven at a temperature of 100 ^oC for the final polymerization step. Such parameters of the preparation procedure were experimentally determined as optimal for the best dispersion of each type of considered nanoparticles in the epoxy resin matrix.

After the above manipulations, epoxy-based samples' list of monofiller composite series represents as follows:

1. 0, 5, 10, 20, 30 and 40 vol.% of $Fe_2O_3 \cdot H_2O$;
2. 0, 10, 20, 23, 25, 28 and 30 vol.% of $MnFe_2O_4$;
3. 0, 10, 15, 25 and 30 vol.% of Ni@C.

The filler concentrations in each composite system were chosen close to the percolation threshold theoretical value (below and above) for these particles[152,153]. The volume concentrations were evaluated from weight concentrations taking into account the densities of nanopowders and epoxy resin.

2.2.2 Bifiller composite samples

Bifiller (or hybrid) composite series consisting of two types of particles inside epoxy resin matrix are considered. The first filler is multi-walled carbon nanotubes (MWCNTs) grown by the chemical vapor deposition method[154–156] with an average outer diameter of 20-40 nm, the length of 0.5-200 μm and the density of 2.0 g/cm^3. Scanning electron microscopy micrograph of MWCNTs is presented in Figure 2.6. Manganese ferrite (28 nm-spherical particles) or Ni@C nanoparticles in the epoxy/MWCNT/$MnFe_2O_4$ or epoxy/MWCNT/Ni@C composite series, respectively, are used as the second fillers.

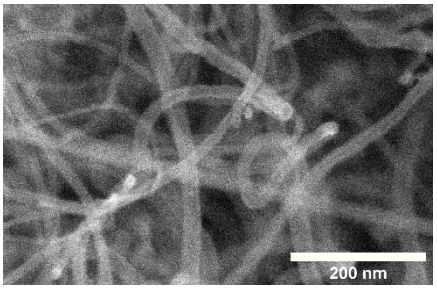

Figure 2.6: Scanning electron microscopy image of multi-walled carbon nanotubes.

The preparation method of bifiller composites does not differ essentially from the dispersion of one filler in a polymer matrix[149–151]. The only difference is the separate dispersion of each inclusion type in alcohol (in our particular case, ethanol for epoxy/MWCNT/$MnFe_2O_4$ and isopropanol for epoxy/MWCNT/Ni@C systems) by using ultrasonication (1-h probe for

magnetic particles/alcohol suspensions, 1-h probe and 1-h bath for MWCNTs/alcohol suspensions). Thereafter, epoxy resin (Epikote 828) was added to the MWCNTs/alcohol suspension, and the resulting mixture was processed with an ultrasonic probe for 1 h. This preparation protocol is associated with the high MWCNTs ability to form agglomerates (due to their huge aspect ratio), and therefore they require more intense dispersion by ultrasonic treatment. The final 1 h ultrasonic probe treatment took place after mixing together both the magnetic particles/alcohol and MWCNTs/epoxy/alcohol obtained suspensions. Then, after complete alcohol evaporation, the resulting mixture was cured by a triethylenetramine (TETA) hardener for 20 h at room temperature and 2 h at 100 ^{o}C in the oven.

Using the technique described above, two series of epoxy/MWCNT/$MnFe_2O_4$ and one series of epoxy/MWCNT/Ni@C hybrid composites with a fixed MWCNTs-content and various second-filler amounts were prepared. As a result, the final hybrid samples' list is as follows:

1. 0.09 vol.% of MWCNT + 0, 0.025, 0.05, 0.35, 0.65, 5 and 10 vol.% of $MnFe_2O_4$;
2. 0.58 vol.% of MWCNT + 0, 0.025 and 0.58 vol.% of $MnFe_2O_4$;
3. 0.09 vol.% of MWCNT + 0, 0.025, 0.2, 0.6 and 1 vol.% of Ni@C.

The MWCNT content of 0.09 vol.% is the concentration just below the percolation state in corresponding monofiller composites[157], while the higher MWCNT content of 0.58 vol.% is above the percolation threshold. And such relatively low second-filler concentrations were chosen because hybrid composites with higher concentrations demonstrate non-uniform nanoparticle distributions as it will be shown further.

3. RESULTS AND DISCUSSION

3.1 Dielectric properties and electrical percolation in epoxy resin composites based on magnetic nanoparticles

Nowadays, there is a great interest in polymer composite materials filled with various nanoparticles, caused by the ability to control their properties at the nanoscale and as a consequence to apply them in different functional devices[19,158]. Electrically conductive polymer composites based on both organic and inorganic nanofillers attract the attention of scientists because of their potential applications, such as antistatic materials[11] and electromagnetic coatings[12], solar cells and biosensors[14], electromagnetic shielding, and absorption of radiation in different frequency ranges[15]. Epoxy resin, due to its attractive mechanical and thermal properties, is a very popular polymer matrix for composite preparation[159,160].

Due to the low percolation threshold, as well as their unique electrical, thermal, and mechanical properties, various carbon fillers are popular and already studied quite well in recent years[19,32,70,161]. However, materials based on metal and metal oxide nanoparticles are also gaining popularity because of their wide range of applications, from catalysis to nanoelectronics[109]. The range of their potential applications, in particular, iron oxide nanoparticles, expands even more if one considers that in addition to dielectric properties, they can have magnetic and ferromagnetic properties. Then, these particles can also be applied in such areas as magnetic resonance imaging, tissue engineering, and drug delivery and also as hyperthermia agents[23].

Particularly, nanowires, nanorods, and others as magnetic particles of high aspect ratio are interesting for composites[112,113]. However, investigations of polymer composites with goethite ($Fe_2O_3 \cdot H_2O$) nanorods are rare enough[111]. Moreover, the investigations of goethite-based siloxane composites show the relatively small dielectric permittivity value[111]. Therefore, it is important to determine the electrical percolation threshold in composites with goethite nanorods and find the relation between the electrical percolation threshold and composite preparation technology.

Manganese ferrite ($MnFe_2O_4$) nanoparticles are already studied quite well from the magnetic properties point of view and on this basis they have found applications in many directions, such as magnetic recording media devices[20], ferrofluid[21], biosensors[110], and for biomedical applications[22]. However, investigations of $MnFe_2O_4$ in terms of electrical properties can also be interesting, to make them applicable (along with very popular carbon

materials) in fields such as electromagnetic shielding[15,162] and compatibility[163]. Nevertheless, the electrical percolation phenomena were not studied in composites with $MnFe_2O_4$ inclusions.

Nickel (Ni) nanosized particles and carbon-coated Ni nanoparticles (Ni@C) have superparamagnetic or ferromagnetic features, which, due to the presence of magnetic losses[27,28], make them also promising for the design of microwave absorbing devices. The thermal behavior of broadband dielectric and magnetic properties has been studied for the composites made of polymer filled with Ni@C concentrations below the percolation threshold[164]. However, the dielectric properties of composites with Ni@C content above the percolation threshold, as well as the electrical percolation in these composites have not been studied yet. The electrical percolation threshold in composites with quasi-spherical particles ($MnFe_2O_4$ or Ni@C) can be substantially lower than it is expected by the excluded volume theory and dependent on particle size, so that these composites can substitute carbon-based composites in various electronics applications[165,166].

This subchapter is devoted to the dielectric/electric properties experimental investigations of three epoxy resin composite systems based on different magnetic nanoparticles: goethite ($Fe_2O_3 \cdot H_2O$) nanorods, manganese ferrite ($MnFe_2O_4$) and Ni@C core-shell nanoparticles.

3.1.1 Goethite nanorods / epoxy resin composites

Room-temperature region

The surface of goethite nanorods / epoxy resin composites was investigated by scanning electron microscopy. The results for the highest concentration available are presented in Figure 3.1. It can be concluded that nanorods are dispersed homogeneously.

The concentration dependence of the complex dielectric permittivity of $Fe_2O_3 \cdot H_2O$ / epoxy resin composites at room temperature and frequency of 129 Hz is shown in Figure 3.2a. The addition of nanorods into the polymer matrix leads to an increase of dielectric permittivity according to the power law of percolation (Equation (1.19))[66,68,71,72,75,76,167]. Approximation of the real part of the dielectric permittivity according to the percolation law is shown in Figure 3.2b. This calculation indicates that the electrical percolation for the $Fe_2O_3 \cdot H_2O$ / epoxy resin composites is reached when the filler concentration is close to 40 vol.%. This is also confirmed by the plateau in conductivity

spectrum for composite with 40 vol.%, while for lower filler concentrations this plateau is absent. In order to increase the determination accuracy of p_c, many more samples with different goethite nanorods concentrations in a range between 30 and 40 vol.% are needed.

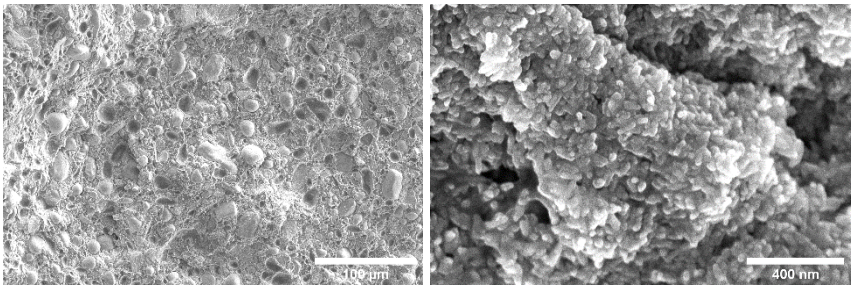

a b

Figure 3.1: Scanning electron microscopy images of $Fe_2O_3 \cdot H_2O$ / epoxy resin composites with 40 vol.% filler concentration (at different magnification levels).

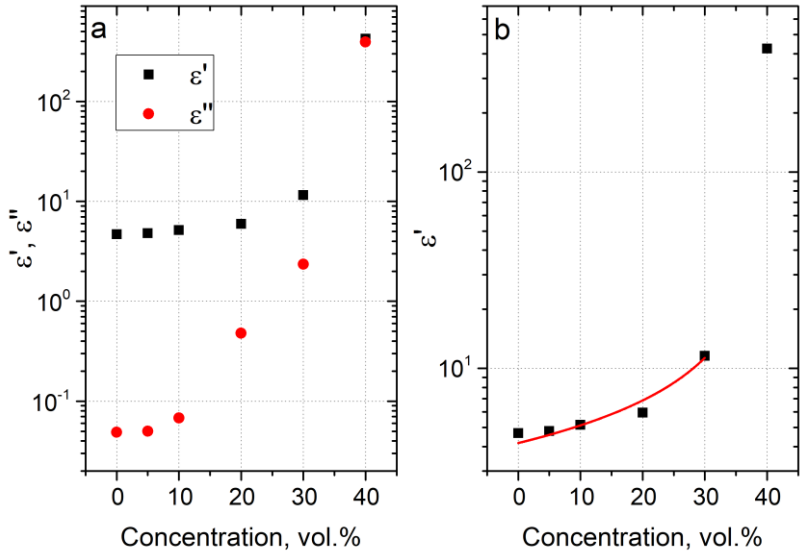

Figure 3.2: (a) Concentration dependence of the complex dielectric permittivity of $Fe_2O_3 \cdot H_2O$ / epoxy resin composites at room temperature and frequency of 129 Hz; (b) A percolation law of the real part of permittivity $\varepsilon' \propto (40 - p)^{-0.72}$ for $Fe_2O_3 \cdot H_2O$ / epoxy resin composites.

The frequency dependence of the complex dielectric permittivity in a wide frequency range (from hertz to terahertz) at room temperature is shown in Figure 3.3. However, measurements above 1 MHz were performed only for two composites with the highest concentrations (30 and 40 vol.%). This choice was due to the fact that the permittivity of composites below the percolation threshold at room temperature is almost frequency-independent and its value is close to pure epoxy resin permittivity[149,150]. In the microwave frequency range, the value of complex dielectric permittivity is very similar to the corresponding properties of epoxy resin composites filled with iron nanowires and nanoparticles[112].

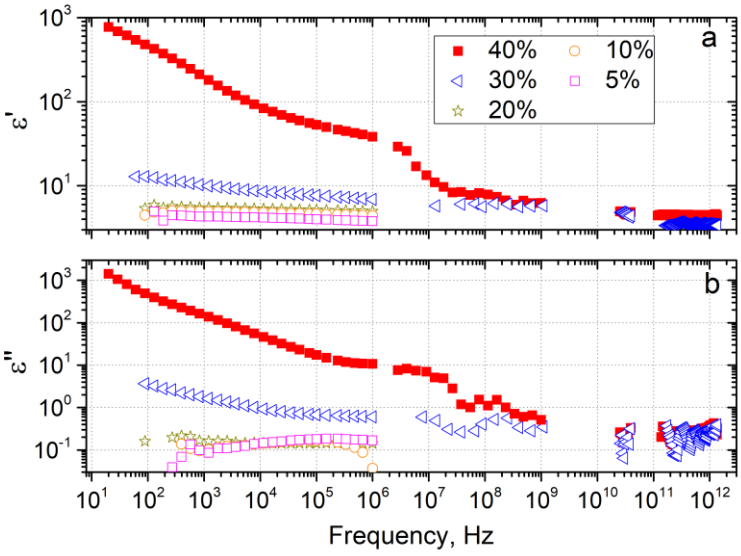

Figure 3.3: Room-temperature broadband frequency dependence of complex dielectric permittivity of $Fe_2O_3 \cdot H_2O$ / epoxy resin composites.

Temperature-dependent region: dielectric permittivity spectra

The temperature dependence of the complex dielectric permittivity for $Fe_2O_3 \cdot H_2O$ / epoxy resin composites at 129 Hz is shown in Figure 3.4. At low temperature, composites below the percolation threshold demonstrate a dielectric permittivity close to pure epoxy resin permittivity and it is almost temperature-independent. The imaginary part is quite noisy because its values at these temperatures are of the same order as the measurement's accuracy.

Meanwhile, at high temperatures, the imaginary part of the dielectric permittivity increases strongly even for composites below the percolation threshold. Such behavior at high temperatures is typical for epoxy resin composites[11,168] and it indicates the electrical conductivity phenomenon, which dominates in composites both above and below the percolation threshold.

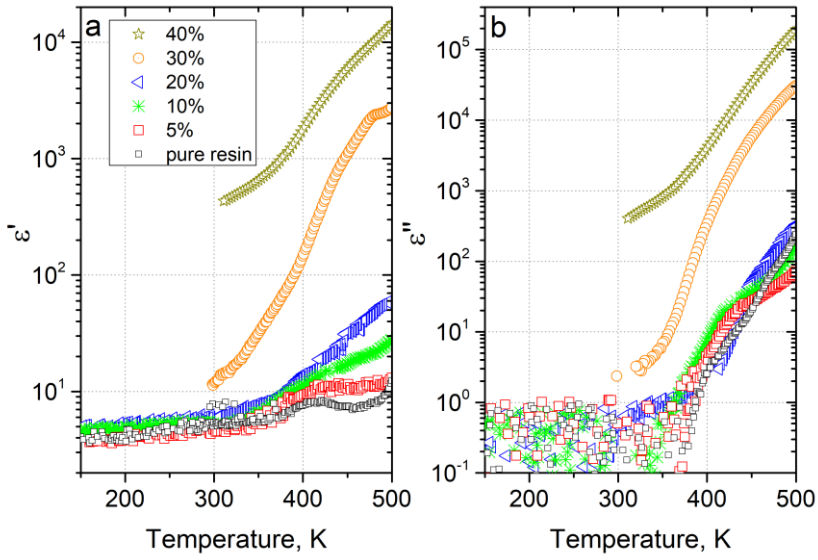

Figure 3.4: Temperature dependence of the complex dielectric permittivity of $Fe_2O_3 \cdot H_2O$ / epoxy resin composites at 129 Hz.

The temperature dependence of the complex dielectric permittivity at different frequencies of $Fe_2O_3 \cdot H_2O$ / epoxy resin composite with 5 vol.% filler concentration is shown in Figure 3.5. The imaginary part of the dielectric permittivity has a maximum, which position is frequency-dependent. When the frequency increases, the maximum expands and shifts towards higher temperatures. The real part of the dielectric permittivity decreases with increasing frequency. Such dielectric dispersion is due to the molecule dynamics of epoxy resin[11,169]. At high temperatures (above 350 K), the complex dielectric permittivity and the loss tangent $\varepsilon''/\varepsilon'$ sharply increases due to the appearance of electrical conductivity.

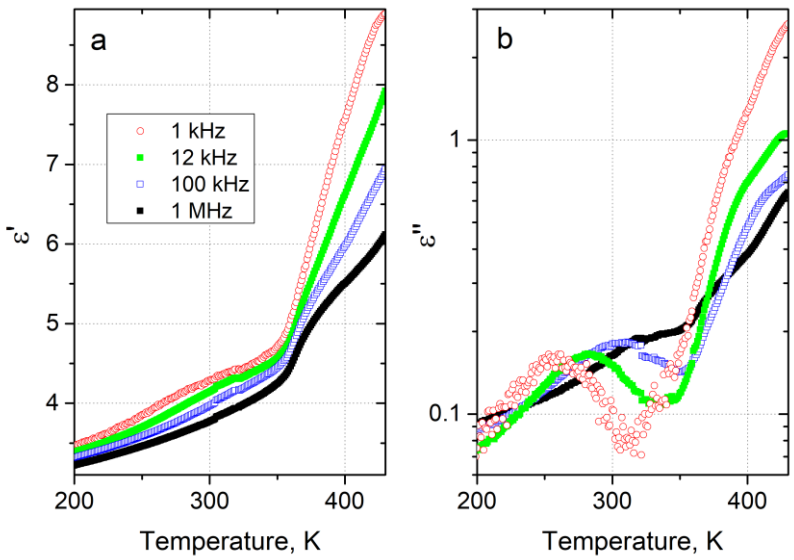

Figure 3.5: Temperature dependence of the complex dielectric permittivity of $Fe_2O_3 \cdot H_2O$ / epoxy resin composite with 5 vol.% filler concentration at different frequencies.

The frequency dependence of the complex dielectric permittivity at different temperatures for $Fe_2O_3 \cdot H_2O$ / epoxy resin composite with 5 vol.% filler concentration is shown in Figure 3.6. At temperatures above 25 ºC, the spectra of the imaginary part of the dielectric permittivity present a maximum corresponding to the absorption peak. The physical process that causes the absorption peak is the reorientation of the dipoles. This behavior is typical for composites below the percolation threshold, and it is due to the dipole relaxation[11,151,170].

On cooling, the maximum of ε'' expands and shifts towards low frequencies, while at low temperatures (below 270 K), it generally disappears. The frequency at the maximum of the imaginary part of the dielectric permittivity (ν_{max}) at a fixed temperature allows to determine the average relaxation time by using the following equation: $\tau = 1/\nu_{max}$. Then, on cooling, the relaxation time increases according to the Vogel-Fulcher law[171–174] (see Figure 3.7):

$$\tau = \tau_0 e^{\frac{E_B}{k_B(T-T_0)}} \qquad (3.1)$$

where τ_0 is the relaxation time at very high temperatures, E_B is the activation energy, k_B is the Boltzmann constant, and T_0 is the glass transition temperature. Obtained parameters are presented in Table 3.1. In composites, the glass transition temperature increases with goethite nanorod concentration. This increase can be explained by the strong interactions between the epoxy resin and $Fe_2O_3 \cdot H_2O$ nanorods. Moreover, according to the theoretical calculations, the density of composite could be higher than the pure polymer density, and therefore the increase of the glass transition temperature with the filler concentration could be observed[40,175].

Table 3.1: Parameters of the Vogel-Fulcher law fits (according to Equation (3.1)) of the average relaxation time to the data of Figure 3.7.

Concentration, vol. %	ln{τ_0, s}	E_B/k_B, K	T_0, K
0	-27.4	2689	142
5	-20	1649	91
10	-18	773	152
20	-18	805	180

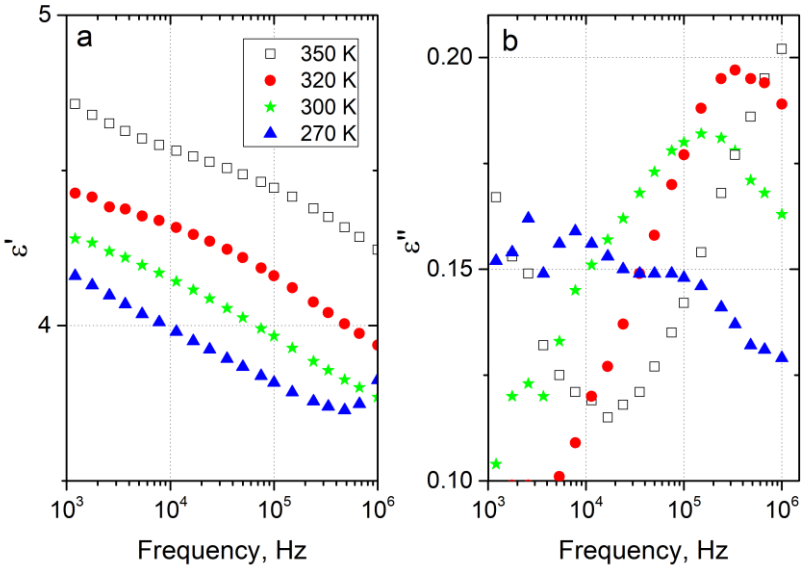

Figure 3.6: Frequency dependence of the complex dielectric permittivity of $Fe_2O_3 \cdot H_2O$ / epoxy resin composite with 5 vol.% filler concentration at different temperatures.

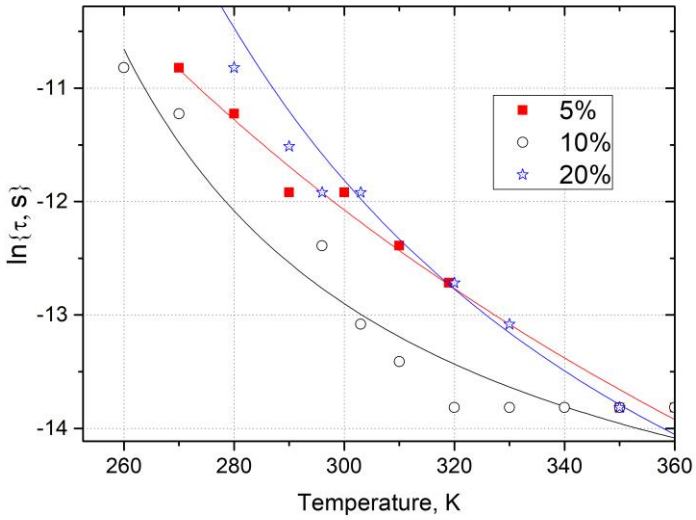

Figure 3.7: Temperature dependence of the average relaxation time of $Fe_2O_3 \cdot H_2O$ / epoxy resin composites. The solid lines correspond to the approximations by Vogel-Fulcher law (Equation (3.1)).

Temperature-dependent region: electrical conductivity spectra

The electrical conductivity σ was calculated according to the following equation: $\sigma = \omega \varepsilon_0 \varepsilon''$, where $\omega = 2\pi\nu$, ν is the frequency, and ε_0 is the dielectric permittivity of vacuum. The frequency dependence of the electrical conductivity ($\sigma(\nu)$) for $Fe_2O_3 \cdot H_2O$ / epoxy resin composite with 20 vol.% filler concentration at different temperatures (at temperatures not lower than 370 K, where any relaxation related to the polymer matrix is observed in dielectric spectra) is shown in Figure 3.8.

In the investigated frequency range, two separate regions of electrical conductivity can be observed, namely, the region of the frequency-independent plateau (at low frequencies) and the frequency-dependent region (at high frequencies). Therefore, the $\sigma(\nu)$ can be well fitted according to the universal Almond-West power law[170,176]:

$$\sigma = \sigma_{DC} + A\omega^s \qquad (3.2)$$

where σ_{DC} is the DC conductivity and $A\omega^s$ is the AC conductivity. The DC conductivity is due to a random distribution of electrical charge carriers.

The AC conductivity (σ_{AC}) increases, approximately, according to a power law with an almost equivalent slope.

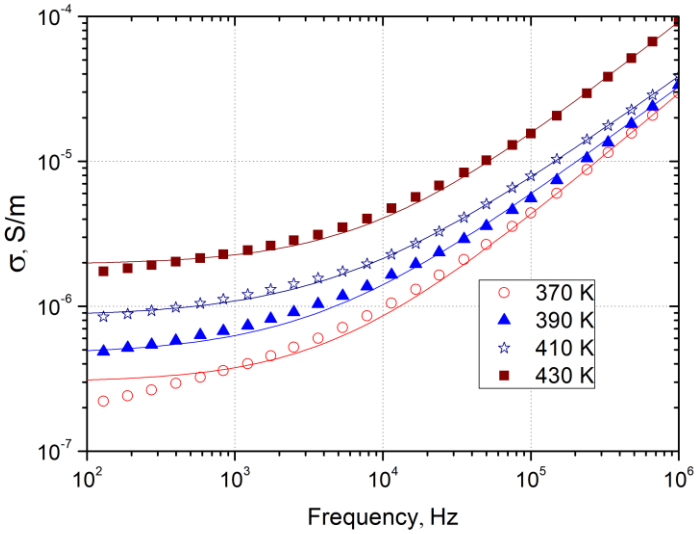

Figure 3.8: Frequency dependence of the electrical conductivity of $Fe_2O_3 \cdot H_2O$ / epoxy resin composite with 20 vol.% filler concentration at different temperatures. The solid lines are the best fit according to Equation (3.2).

The conductivity spectra are fitted with Equation (3.2) quite well, except the data at very low frequencies, where discrepancies appear due to blocking contact effects[177]. This behavior of both DC and AC conductivity can be addressed to the contribution of electronic conductivity inside epoxy resin[11]. A similar conductivity behavior was observed for all other investigated composites (see Figure 3.9) and has good agreement with the data presented in the literature for metal oxide composites[23], as well as for composites based on, for example, carbon fillers[11,40,178]. Another characteristic feature is an increase of the DC conductivity with the filler concentration (see Figure 3.9). When the filler concentration changes from 20 to 30 vol.%, a significant jump in the DC conductivity absolute value is observed. It is because the concentration of 30 vol.% is below but close to the percolation threshold value, when the percolation network is almost formed, but there is no percolation yet.

The temperature dependence of DC conductivity was approximated by the Arrhenius law[179,180]:

$$\sigma_{DC} = \sigma_0 \exp\left(-\frac{E_A}{k_B T}\right) \quad (3.3)$$

where σ_0 is the pre-exponential factor and E_A is the conductivity activation energy. Obtained parameters are presented in Table 3.2.

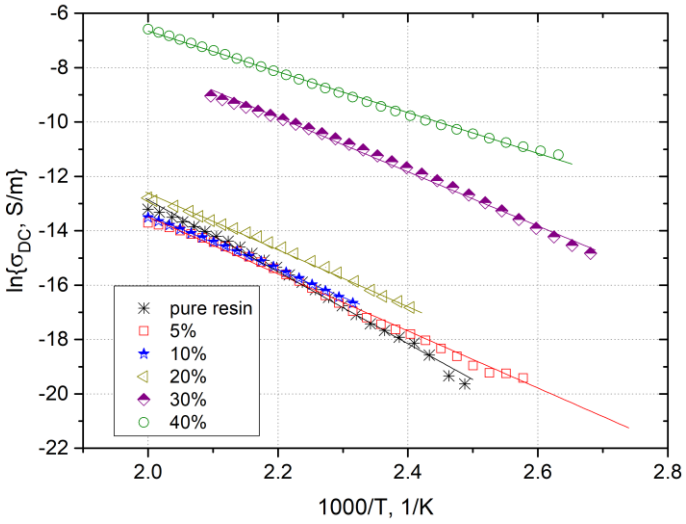

Figure 3.9: Temperature dependence of DC electrical conductivity of $Fe_2O_3 \cdot H_2O$ / epoxy resin composites.

Table 3.2: Parameters of the Arrhenius law fits (according to Equation (3.3)) of the DC conductivity to the data of Figure 3.9.

Concentration, vol. %	σ_0, S/cm	E_A/k_B, K
0	7969	13225
5	18	10480
10	8.3	10073
20	39	10438
30	1808	9973
40	42	7498

In $Fe_2O_3 \cdot H_2O$ / epoxy resin composites, the conductivity activation energy is almost independent of filler concentration below the percolation threshold,

while above the percolation threshold, it decreases with filler concentration. Similar results are observed for epoxy resin composites filled with carbon nanotubes and carbon black[11,181].

Thus, at high temperatures, because of the finite conductivity of the epoxy resin, electrical conductivity occurs in composites both above and below the percolation threshold.

3.1.2 Manganese ferrite / epoxy resin composites

Room-temperature region

Scanning electron microscopy images of manganese ferrite / epoxy resin composites with different sizes of spherical-shaped $MnFe_2O_4$ nanoparticles (28 and 60 nm) are shown in Figure 3.10. It can be concluded that nanoparticles are distributed homogeneously in both cases.

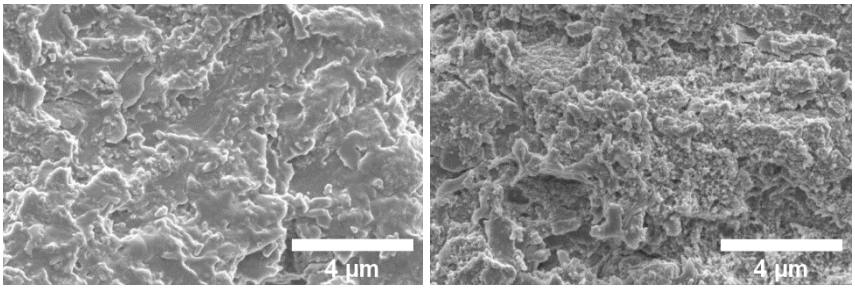

a b

Figure 3.10: Scanning electron microscopy images of $MnFe_2O_4$ / epoxy resin composites with different particles size (left: 60 nm, right: 28 nm).

The frequency dependencies of the real part of dielectric permittivity (ε') and the electrical conductivity (σ) of $MnFe_2O_4$ / epoxy resin composites with 60 nm particle size at room temperature are shown in Figure 3.11.

An increase of the $MnFe_2O_4$ concentration in epoxy resin leads to the monotonic increase of the dielectric permittivity and electrical conductivity values. Moreover, for composites with a filler concentration of ≤20 vol.%, the dielectric permittivity is a completely frequency-independent function, and the DC conductivity plateau is absent (similar to pure epoxy resin). However, for composites with filler concentration of >20 vol.%, the dielectric permittivity is frequency-dependent and at a maximum concentration of 30 vol.% ε' decreases strongly with the increasing frequency, and a weakly

pronounced plateau of σ appears, which indicates that the percolation threshold is close to 30 vol.%.

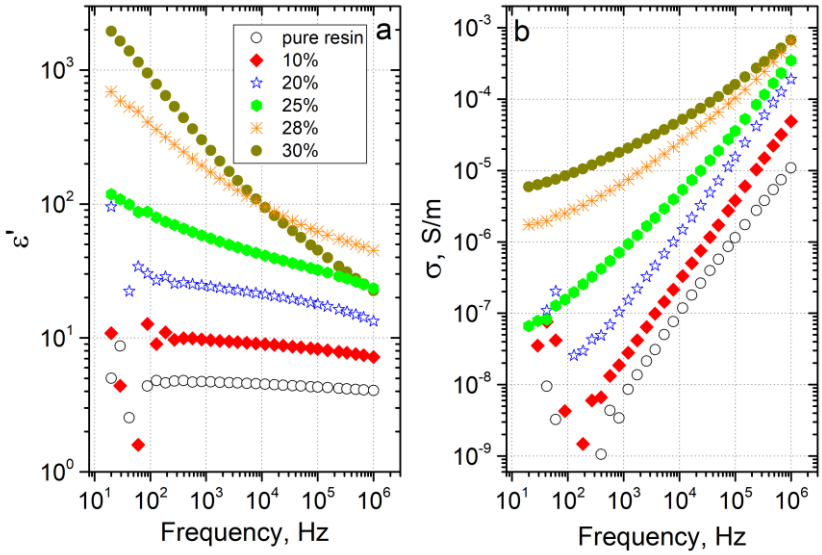

Figure 3.11: Frequency dependence of (a) the dielectric permittivity and (b) the electrical conductivity of $MnFe_2O_4$ / epoxy resin composites with 60 nm particle size at room temperature.

To determine the percolation threshold values of $MnFe_2O_4$ / epoxy resin composites with 28 and 60 nm particle sizes, the dielectric permittivity at 396 Hz and the room temperature was plotted as a function of filler concentration in Figure 3.12. Since all the studied concentrations (except the maximum one of 30 vol.%) do not have a frequency-independent plateau at low frequencies, the dielectric permittivity was fitted according to the classical power law for composites below the percolation threshold (Equation (1.19))[66,68,71,72,75,76,167]. The obtained approximation parameters are listed in Table 3.3.

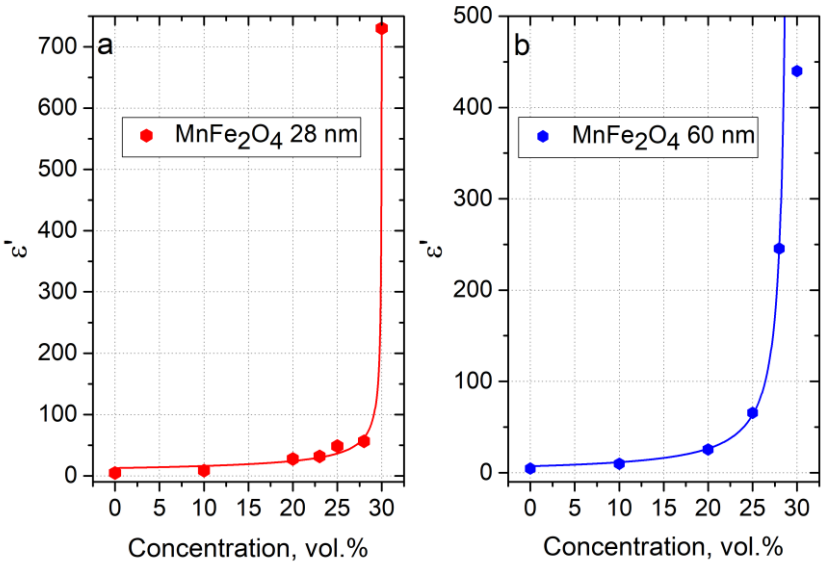

Figure 3.12: Concentration dependence of the real part of dielectric permittivity of $MnFe_2O_4$ / epoxy resin composites with (a) 28 nm and (b) 60 nm particles sizes at room temperature and 396 Hz (symbols), and fits with Equation (1.19) (solid curves).

Table 3.3: Parameters of the percolation threshold law fits (according to Equation (1.19)) to the data of Figure 3.12.

	p_c, vol.%	t
28 nm	30	0.58
60 nm	29.3	1.13

This calculation indicates that the electrical percolation for $MnFe_2O_4$ / epoxy resin composites is reached when the filler concentration is close to 30 vol.%. Moreover, it seems that the percolation threshold depends on the size of the manganese ferrite spherical particles. However, according to the excluded volume theory[102,104], the percolation threshold depends only on the shape of the particles, and not on their size. Therefore, it should be assumed that the difference in the conductive capacity of composites based on $MnFe_2O_4$ nanoparticles of different sizes is due to their different distributions in the polymer matrix.

Temperature-dependent region: dielectric permittivity spectra

Consider the typical behavior of a composite below the percolation threshold using a sample with 20 vol.% $MnFe_2O_4$ (60 nm-sized) as an example. For the latter, the temperature dependence of the complex dielectric permittivity at different frequencies and frequency dependence of complex dielectric permittivity at different temperatures are shown in Figures 3.13 and 3.14, respectively. For comparison in Figure 3.13, the data for pure epoxy resin are plotted.

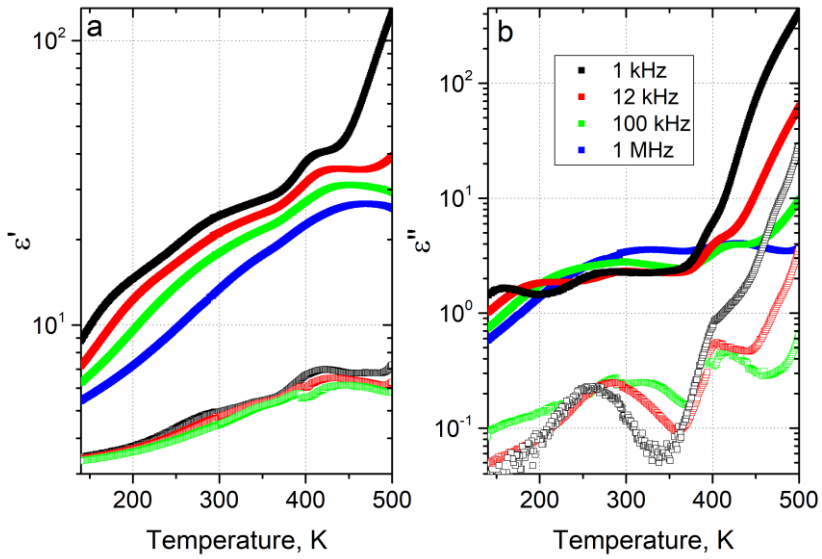

Figure 3.13: Temperature dependence of the complex dielectric permittivity for pure epoxy resin (open symbols) and $MnFe_2O_4$ / epoxy resin composite (close symbols) with 20 vol.% filler concentration (60 nm-sized) at different frequencies.

In the temperature range of 150-250 K, the imaginary part of ε versus T and ν is characterized by maxima, whose position is frequency- and temperature-dependent, respectively. With increasing frequency, the maximum of $\varepsilon''(T)$ expands and shifts toward higher temperatures (Figure 3.13b), whereas during cooling, the maximum of $\varepsilon''(\nu)$ expands and shifts toward lower frequencies (Figure 3.14b). The real part of ε versus T (Figure 3.13a) and ν (Figure 3.14a) decreases with increasing frequency and decreasing temperature, respectively. Similar behavior was observed for each

composite below the percolation threshold of both sizes, as well as for pure epoxy resin (see open symbols in Figure 3.13). This behavior is because of the dipole relaxation[11,151,170].

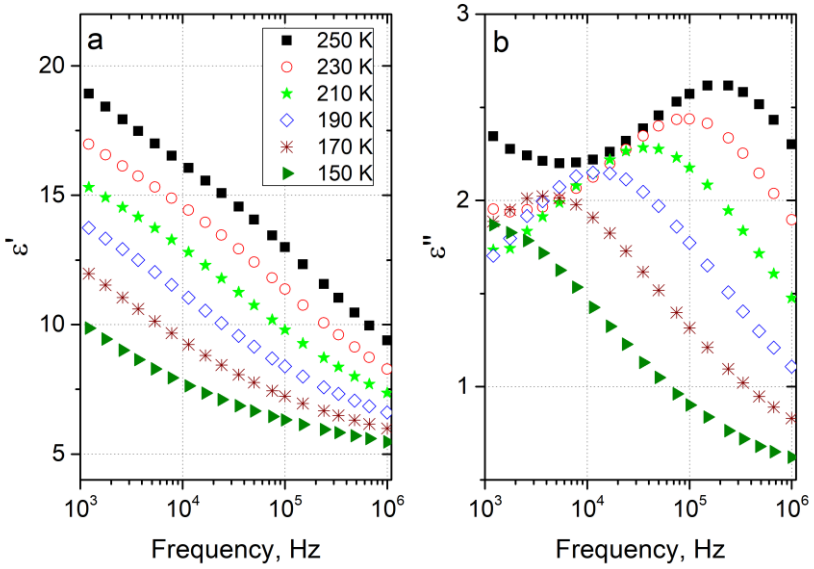

Figure 3.14: Frequency dependence of the complex dielectric permittivity for $MnFe_2O_4$ / epoxy resin composite with 20 vol.% filler concentration (60 nm-sized) at different temperatures.

The relaxation time, defined as the reciprocal frequency value at the maximum of the imaginary part of ε at a fixed temperature, increases according to the Vogel–Fulcher law (Equation (3.1)) with cooling (Figure 3.15). The approximation parameters are listed in Table 3.4. In composites, the glass transition temperature decreases with the $MnFe_2O_4$ addition (any size) compared with pure epoxy resin. Moreover, when concentration increases, the glass transition temperature slightly increases for smaller particles (28 nm) and decreases for larger particles (60 nm). For smaller particles, an increase of the glass transition temperature with the concentration is due to the decrease in the interfacial space between the polymer and nanoparticles, and the opposite situation is observed for larger particles.

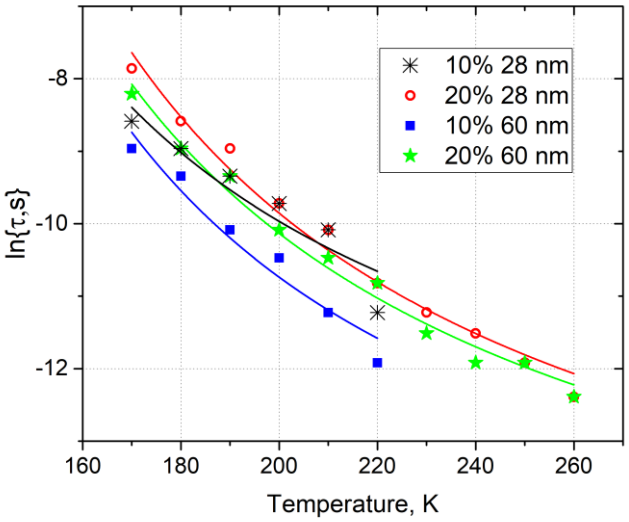

Figure 3.15: Temperature dependence of the relaxation time for $MnFe_2O_4$ / epoxy resin composites below the percolation threshold. Solid lines are calculated according to Equation (3.1).

Table 3.4: Parameters of the Vogel-Fulcher law fits (according to Equation (3.1)) of the average relaxation time to the data of Figure 3.15.

Concentration, vol.%	Particle size, nm	$\ln\{\tau_0, s\}$	E_B/k_B, K	T_0, K
0	-	-23	1969	137
10	28	-15	634	74
20	28	-16.5	798	80
10	60	-16.5	672	83
20	60	-16.5	782	77

Temperature-dependent region: electrical conductivity spectra

For composites below the percolation threshold (e.g., Figure 3.13b) at high temperatures (above 380 K), the imaginary part of the dielectric permittivity increases strongly and becomes higher than the real part, which means that the composite has become conductive. Indeed, at high temperatures (Figure 3.16),

the frequency dependence of the electrical conductivity demonstrates a frequency-independent plateau at low frequencies (corresponds to DC conductivity), and region increasing with frequency at high frequencies (corresponds to AC conductivity). Therefore, the frequency dependence of the electrical conductivity can be fitted according to the Almond-West power law (Equation (3.2)).

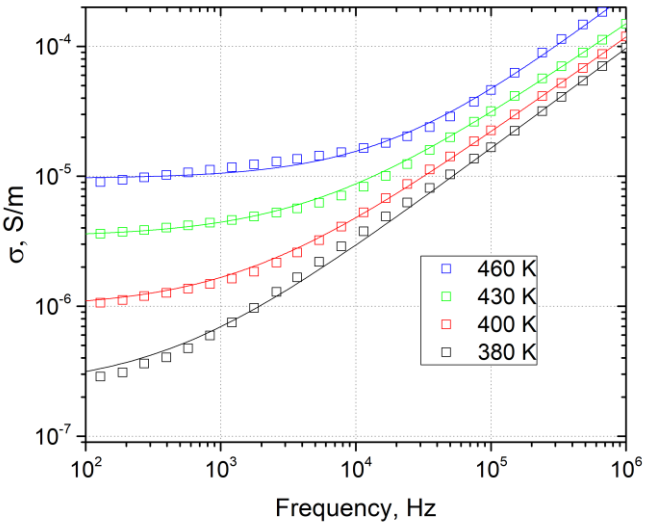

Figure 3.16: Frequency dependence of electrical conductivity for $MnFe_2O_4$ / epoxy resin composite with 20 vol.% filler concentration (60 nm-sized) at different temperatures. Solid lines are calculated according to Equation (3.2).

DC conductivity values for all investigated $MnFe_2O_4$ / epoxy resin composites with 28 nm particle size are shown in Figure 3.17.

For composites below the percolation threshold (10-25 vol.%) and for pure epoxy resin, DC conductivity appears at higher temperatures only, above 380 K. This DC conductivity appearance is due to the epoxy resin becoming conductive at high temperature. The σ_{DC} can be fitted by Arrhenius law (Equation (3.3)). Obtained parameters are listed in Table 3.5. As it can be seen, the conductivity activation energy decreases with filler concentration.

For composites above the percolation threshold (30 vol.%), the DC conductivity is already observed at room temperature and also increases its absolute value during heating.

Table 3.5: Parameters of the Arrhenius law fits (according to Equation (3.3)) of the DC conductivity to the data of Figure 3.17.

Concentration, vol.%	σ_0, S/m	E_A/k_B, K
0	$0.7 \cdot 10^6$	13185
10	$0.2 \cdot 10^5$	10841
20	$0.4 \cdot 10^3$	8745
23	7.31	6247
25	7.30	5961
30	6.67	3791

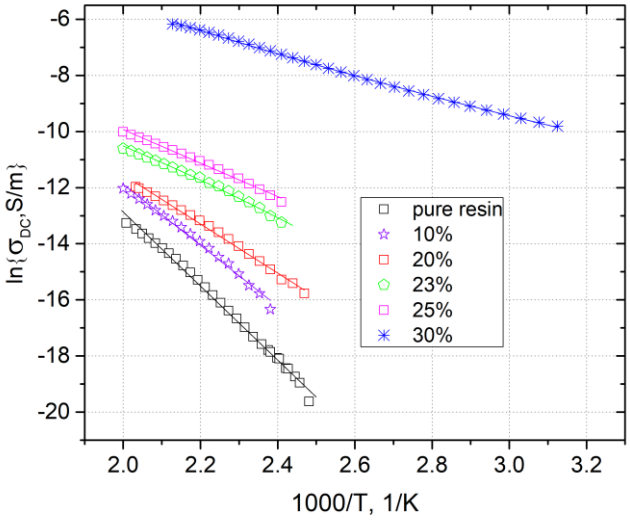

Figure 3.17: Temperature dependence of the DC electrical conductivity for $MnFe_2O_4$ / epoxy resin composites with 28 nm particle size.

A similar conductivity behavior was observed for all other investigated $MnFe_2O_4$ / epoxy resin composites with 60 nm particle size.

3.1.3 Ni@C nanoparticles / epoxy resin composites

Room-temperature region

Scanning electron microscopy images of Ni@C nanoparticles / epoxy resin composites are presented in Figure 3.18. The composites filled with the lowest Ni@C content (10 vol.%) are characterized by a good distribution of nanoparticles, while high (25 vol.%) loading leads to a lower quality dispersion, which manifests in the presence of a larger number of Ni@C agglomerates of different sizes.

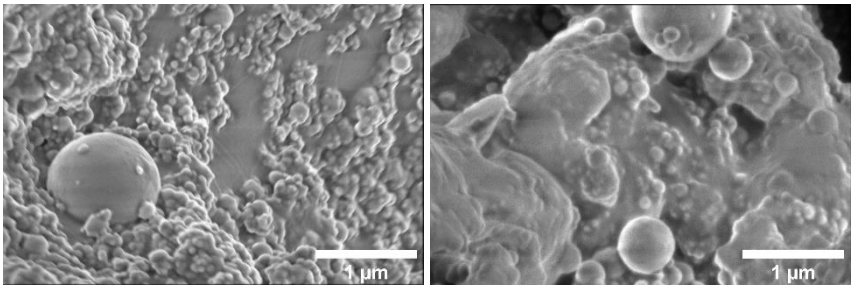

a b

Figure 3.18: Scanning electron microscopy images of Ni@C / epoxy resin composites with (a) 10 and (b) 25 vol.% of Ni@C.

The frequency dependencies of the real part of dielectric permittivity (ε') and the electrical conductivity (σ) of Ni@C / epoxy resin composites at room temperature are presented in Figure 3.19.

For the sample with the lowest Ni@C concentration of 10 vol.% (dark green close symbols), the dielectric permittivity is weakly dependent on the frequency, and the DC conductivity plateau is absent (similarly to empty epoxy resin). Meanwhile, the rest of the samples demonstrate a pronounced conductive behavior, namely, the presence of a strong ε' frequency dependence and the DC conductivity plateau (frequency-independent part of σ). With the increasing embedded Ni@C nanoparticle concentration, the DC conductivity absolute value increases. Such a result indicates that the percolation threshold of Ni@C / epoxy resin composites is in the range between 10 and 15 vol.% of Ni@C nanoparticles.

Moreover, for composites above the percolation threshold the dielectric permittivity (ε') and the electrical conductivity (σ) are very high (ε'=10^5 and σ=0.6 S/m at 100 Hz for composites with 30 vol.% Ni@C). The dielectric permittivity strongly decreases, while the electrical conductivity strongly

increases with frequency. However, the complex dielectric permittivity remains quite high even in the microwave frequency range, so that these composites are suitable for electromagnetic shielding applications.

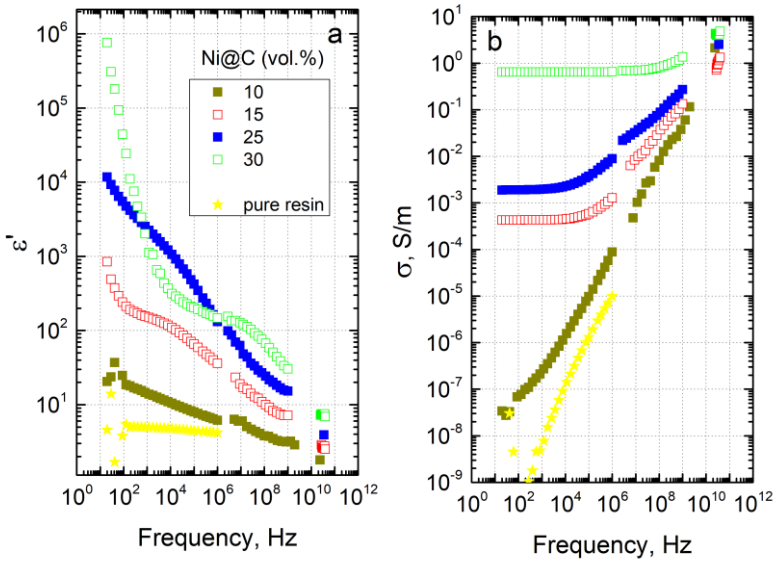

Figure 3.19: Broadband frequency dependencies of (a) the real part of dielectric permittivity and (b) the electrical conductivity of Ni@C / epoxy resin composites at room temperature.

Temperature-dependent region

The temperature dependencies of DC conductivity in a wide temperature range of Ni@C / epoxy resin composites are presented in Figure 3.20.

For non-conductive at room temperature composite with 10 vol.% Ni@C content, DC conductivity appeared at temperatures above 350 K, coursed by the epoxy resin conductivity contribution (at high temperatures epoxy resin becomes conductive)[182]. For the conductive at room temperature samples, a small narrow-temperature (from room temperature to 310 K) reduction in DC conductivity is observed, which is obviously associated with polymer matrix thermal expansion. Then, further heating up to the maximum temperature (500 K) was accompanied by a monotonic increase in DC conductivity values by 2–3 orders of magnitude, which is related to the epoxy resin conductivity contribution. The second process affecting the increase of σ_{DC} is nanoparticles

redistribution inside the matrix (large agglomerates break down into smaller ones)[168,182,183]. That is why, after annealing, there is such pronounced hysteresis of DC conductivity for all samples, which intensifies even more on the back way (from 500 K to room temperature) during cooling due to the compression of the polymer matrix. Moreover, after annealing the DC conductivity of sample with 15 vol.% of Ni@C became higher than with 25 vol.%, which indicates a more successful nanoparticles redistribution in the composite with a lower filler content due to initially smaller agglomerates number and their size. The composite with 10 vol.% of Ni@C remains conductive after annealing. It means that annealing can be effectively used to decrease the percolation threshold in Ni@C / epoxy resin composites. The lowest increase of electrical conductivity after annealing is observed for composites with the highest Ni@C concentration obviously due to the lowest distances between conductive clusters and the most stable initial percolation network formed before thermal treatment.

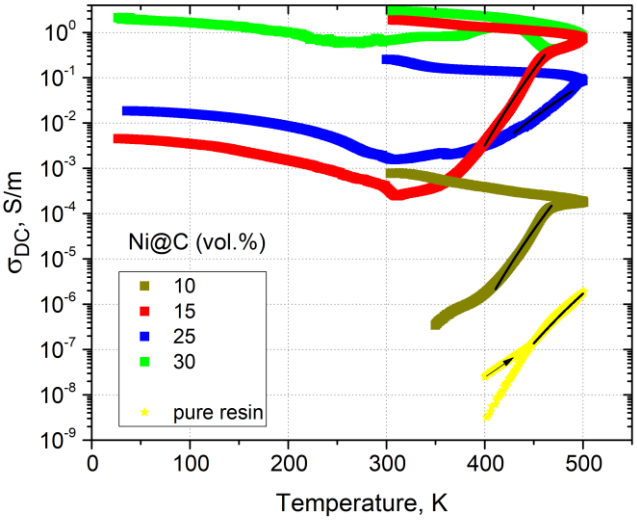

Figure 3.20: Temperature dependence of the DC conductivity of Ni@C / epoxy resin composites. Solid lines at high temperatures correspond to approximations according to Equation (3.3).

Cooling of unannealed samples from room temperature to 30 K is characterized by a monotonic increase in DC conductivity. A possible explanation is the epoxy resin compression during cooling, which reduces the

distance between the nanoparticles and, as a result, contributes to an increase in conductivity.

In the heating mode, the DC conductivity can be fitted by the Arrhenius law (Equation (3.3)). The Arrhenius behavior is typical for the thermally activated conductivity, which is observed, e. g., in pure epoxy resin[168]. Obtained parameters are presented in Table 3.6. The following observation can be made: the higher Ni@C concentration (and, consequently, the initial room temperature DC conductivity), the lower the activation energy (Table 3.6). This effect can be explained by the lower impact of the epoxy resin conductivity on the resultant composite conductivity at higher nanoparticles concentrations.

Table 3.6: Parameters of the Arrhenius law fits (according to Equation (3.3)) of the DC conductivity to the data of Figure 3.20.

Sample	Before Annealing	
	σ_0, S/m	E_A/k_B, K
10 vol.% Ni@C	$2.9 \cdot 10^9$	14314
15 vol.% Ni@C	$3.8 \cdot 10^{12}$	13886
25 vol.% Ni@C	$2.7 \cdot 10^5$	7579
30 vol.% Ni@C	$2.2 \cdot 10^6$	7436
Pure epoxy	$1.3 \cdot 10^4$	11363

Results of thermogravimetric analysis of MWCNTs, Ni@C nanoparticles, epoxy and composites with these inclusions are presented in Figure 3.21 (the data of 0.6 vol.% Ni@C+0.09 vol.% MWCNT sample linked to subchapter 3.2.2). The small weight decrease in the temperature range 300–600 K can be explained by the decrease of humidity. Therefore, it is possible to conclude that powders and composites are stable up to 600 K. The oxidation processes in powders, epoxy and composites start at higher temperatures (above 600 K) and are followed by a significant decrease in weight.

Thus, the selected temperature range for broadband investigations and for annealing (up to 500 K) is conditioned by two reasons: (i) the thermogravimetric analysis results (the composites stability up to 600 K) and (ii) the fact that epoxy resin heating above 400 K is characterized by changing properties of composites based on it[11,168].

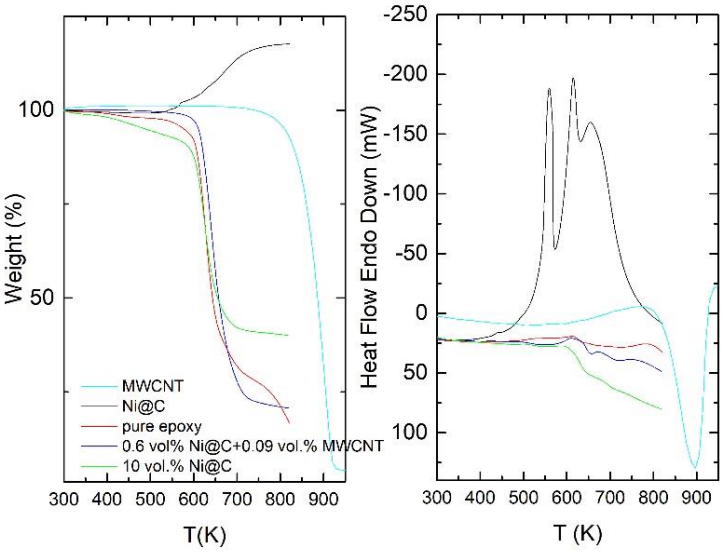

Figure 3.21: Thermogravimetric analysis of MWCNTs, Ni@C nanoparticles, epoxy and composites with these inclusions.

Relaxation time distributions

The procedure used for calculating the relaxation time distribution is described in detail in subchapter 1.5.

The calculated frequency dependences of complex impedance for Ni@C / epoxy resin composites before and after annealing at 500 K according to equations (1.21)-(1.22) are presented in Figure 3.22.

The frequency-independent plateau of Z' disappears and Z'' has a maximum close to the critical frequency (frequency at which the conductivity starts to increase from its DC conductivity plateau). The critical frequency position determines the relaxation time (the position of the relaxation time distribution maximum). For this reason, if the critical frequency is outside the investigated experimental frequency range, then it is not possible to determine quantitatively the relaxation time distribution. Thus, analyzing Figure 3.22, one can conclude that, among the studied samples, only for three of them, the relaxation time distributions are available from the collected experimental data: 15, 25 vol.% of Ni@C before annealing and 10 vol.% of Ni@C after annealing.

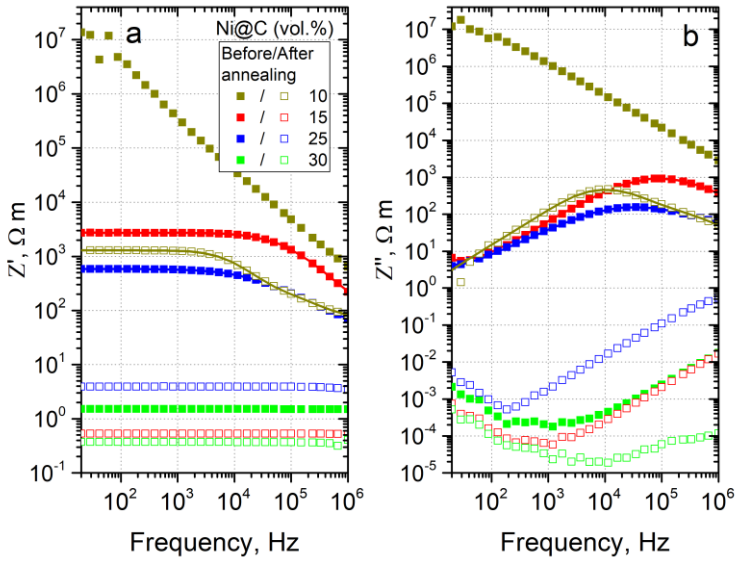

Figure 3.22: Frequency dependence of the complex impedance (calculated according to Equations (1.21)-(1.22)) for Ni@C / epoxy resin composites at room temperature before and after annealing at 500 K.

The obtained distributions of relaxation times are presented in Figure 3.23. Considering the interpretation of the distribution of relaxation times in percolative composites, the relaxation time defines as $\tau = RC = C/\sigma$, where C is the capacitance of one cluster of conductive nanoparticles, R is the resistivity and σ is the conductivity inside one cluster or between neighboring clusters. The capacitance of clusters is dependent only on the geometrical parameters of clusters, for example, if we assume spherical clusters, their capacitance is $C = 4\pi\varepsilon_0 r$, where r is the effective radius of clusters. The tunneling conductivity between clusters is also dependent on nanoparticles distribution inside the polymer matrix. Thus, short relaxation times in distributions correspond to the relaxation in small Ni@C clusters where they are distributed more homogeneously and long relaxation times correspond to large clusters of nanoparticles. From the distribution of relaxation times, it is difficult to speak about the real Ni@C geometrical shape distribution because the conductivity σ is also dependent on the Ni@C concentration (Figure 3.19) and on the potential barrier for electrons tunneling between clusters. Therefore, if the distribution of conductive nanoparticles is the same, the distribution of relaxation times should be observed at the shortest relaxation

times for composites with higher nanoparticles concentrations. In Figure 3.23 the opposite situation is observed: the distribution of relaxation times of composites with 15 vol.% of Ni@C corresponds to shorter relaxation times in comparison with the distribution of relaxation times of composites with 25 vol.% of Ni@C. This indicates a better distribution of Ni@C nanoparticles in composites with smaller Ni@C concentrations in good agreement with SEM investigations (Figure 3.18).

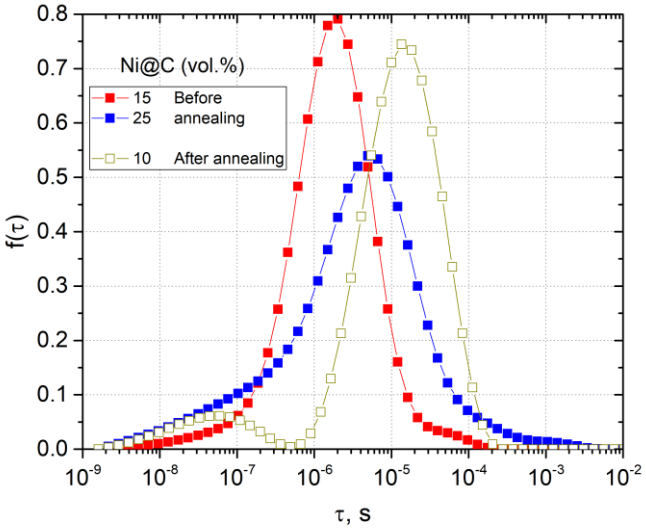

Figure 3.23: Relaxation time distributions (calculated according to Equation (1.23)) for Ni@C / epoxy resin composites at room temperature before and after annealing at 500 K.

Thus, the relaxation time distributions show a clear deviation from the classical percolation theory: a more conductive sample (25 vol.%) has a lower critical frequency (Figure 3.19) and, consequently, a longer relaxation time. After annealing, this effect is enhanced: the DC conductivity of 15 vol.% Ni@C/epoxy is higher than that of 25 vol.% Ni@C/epoxy. Thus, the physics coming from the analysis of dielectric spectra, in particular the dielectric relaxation spectroscopy, allows to estimate the nanoparticle distribution level in the polymer matrix.

Microwave shielding efficiency

The Ni@C / epoxy resin composites were analyzed in terms of the microwave shielding efficiency ability; the results for 2 mm-thick samples before annealing are presented in Table 3.7. The concentration increase leads to substantial attenuation of electromagnetic radiation in the microwave region, and the maximum concentration (30 vol.% Ni@C) transmits only 17% of the incident wave. Since DC conductivity exhibits a pronounced hysteresis after annealing (see Figure 3.20), expectedly that in microwaves the conductivity (and the dielectric permittivity imaginary part) will also increase, which should lead to the transmittance decrease even more. Thus, these materials are interesting for shielding applications.

Table 3.7: Shielding efficiency of 2 mm-thick Ni@C composite layer at the frequency of 30 GHz.

Sample	Reflectance, %	Transmittance, %	Absorbance, %
10 vol.% Ni@C	36	16	48
15 vol.% Ni@C	28	43	29
25 vol.% Ni@C	11	30	44
30 vol.% Ni@C	21	17	62

Percolation thresholds differences explanation

According to theoretical models, the percolation threshold of spherical particles is close to 30 vol% and does not depend on their size[152,184]. However, these models consider the percolation as a geometric phenomenon, when micron-sized particles uniformly distributed in a unit volume are in mechanical contact. When it comes to the percolation from an electrical point of view, the particles do not have to touch, there may be a characteristic distance (tunneling distance) between them, through which the electron can tunnel, overcoming the potential barrier. Moreover, when passing from micron-sized particles to nanoscale, the percolation threshold can decrease when the particle size becomes commensurate with the tunneling distance[185–187].

Thus, in our case, epoxy-based composite systems filled with two types of spherical particles of different nature, but close size (manganese ferrite $MnFe_2O_4$ and carbon-coated nickel nanoparticles Ni@C), demonstrate

significantly different percolation thresholds. For $MnFe_2O_4$, the percolation threshold is close to 30 vol%, which is in agreement with theoretical predictions. For Ni@C, the percolation threshold is much lower, between 10 and 15 vol%. According to the literature, real composite systems based on polymer matrices with spherical particles can have a wide range of percolation thresholds: from 10 to 30 vol.%[188–194]. Generally, the percolation threshold depends on the filler particles shape, their size, polymer, manufacturing technology, spatial distribution of the filler in the matrix, and the interaction between the filler and the host polymer[188,195]. In our case, only the last two factors can differ. In this regard, two possible explanations of the differences in the percolation thresholds can take place. Assuming the particles distribution in both systems is equally uniform, then the difference is determined by the interaction between the filler and the host polymer: different contact resistance due to different wetting[188,195]. However, a second explanation related to the spatial distribution of the filler in the matrix can also be valid. There are known studies where spherical particles (for example, carbon black), forming small aggregates, demonstrate a lower percolation threshold than in the case of individual isolated particles[196,197]. This is due to the fact that the formed aggregates have an aspect ratio greater than one (unlike the case of the isolated spherical particles), which means that the probability of meeting a neighboring particle to create a percolation network is higher. Such a situation, when the percolation threshold is lower for the case with non-perfect distribution, is called a favorable segregated geometry[189,194,198,199]. Small nano-sized spherical particles are not presentable in panoramic SEM images, therefore it is impossible to conclude unequivocally. However, in any case, the experimental results show that Ni@C nanoparticles are able to create a percolation network at lower concentrations.

3.1.4 Summary

Three types of epoxy resin composite systems based on different magnetic nanoparticles have been studied.

The dielectric properties of $Fe_2O_3 \cdot H_2O$ nanorods / epoxy resin composites have been studied in a wide frequency range from hertz to terahertz at temperatures of 200-450 K. The percolation threshold in this system is close to 40 vol.%.

The dielectric properties of $MnFe_2O_4$ / epoxy resin composites with two different sizes of spherical-shaped particles (28 and 60 nm) have been studied in the frequency range from 20 Hz to 1 MHz and temperature range of 150-500 K. It was demonstrated that the percolation thresholds in these composites are 30 and 29.3 vol.% for small and large $MnFe_2O_4$ nanoparticles, respectively. The minor difference in the percolation threshold value is related to the better distribution of larger nanoparticles.

The following several common features for $Fe_2O_3 \cdot H_2O$ / epoxy and $MnFe_2O_4$ / epoxy systems are observed. The dielectric behavior of composites below the percolation threshold is mainly determined by relaxation in a pure polymer matrix. The dielectric properties of composites above the percolation threshold are determined by the percolation network, which is formed by the filler particles inside the composite. At low frequencies, the DC conductivity is produced by the random distribution of electric charge carriers and increases with the filler concentration. At high temperatures, because of the finite conductivity of the epoxy resin, DC electrical conductivity occurs in the composites both above and below the percolation threshold. The activation energy decreases with fillers concentration indicating that the electrical transport occurs together in fillers and epoxy matrix subsystems.

The dielectric/electric properties of the Ni@C / epoxy resin composites have been studied in broad frequency (20 Hz-40 GHz) and temperature (30–500 K) ranges. For such a system, it was possible to roughly estimate the percolation threshold, which is in the range between 10 and 15 vol.%. Additional annealing of these composites up to 500 K substantially decreases the percolation threshold down to below 10 vol.%. However, with a Ni@C concentration increase, the nanoparticles dispersion quality in the polymer is suppressed dramatically. This is proved by the SEM micrographs and the analysis of relaxation time distributions. Moreover, Ni@C / epoxy resin composites demonstrate substantial attenuation of electromagnetic radiation in the microwave region, thus, these materials are interesting for shielding applications.

3.2 Dielectric relaxation spectroscopy and synergy effects in ternary hybrid epoxy-based composites with multi-walled carbon nanotubes and magnetic nanoparticles

Polymer composites loaded with carbon nanoparticles have attracted superior attention due to the variety of their electric, mechanical and thermal properties, a wide range of their functionalities and multifunctionalities, followed by the possibility of fine tuning/control of their specific features by playing with the fillers concentrations, fabrication methods, matrices origins and applying external forces[7,8]. The high aspect ratio carbon nanotubes (CNTs) give conductive properties to the insulating matrices at their sufficiently low content up to 1-2 wt.%[200]. However, huge Van der Waals forces between individual CNTs lead to their agglomeration, which increases the percolation threshold (some critical concentration at which sharp insulator-conductor transition occurs[201]). Rising the CNTs concentration not only makes the composite manufacturing process more laborious, but also might impair the mechanical properties of the resultant polymer product. Moreover, CNTs are expensive and might be toxic[202]. Therefore, reducing the electrical percolation threshold along with simultaneously maintaining the optimal mechanical properties of the polymer composites at as low as possible amount of expensive and toxic filler is still an actual problem.

One of the possible solutions is the development of hybrid multifunctional composite materials containing two or more nanofillers. Often, due to the proper distribution of several different fillers in the matrix and their simultaneous participation in the percolation network formation, synergy effects can occur[37]. Mostly, the electrical conductivity improvement of a multiphase composite is accompanied by a decrease in the percolation threshold compared to monofiller composite series. A considerable number of papers have been published with successful detection of synergy effects of different carbon allotropes[37,39–41]. Composites with the combination of particles of different natures (carbon and non-carbon) can have optimal dielectric and magnetic properties[42–46]. In particular, the introduction of cobalt nanoparticles inside MWCNTs led not only to a substantial increase in electrical conductivity, but also stimulated the emergence of ferromagnetism as well[203]. Such multiphase systems are especially interesting for solving the problems of electromagnetic compatibility, since the regulation of the dissimilar particles ratio leads to a variation of dielectric and magnetic losses with the electromagnetic response control[47,204,205]. For instance, it has been shown that composites with $MnFe_2O_4$ coated multi-walled carbon nanotubes

(MWCNTs) are very appealing for electromagnetic shielding tasks[206]. However, the dielectric properties of hybrid composites combining $MnFe_2O_4$ and MWCNTs, as well as hybrid composites with Ni@C and MWCNTs have not been studied yet.

This subchapter is devoted to the dielectric/electric properties experimental investigations of epoxy/MWCNT/$MnFe_2O_4$ and epoxy/MWCNT/Ni@C hybrid composites systems in order to discover the possible synergy between constituent components.

3.2.1 Epoxy / MWCNT / $MnFe_2O_4$ hybrid composites

Room-temperature region

Scanning electron microscopy micrographs of epoxy/MWCNT/$MnFe_2O_4$ hybrid composites with 0.09 vol.% of MWCNTs and 0.025, 0.35, and 0.65 vol.% of $MnFe_2O_4$ at the same middle magnification are presented in Figure 3.24. It can be concluded that the best distribution of MWCNTs was observed for composites with the lowest $MnFe_2O_4$ concentration (0.025 vol.%). With increasing $MnFe_2O_4$ content, MWCNT agglomerates were more pronounced. The SEM-micrograph with low magnification (see Figure 3.25a) proved that MWCNTs could disperse uniformly in the epoxy resin matrix. Due to the low $MnFe_2O_4$-content and their nanometer particle size, a high magnification was required to detect them (see Figure 3.25b).

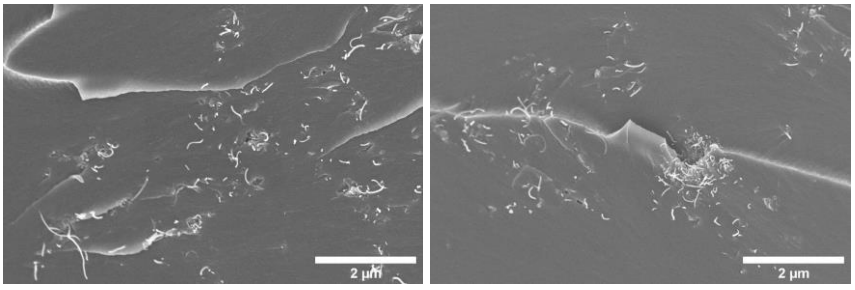

a b

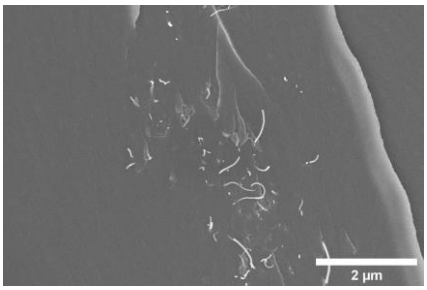

c

Figure 3.24: Scanning electron microscopy images of epoxy/MWCNT/$MnFe_2O_4$ hybrid composites with 0.09 vol.% of MWCNTs and (a) 0.025, (b) 0.35, and (c) 0.65 vol.% of $MnFe_2O_4$.

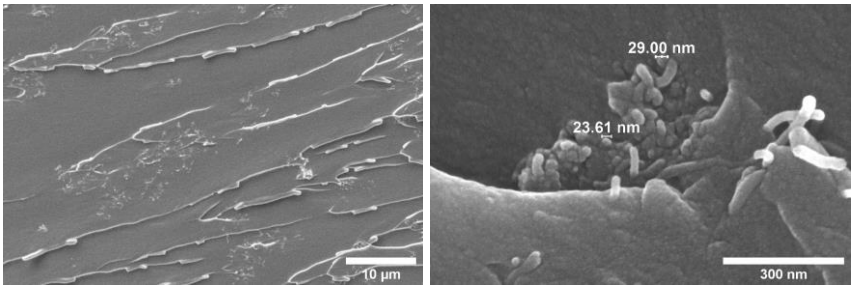

a b

Figure 3.25: Scanning electron microscopy images of epoxy/MWCNT/$MnFe_2O_4$ hybrid composites with 0.09 vol.% of MWCNTs and 0.025 vol.% of $MnFe_2O_4$ at (a) low and (b) high magnifications.

Frequency dependencies of the real part of dielectric permittivity (ε') and the electrical conductivity (σ) of epoxy/MWCNT/$MnFe_2O_4$ hybrid composites at room temperature are presented in Figure 3.26.

At low frequencies (below 1 MHz), the dielectric permittivity and the electrical conductivity of composites are strongly dependent on $MnFe_2O_4$ concentration.

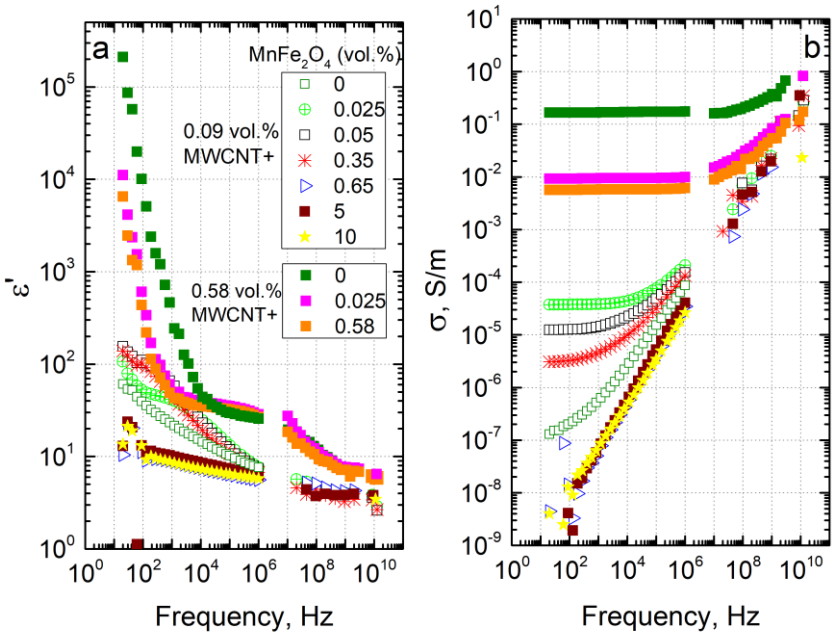

Figure 3.26: Frequency dependencies of (a) the real part of dielectric permittivity and (b) the electrical conductivity of epoxy/MWCNT/$MnFe_2O_4$ hybrid composites at room temperature.

In the case of the first sample series with an MWCNT concentration of 0.09 vol.%, after the addition of a small amount of $MnFe_2O_4$ (0.025 vol.%) to the initially non-conductive composite (open green symbols in Figure 3.26), the hybrid composite became conductive and its conductivity value increased by three orders of magnitude. With a further increase in $MnFe_2O_4$ content (0.05 and 0.35 vol.%), the electrical conductivity decreased and at the three highest concentrations (0.65, 5, and 10 vol.%), the samples became fully non-conductive (the σ_{DC} conductivity plateau is absent) with σ values even lower than that for composites without $MnFe_2O_4$. This maximum of σ close to the 0.025 vol.% of $MnFe_2O_4$ was visually pronounced on the corresponding concentration dependence at room temperature and 129 Hz, as shown in Figure 3.27a (the results of ε' and σ are presented before and after annealing at 500 K).

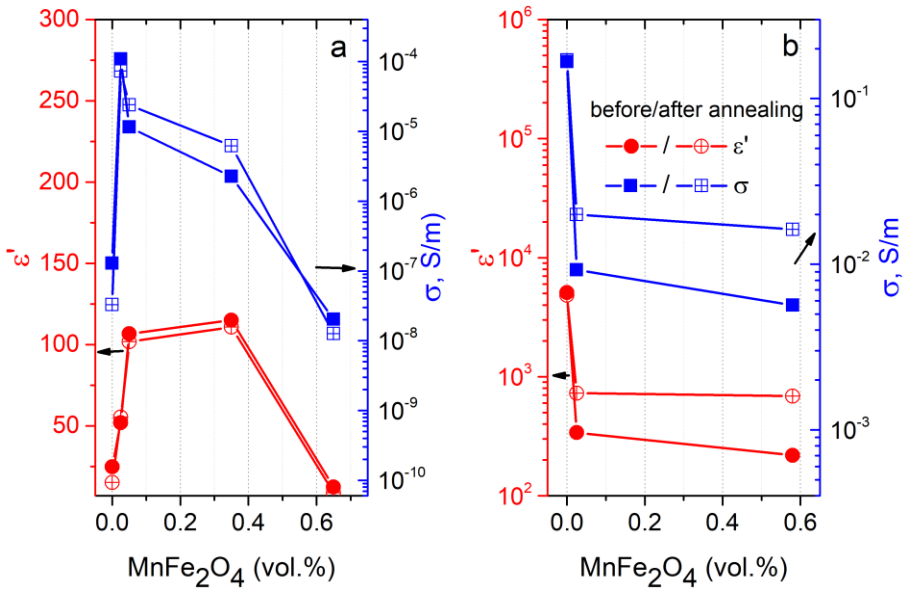

Figure 3.27: $MnFe_2O_4$-concentration dependencies of the real part of dielectric permittivity and electrical conductivity of epoxy/MWCNT/$MnFe_2O_4$ hybrid composites with (a) 0.09 vol.% and (b) 0.58 vol.% of MWCNTs at room temperature and 129 Hz before and after annealing at 500 K.

Thus, in this composite series with a pre-percolation MWCNT content, one can observe a synergy effect between two fillers, which takes place only at certain small amounts of $MnFe_2O_4$. This result can be partially explained by the analysis of the SEM-micrographs. The best MWCNT distribution was observed for the sample with a minimum $MnFe_2O_4$ concentration. In addition, electrical transport could occur between the MWCNT and $MnFe_2O_4$ clusters, and this mechanism should lead to the rise in the total composite conductivity. However, its contribution to the total conductivity is obviously much smaller than the tunneling conductivity between the MWCNT clusters.

In the case of the second sample series with a high MWCNT concentration of 0.58 vol.%, after the addition of any small (0.025 vol.%) or relatively large (0.58 vol.%) amounts of $MnFe_2O_4$ to the initially conductive composite, the absolute values of electrical conductivity became smaller (see Figures 3.26 and 3.27b). Thus, in the case of an initially well-formed percolation network of nanotubes, any amount of magnetic $MnFe_2O_4$ particles leads to a decrease

in electrical conductivity. This means that there is no synergy effect for this sample series. The observed effect can be explained by the worse distribution of MWCNTs after the addition of $MnFe_2O_4$ nanoparticles.

Temperature-dependent region

The temperature dependencies of DC conductivity in a wide temperature range are presented in Figure 3.28. For two composites from the first series (with 0.09 vol.% of MWCNTs and 0 and 0.65 vol.% of $MnFe_2O_4$), which were initially non-conductive at room temperature, DC conductivity appeared only at high temperatures (above 400 K). This is due to the fact that at high temperatures, the epoxy resin becomes conductive (yellow curve in Figure 3.28)[11,182]. A similar DC conductivity behavior was observed for other non-conductive composites at room temperature (5 and 10 vol.% of $MnFe_2O_4$).

For these composites, which are initially conductive at room temperature, the following DC conductivity behavior features were observed. First, during heating from room temperature to 400–450 K (depending on the particular sample), the DC conductivity slightly decreased due to the thermal expansion of epoxy resin and the increase in the distance between the particles[168,182]. Then, the DC conductivity began to increase up to 500 K (epoxy resin contribution). Cooling from 500 K to room temperature had a similar tendency, the difference was mainly in the absolute value of DC conductivity. Basically, after annealing at 500 K, the DC conductivity at room temperature increased, which indicates that some redistribution of particles in the matrix occurs (large conductive agglomerates broke up into small ones)[168,182,183]. However, one composition (with 0.09 vol.% of MWCNTs and 0.025 vol.% of $MnFe_2O_4$) showed the opposite behavior. Due to the smallest $MnFe_2O_4$ and MWCNT concentrations, the distance between the particles was the largest, therefore the percolation network was the most unstable, and its partial destruction was possible after annealing due to the rapid thermal expansion of the polymer matrix. Further cooling from room temperature to 30 K is characterized by a gradual decrease of DC conductivity. The inflections in the electrical conductivity data around 375–400 K can be related to the occurrence of the glass transition[182].

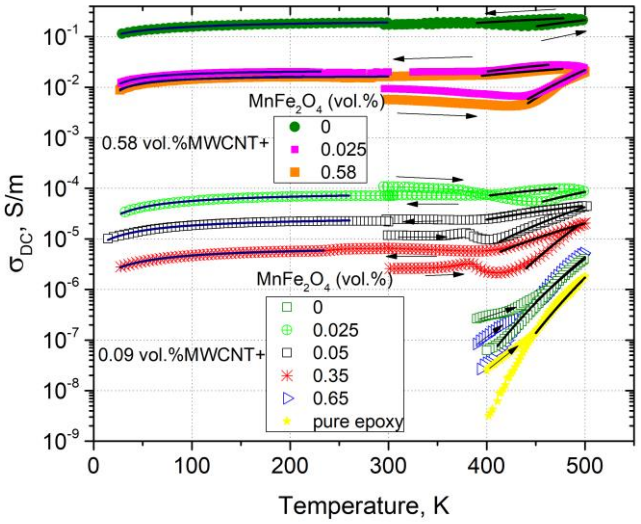

Figure 3.28: Temperature dependence of the DC conductivity of epoxy/MWCNT/$MnFe_2O_4$ hybrid composites. Solid lines at high and low temperatures correspond to approximations according to Equations (3.3) and (3.4), respectively.

At high temperatures, σ_{DC} can be fitted by the Arrhenius law (Equation (3.3)). Obtained parameters are presented in Table 3.8. In the composite series with 0.09 vol.% MWCNTs, the activation energy showed the minimum at the $MnFe_2O_4$ concentration of 0.025 vol.%, which corresponded to the maximum of conductivity (see Figure 3.27a). In the composite series with 0.58 vol.% MWCNTs, the lowest activation energy was observed for the most conductive sample (without $MnFe_2O_4$); for the two other samples, E_A had close values. In addition, for both series, the activation energy decreased after annealing. Thus, it can be concluded that the lowest activation energy is typical for the highest electrical conductivity composites as the contribution of the matrix electrical conductivity was insufficient for these composites.

Table 3.8: Parameters of the Arrhenius law fits (according to Equation (3.3)) of the DC conductivity to the data of Figure 3.28.

Sample	Before Annealing		After Annealing	
	σ_0, S/m	E_A/k_B, K	σ_0, S/m	E_A/k_B, K
Pure epoxy	$1.3\cdot10^{4}$	11363	$1.6\cdot10^{5}$	12433
0.09 vol.% MWCNT	$2.2\cdot10^{2}$	8892	$5.6\cdot10^{2}$	9338
0.09 vol.% MWCNT+ 0.025 vol.% $MnFe_2O_4$	$9.5\cdot10^{-3}$	2357	$6.7\cdot10^{-4}$	898
0.09 vol.% MWCNT+ 0.05 vol.% $MnFe_2O_4$	$7.5\cdot10^{-2}$	3736	$5.7\cdot10^{-4}$	1266
0.09 vol.% MWCNT+ 0.35 vol.% $MnFe_2O_4$	$2.0\cdot10^{2}$	7998	$1.0\cdot10^{-2}$	3103
0.09 vol.% MWCNT+ 0.65 vol.% $MnFe_2O_4$	$4.1\cdot10^{4}$	11380	$1.7\cdot10^{3}$	9755
0.58 vol.% MWCNT	3.0	1272	$0.58\cdot10^{-1}$	446
0.58 vol.% MWCNT+ 0.025 vol.% $MnFe_2O_4$	$5.0\cdot10^{2}$	5056	$1.9\cdot10^{-1}$	897
0.58 vol.% MWCNT+ 0.58 vol.% $MnFe_2O_4$	$1.6\cdot10^{3}$	5623	$1.1\cdot10^{-1}$	724

At low temperatures, the DC conductivity fitted well according to the tunneling model[207]:

$$\sigma_{DC} = \sigma_0 exp\left(\frac{-T_1}{T+T_0}\right) \tag{3.4}$$

where σ_0 is the pre-exponential factor; T_1 represents the energy required for an electron to cross the insulator gap between the conductive particle aggregates; and T_0 is the temperature above which thermally activated conduction over the barriers begins to occur.

In the tunneling model, parameters T_1 and T_0 are determined by $T_1 = wA\beta_0/8\pi k_B$ and $T_0 = 2T_1/\pi\chi w$ expressions, respectively. Here, $\chi = \sqrt{2mV_0}/\hbar$ and $\beta_0 = 4V_0/ew$; m and e are the electron mass and charge, respectively; V_0 is the potential barrier amplitude; w is the inter-particles distance (gap width); A is the area of capacitance formed by the junction; ħ is the Dirac constant; and π is the pi number. Obtained parameters are presented in Table 3.9. The ratio T_1/T_0 is proportional to the gap width w and the potential barrier V_0 amplitude. Indeed, according to the last column in Table 3.9, for composites with a 0.09 vol.% of MWCNTs, the highest value

of the T_1/T_0 ratio was observed for the lowest concentrations of $MnFe_2O_4$ due to the large potential barrier V_0 amplitude for particle tunneling. The importance of the potential barrier V_0 amplitude for the electrical transport mechanism was also clearly observed for hybrid composites with a 0.58 vol.% of MWCNTs, where the ratio T_1/T_0 was the largest for composites with the middle values of the conductivity and distances between nanoparticles. Thus, at low temperatures, the main transport mechanism is electron tunneling through the potential barrier, and $MnFe_2O_4$ is the factor that can tune the potential barrier.

Table 3.9: Tunneling model parameters (according to Equation (3.4)) to the data of Figure 3.28.

Sample	σ_0, S/m	T_1, K	T_0, K	T_1/T_0
0.09 vol.% MWCNT+ 0.025 vol.% $MnFe_2O_4$	$8.7\cdot10^{-5}$	55.3	26.2	2.1
0.09 vol.% MWCNT+ 0.05 vol.% $MnFe_2O_4$	$2.8\cdot10^{-5}$	59.5	40.4	1.5
0.09 vol.% MWCNT+ 0.35 vol.% $MnFe_2O_4$	$7.3\cdot10^{-6}$	59.3	32.9	1.8
0.58 vol.% MWCNT	$2.1\cdot10^{-1}$	49.2	47.4	1.0
0.58 vol.% MWCNT+ 0.025 vol.% $MnFe_2O_4$	$2.2\cdot10^{-2}$	20.7	5.3	3.9
0.58 vol.% MWCNT+ 0.58 vol.% $MnFe_2O_4$	$1.8\cdot10^{-2}$	27.3	11.6	2.4

The electrical properties of the composites can also be characterized in terms of the critical frequency. The critical frequency f_{cr} is the frequency at which the DC conductivity plateau passes into the frequency-dependent region. It is possible to calculate f_{cr} from the σ frequency spectra (see Figure 3.26). The critical frequency for all composites with the MWCNT concentration of 0.58 vol.% was higher than 1 MHz. The results f_{cr} for conductive composites with an MWCNT concentration of 0.09 vol.%. are presented in Figure 3.29. The temperature dependence (from 500 K to 30 K) of the critical frequency has a basically similar behavior as the temperature dependence of DC conductivity (see Figure 3.28) for the corresponding samples. The $MnFe_2O_4$ concentration increase, and the critical frequency

decrease. The information about the critical frequency before annealing can be obtained from the inset of Figure 3.29.

The temperature dependence of the critical frequency mainly correspond to the temperature dependence of DC conductivity according to the relations[182,207]:

$$f_{cr} = \frac{\sigma_{DC}}{\varepsilon_0 \varepsilon_s} \tag{3.5}$$

$$\sigma_{DC} \sim f_{cr}^{z} \tag{3.6}$$

where ε_s is a static permittivity and z is an exponent, which characterizes the relation between capacitive and conductive networks in the composite. Above 400 K, both the DC conductivity and critical frequency strongly increase with temperature and the z value was close to 0.5. This value corresponds to the strong variation of conductivity and the weak variation of permittivity on the gaps between clusters[208]. After annealing, the critical frequency also increases together with DC conductivity (Figures 3.27 and 3.29 inset).

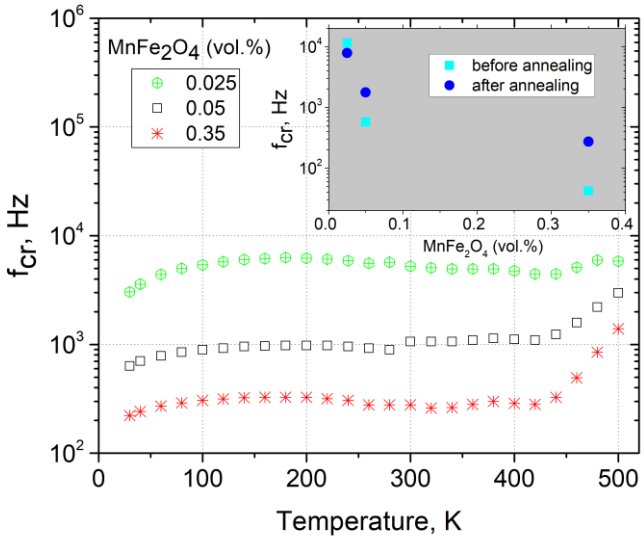

Figure 3.29: Temperature dependence of critical frequency for epoxy/MWCNT/$MnFe_2O_4$ hybrid composites with 0.09 vol.% of MWCNTs (Insert: critical frequency versus $MnFe_2O_4$ concentration at room temperature before and after annealing at 500 K).

Relaxation time distributions

Experimental data of complex dielectric permittivity was converted to complex impedance ($Z = Z' - iZ''$) using the Equations (1.21)-(1.22). The results are presented in Figure 3.30. The frequency at which the frequency-independent plateau of Z' disappears and the Z'' has a maximum is close to the critical frequency f_{cr}, as discussed earlier. This critical frequency f_{cr} is related to the relaxation time τ by a simple expression:

$$2\pi f_{cr}\tau = 1 \qquad (3.7)$$

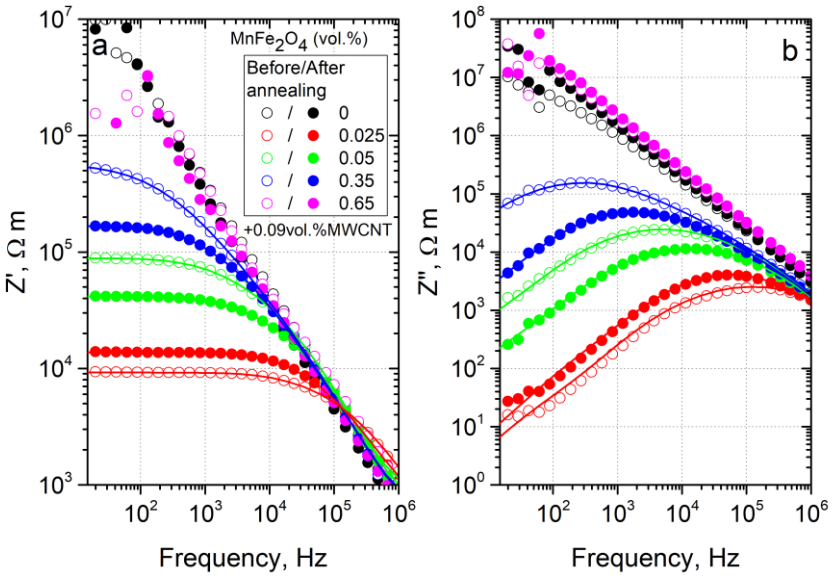

Figure 3.30: Frequency dependence of the complex impedance (calculated according to Equations (1.21)-(1.22)) for epoxy/MWCNT/$MnFe_2O_4$ hybrid composites at room temperature before and after annealing at 500 K.

However, since the considered composites are heterogeneous systems consisting of particles with a size and shape dispersion, their relaxation time has some distribution $f(\tau)$. Since this relaxation is a Maxwell–Wagner one, the relaxation time distribution can be obtained from complex impedance by solving integral equation (Equation (1.23)). The obtained distributions of relaxation times before and after annealing are presented in Figure 3.31. The distributions were calculated only for those samples where the τ value was within the experimental range under consideration. The distributions were symmetrical for all presented samples. The relaxation time of the system was

directly related to its conductivity (Equations (3.6)-(3.7)), while the distributions of the relaxation times were related to the distribution of nanoparticles inside the polymer matrix in accordance with the data presented in Figures 3.24-3.25[209]. Exactly the same pattern can be observed in Figure 3.31, which completely correlates with the conductivity behavior (see Figures 3.27a or 3.28).

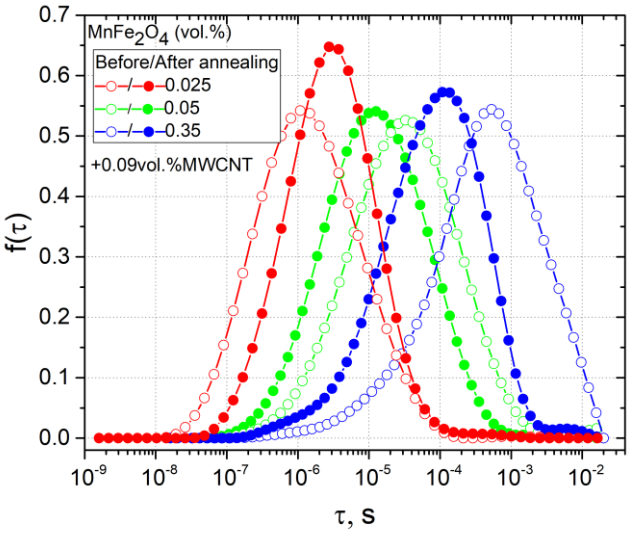

Figure 3.31: Relaxation time distributions (calculated according to Equation (1.23)) for epoxy/MWCNT/$MnFe_2O_4$ hybrid composites at room temperature before and after annealing at 500 K.

3.2.2 Epoxy / MWCNT / Ni@C hybrid composites

Room-temperature region

The MWCNTs distribution in the composite without Ni@C is rather homogeneous (see Figure 3.32a). However, Figure 3.32b,c clearly shows that an increase of Ni@C concentration from 0.6 to 1 vol.% in epoxy/MWCNT/Ni@C hybrid composites is accompanied by an MWCNTs distribution deterioration (an increase of the agglomerates number).

In order to see the macroscopic distribution of MWCNTs, the panoramic SEM images of epoxy/MWCNT/Ni@C hybrid composites are presented in

Figure 3.33 (MWCNT clusters are observed as black spots, which are confirmed by higher resolution SEM pictures). The MWCNT network is clearly observed in composites with 0.6 vol.% of Ni@C (Figure 3.33b), in composites with 1 vol.% clusters of MWCNT are uniformly distributed, while in composites without Ni@C, no macroscopic structure of the MWCNT is observed. This is in good agreement with previously reported results that the MWCNT clustering can decrease the percolation threshold value[201]. Smaller Ni@C clusters act as separators of MWCNT clusters (Figure 3.32b) and support certain macroscopic structures of the MWCNT network (Figure 3.33b,c).

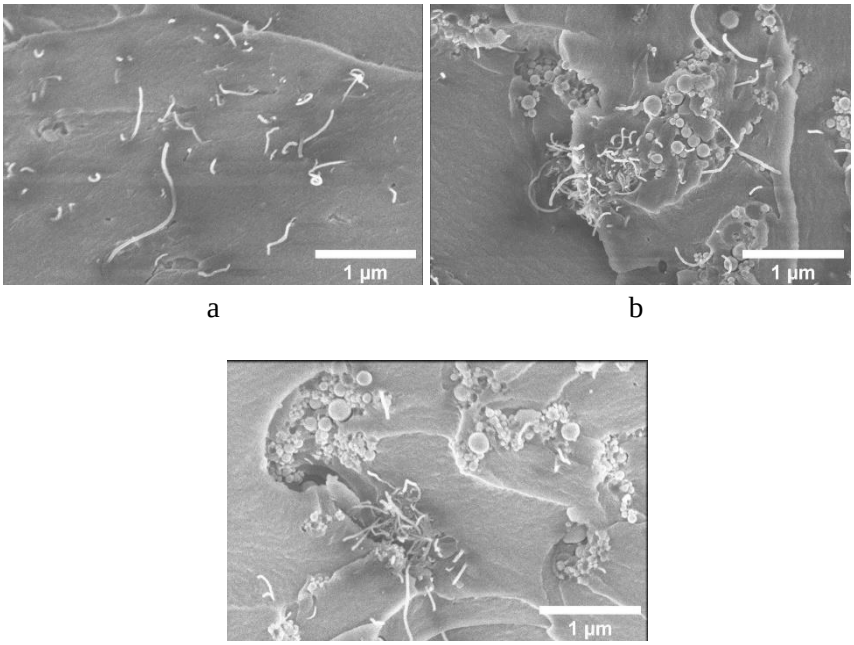

a b

c

Figure 3.32: Scanning electron microscopy images of epoxy/MWCNT/Ni@C hybrid composites with 0.09 vol.% of MWCNTs and (a) 0, (b) 0.6, and (c) 1 vol.% of Ni@C.

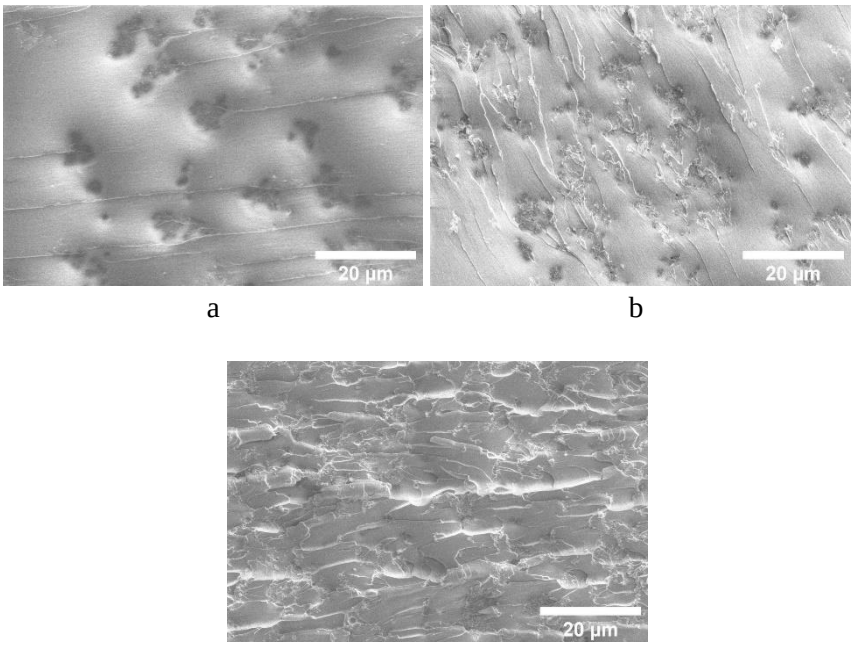

a b

c

Figure 3.33: Panoramic scanning electron microscopy images of epoxy/MWCNT/Ni@C hybrid composites with 0.09 vol.% of MWCNTs and (a) 0, (b) 0.6, and (c) 1 vol.% of Ni@C.

The frequency and concentration dependencies of ε' and σ for epoxy/MWCNT/Ni@C hybrid composites at room temperature are presented in Figures 3.34 and 3.35, respectively.

The addition of Ni@C to initially non-conductive composite with MWCNTs (a pre-percolation state) causes the appearance of the DC conductivity. The DC conductivity changes in a non-monotonically manner with increasing Ni@C concentration. First, the σ_{DC} increases, then, having reached a maximum at the Ni@C concentration of 0.2 vol.%, it begins decreasing. This indicates the synergy effect between two fillers at low Ni@C content. Perhaps small Ni@C clusters, located between the nanotubes, help them to complete the formation of the MWCNTs percolation network. Small Ni@C amounts up to 0.2 vol.% improve the MWCNTs dispersion in the polymer matrix, while at higher Ni@C concentrations an increase of the agglomerates number and, as a consequence, an MWCNTs distribution deterioration is observed (see SEM-images in Figure 3.32).

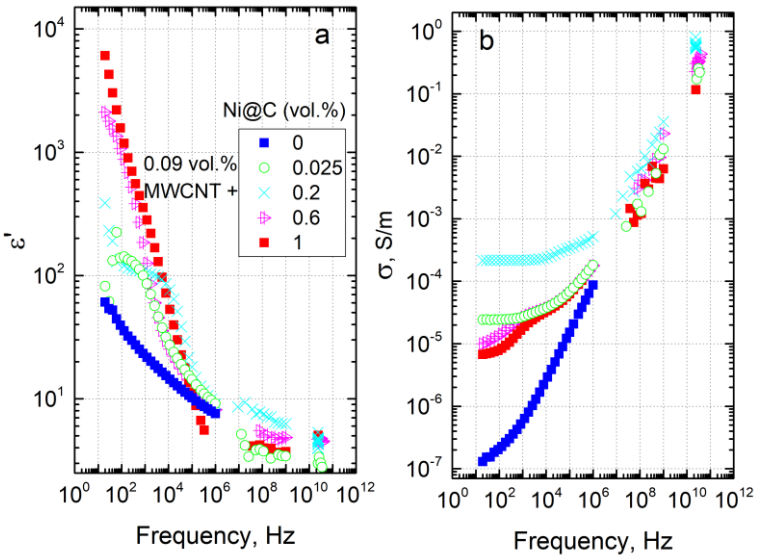

Figure 3.34: Frequency dependencies of the real part of dielectric permittivity and the electrical conductivity of epoxy/MWCNT/Ni@C hybrid composites at room temperature.

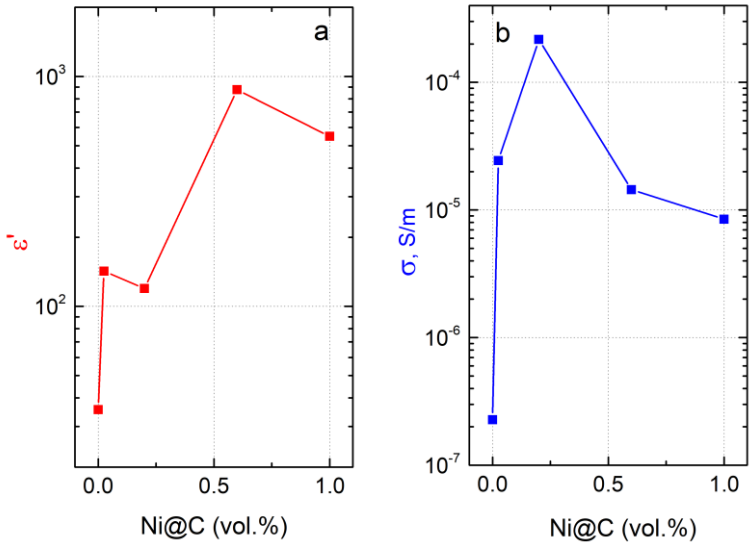

Figure 3.35: Ni@C-concentration dependencies of the real part of dielectric permittivity and the electrical conductivity of epoxy/MWCNT/Ni@C hybrid composites with fixed MWCNTs content of 0.09 vol.% at room temperature and 129 Hz.

Temperature-dependent region

The temperature dependencies of DC conductivity in a wide temperature range for epoxy/MWCNT/Ni@C hybrid composites are presented in Figure 3.36.

In the sample without Ni@C the DC conductivity is observed only at temperatures above 400 K due to the epoxy resin contribution. All composites with Ni@C have qualitatively similar temperature dependencies of σ_{DC}. The temperature sections from room temperature to 500 K and from 500 K to room temperature have the character that was observed for the heating area in the monofiller Ni@C / epoxy resin composite series (presented in subchapter 3.1.3). The only difference is the temperature intervals of each separate zone (see Figure 3.36 for more details). All samples from the epoxy/MWCNT/Ni@C hybrid series are also characterized by hysteresis, but this is accompanied by a decrease of DC conductivity after annealing at room temperature. This may be due to the partial destruction of the percolation network after annealing. At high temperatures, the σ_{DC} before and after annealing is well fitted by the Arrhenius law according to Equation (3.3) with approximation parameters presented in Table 3.10. Before annealing, the minimum activation energy is characteristic for the sample with the lowest Ni@C concentration (0.025 vol.%). After annealing, the activation energy completely correlates with the DC conductivity values: the higher σ_{DC} , the lower E_A. In this case, the minimum activation energy is observed for the most conductive sample of 0.2 vol.% Ni@C. Similarly, as in the case of monofiller Ni@C/epoxy resin composites (subchapter 3.1.3) the lowest activation energy indicates the lowest contribution of polymer matrix conductivity to the total conductivity of composite, because the electrical conductivity of the percolation network is much bigger.

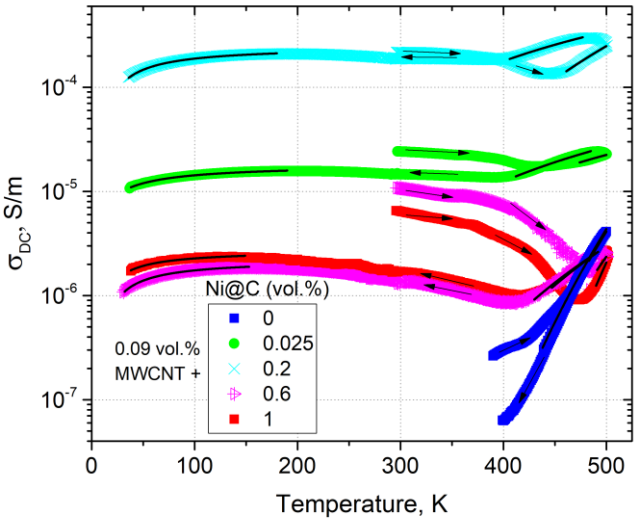

Figure 3.36: Temperature dependence of the DC conductivity of epoxy/MWCNT/Ni@C hybrid composites. Solid lines at high and low temperatures correspond to approximations according to Equations (3.3) and (3.4), respectively.

Table 3.10: Parameters of the Arrhenius law fits (according to Equation (3.3)) of the DC conductivity to the data of Figure 3.36.

Sample	Before Annealing		After Annealing	
	σ_0, S/m	E_A/k_B, K	σ_0, S/m	E_A/k_B, K
0.09 vol.% MWCNT	$4.1 \cdot 10^{2}$	9213	$5.1 \cdot 10^{2}$	9284
0.09 vol.% MWCNT+ 0.025 vol.% Ni@C	$4.8 \cdot 10^{-4}$	1532	$5.7 \cdot 10^{-4}$	1527
0.09 vol.% MWCNT+ 0.2 vol.% Ni@C	$1.8 \cdot 10^{-1}$	3302	$4.7 \cdot 10^{-3}$	1308
0.09 vol.% MWCNT+ 0.6 vol.% Ni@C	$2.3 \cdot 10^{1}$	8049	$4.0 \cdot 10^{-3}$	3601
0.09 vol.% MWCNT+ 1 vol.% Ni@C	$1.9 \cdot 10^{5}$	12634	$7.1 \cdot 10^{-3}$	3887

Cooling of the annealed samples from room temperature to 30 K is characterized by a monotonic DC conductivity decrease. On the low-temperature region, the σ_{DC} is fitted well according to the tunneling model

(Equation (3.4))[207]. Obtained parameters are presented in Table 3.11. The ratio T_1/T_0 is proportional to the gap width w and the potential barrier V_0 amplitude. The minimum of T_1/T_0 is observed at 0.025 vol.% Ni@C, which is close to the optimal concentration (0.2 vol.% Ni@C) for electrical properties. Thus, at low temperatures, the main transport mechanism is electron tunneling through the potential barrier. Obviously, the tunneling conductivity is the typical electrical transport mechanism also in monofiller Ni@C/epoxy resin composites series. However, due to the small size of Ni@C nanoparticles, the value of T_1 is very low and the tunneling conductivity could be observed at very low temperatures (lower than that available by our experimental technique).

Table 3.11: Tunneling model parameters (according to Equation (3.4)) to the data of Figure 3.36.

Sample	σ_0, μS/m	T_1, K	T_0, K	T_1/T_0
0.09 vol.% MWCNT+ 0.025 vol.% Ni@C	18	28.1	17.7	1.6
0.09 vol.% MWCNT+ 0.2 vol.% Ni@C	250	28.1	4.5	6.2
0.09 vol.% MWCNT+ 0.6 vol.% Ni@C	2.2	24.6	2.7	9.1
0.09 vol.% MWCNT+ 1 vol.% Ni@C	2.7	18.5	3.8	4.9

Relaxation time distributions

The frequency dependences of complex impedance and relaxation time distributions for epoxy/MWCNT/Ni@C hybrid composites before and after annealing at 500 K are presented in Figures 3.37 and 3.38, respectively. Before annealing, the relaxation time distributions are not symmetric; however, one should trust the short-time maxima, because the additional maximum at longer relaxation times is related to nonohmic contacts. After annealing, the relaxation time distributions become symmetric for all composites, and the maxima of $f(\tau)$ shifts towards longer relaxation times, which corresponds to the conductivity decrease. The shortest relaxation time is observed for the sample with the best Ni@C nanoparticles distribution (0.2 vol.%). Moreover, for this sample the DC conductivity (and, consequently, the nanoparticles distribution) almost does not change after

annealing (see Figure 3.36), while for the rest of the samples the σ_{DC} deteriorates significantly.

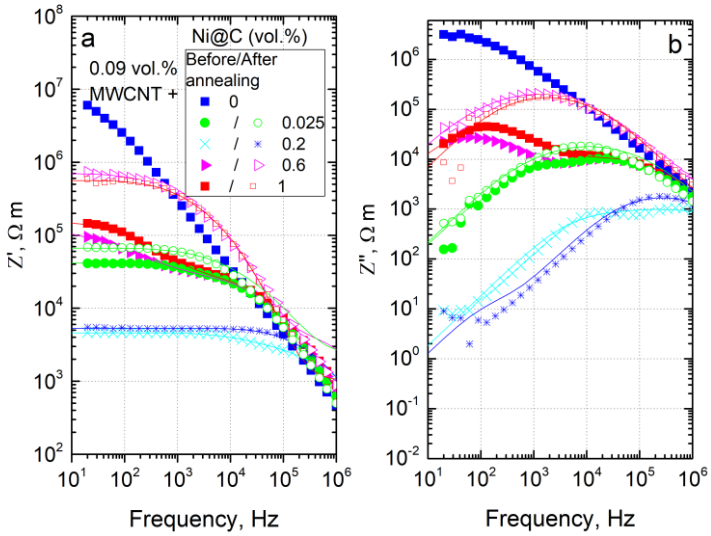

Figure 3.37: Frequency dependence of the complex impedance (calculated according to Equations (1.21)-(1.22)) for epoxy/MWCNT/Ni@C hybrid composites at room temperature before and after annealing at 500 K.

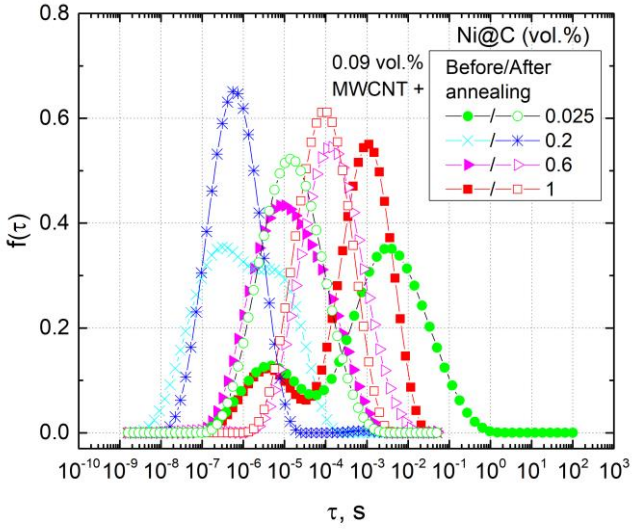

Figure 3.38: Relaxation time distributions (calculated according to Equation (1.23)) for epoxy/MWCNT/Ni@C hybrid composites at room temperature before and after annealing at 500 K.

3.2.3 Summary

The dielectric/electric properties of the epoxy/MWCNT/$MnFe_2O_4$ hybrid composites with two fixed MWCNTs amounts (below and above percolation threshold for the case of monofiller composite series) and varying $MnFe_2O_4$ concentrations up to 10 vol.% were investigated in the broad frequency (20 Hz-40 GHz) and temperature (20-500 K) regions. At low frequencies, the dielectric permittivity and the electrical conductivity of composites are strongly dependent on $MnFe_2O_4$ concentration. Moreover, for composites with MWCNT concentrations just below the percolation threshold, the electrical conductivity had a maximum close to 0.025 vol.% of manganese ferrite, which gave up to 10^3 larger conductivity than that of the composite without $MnFe_2O_4$. This indicates that a pronounced synergy effect between two types of particles occurs. In contrast, for composites with MWCNT concentrations above the percolation threshold (for the case of just the polymer comprising MWCNTs), the synergy effect was not observed with any $MnFe_2O_4$ content. The occurrence of synergy effects in the electrical properties of polymer composites is strongly related to the favorable distribution of nanoparticles inside the polymer matrix, which was suggested by the SEM investigations and calculations of the distribution of relaxation times.

Similar dielectric spectroscopy investigations were performed for epoxy/MWCNT/Ni@C hybrid composites with fixed MWCNTs amount (just below percolation threshold in corresponding monofiller composite series) and different Ni@C concentrations up to 1 vol.%. For this composite series, the electrical conductivity had a maximum close to 0.2 vol.% of Ni@C with absolute value several orders of magnitude higher than for sample with MWCNTs only. It means a pronounced synergy effect between two types of particles occurs at optimal Ni@C concentration.

The dielectric relaxation spectroscopy in polymer-based multiphase composites could be used as a non-invasive platform for the estimation of the nanoparticle distribution within the bulk of the polymer matrix. The latter is directly related to the synergy effect from the use of a few different nanoinclusions. To conclude, the analysis of the dielectric relaxation processes in multiphase composites at given fixed concentrations of the conductive functional filler and varying content of an additional one could help to optimize the relative amount of the second filler for achieving synergy.

3.3 Robust design of compact microwave absorbers and waveguide matched loads based on lossy materials

The development of effective absorbers of electromagnetic radiation is very important for many actual practical problems related to electromagnetic compatibility[53,58,210]. The waveguide matched load is a common example of a device, which absorbs electromagnetic energy almost without reflecting the incident electromagnetic wave. Usually, the design of such components is based on a long wedge or pyramid placed in the center of the waveguide[55]. The wedge is made of lossy material (e.g. dispersed carbonyl iron particles in the epoxy resin) and its top is oriented to the incident wave source. The existence of the optimal value of complex dielectric permittivity (or electrical conductivity in the range of "several Siemens per meter" for microwave frequencies) for effective absorption in the material was shown previously[149,211]. Nevertheless, in practice, it is often difficult to achieve optimal dielectric permittivity and control simultaneously both material losses and its mechanical properties. The losses in available conventional materials are often below optimal values leading to an increase in the length of the wedge to achieve the necessary level of electromagnetic attenuation.

The periodic pyramidal structures are used as broadband absorbers for the anechoic chambers[56,57]. Viskadourakis et al investigated the shielding efficiency of the lossless pyramidal structure in 3.5-7 GHz[58], Nornikman et al studied the hexagonal pyramids[59] in 1-20 GHz, Jenks[60] applied the pyramidal structures as the antenna for 3.3-8.0 GHz frequencies. However, all the mentioned components were produced from non-conductive polymers. The development of pyramidal structures based on lossy materials opens new possibilities in the field of electromagnetic interference (EMI) shielding applications. In particular, it allows to miniaturize microwave components, such as absorbers and loads.

The cheap and time-saving possibility to produce devices and structures of complex shape is additive manufacturing (3D-printing). It will be shown that DC-conductive filament of intermediate electrical conductivity (i.e. $\simeq 1$ S/m) is a universal mean for microwave attenuation elements design by 3D-printing.

This subchapter is devoted to study the advantages of the application of periodic pyramidal structures based on lossy materials as shielding components and matched loads design. The numerical method for electromagnetic properties simulations and optimal geometrical parameters evaluation will be presented. The effectiveness of the method will be verified

by experimental studying the shielding performances of the 3D-printed nanocarbon-based lossy pyramidal structures in 12-18 GHz (Ku-band) and 26-37 GHz (Ka-band) frequency ranges.

3.3.1 Homogenization procedure of pyramidal structures

The classical matched load working principle is based on a smooth transition from an empty waveguide to a waveguide filled with lossy material. The smooth transition is necessary to vanish the reflected power from inhomogeneity inside the waveguide. Usually, the lossy region is made in the shape of a long wedge or pyramid and placed in the center of the waveguide, which top oriented to the incident electromagnetic wave (Figure 3.39 (inset)). The coordinate of the base of the pyramid is assigned as (x=0), dh is the pyramid's height, h_0 is the substrate (base of the pyramid) thickness. By propagation through the waveguide from the top of the pyramid to the base, the relative volume fraction of the lossy material increases and vice-versa the air fraction decreases. Since the transition is smooth, homogenization can be done and the pyramid may be considered as a structure with spatially distributed refractive index[63,64]. In references[51,65] was demonstrated experimentally and numerically that the scattering parameters of the homogenized layer are equivalent to the initial structure for spheres, hollow spheres, corrugated composites and similar structures inside the waveguide.

The cross-section of a waveguide along the plane perpendicular to the pyramid base consists of the rectangle-like lossy region and air region. The homogenization procedure, in this case, means that the air regions can be averaged with lossy regions according to their relative surface fractions $S(x)$. The dependence of the effective refractive index n on the coordinate x is as follows[63,65]:

$$n(x) = n_p\big(1 - S(x)\big) + n_0 S(x) \tag{3.8}$$

where

$$S(x) = \begin{cases} 1, & x < -(h_0 + dh) \\ 1 - \left(\frac{h_0 + dh + x}{dh}\right)^2, & -(h_0 + dh) < x < -h_0 \\ 0, & -h_0 < x < 0 \\ 1, & x > 0 \end{cases} \tag{3.9}$$

and $n_p = \sqrt{\varepsilon}$ is the refractive index of the pyramid's bulk material, n_0=1 is the refractive index of air. The spatial distribution of refractive index $n(x)$ Equation (3.8) is parabolic and presented in Figure 3.39.

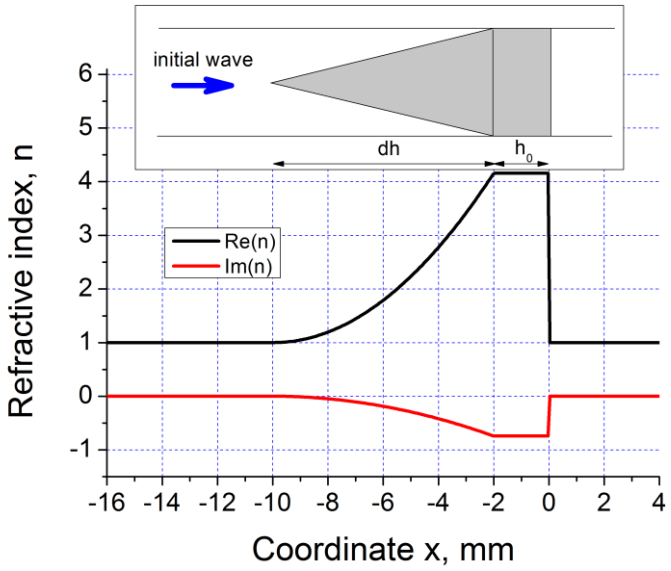

Figure 3.39: Spatial distribution of refractive index in the pyramidal structure after homogenization (inset: the side view of the pyramid inside the waveguide).

The relative amplitudes of reflected S_{11} and transmitted S_{21} trough the pyramid signals may be easily calculated using a multi-layered approach (see subchapter 1.2) developed in optics and discussed in detail in[51,62,65]. The shielding efficiency SE is defined[212,213] as $SE_T = -20log_{10}S_{21}$. Similarly, the efficiency due to reflectance is $SE_R = -20log_{10}S_{11}$.

The presented model gives the dependence of the shielding efficiency of pyramids placed in the waveguide transmission line on their geometrical parameters (h_0, dh) and dielectric properties (ε). Important to note, that in the case of an array of pyramids inside the waveguide or in the free space it is enough to consider and perform averaging and homogenization within one unit cell.

3.3.2 Sample preparation and characterization

Conductive filament production

The DC-conductive filament is based on the poly(lactic) acid (PLA) Ingeo^{TM} Biopolymer PLA-3D850 (Nature Works) with a 12 wt.%-content of -OH modified multiwalled carbon nanotubes (MWCNTs) supplied by

TimesNano, China. The following procedure was used to prepare this filament ready for further 3D-printing.

Firstly, the masterbatch of 12 wt % MWCNTs was prepared by melt mixing of the filler and the polymer in the twin-screw extruder (COLLIN Teach-Line ZK25T) by setting a screw speed of 40 rpm and keeping the temperature in the range 170-180 ^{o}C. After that, the composite pellets were extruded by a single screw extruder (Friend Machinery Co., Zhangjiagang, China) in the temperature range 170-180 ^{o}C and a screw speed of 10 rpm for producing filament for 3D printing (FDM) with 1.75 mm in diameter.

Filament properties and printing

Scanning electron microscopy analysis was performed to get information about the dispersion of nanofiller in the PLA host and its effect on the microstructure. Figure 3.40a,b showed the surfaces of both neat PLA and 12 wt% MWCNT/PLA, respectively, after liquid nitrogen breakage of the filament. Very different fracture surfaces are visible for the tested PLA and composite filaments, which are largely attributed to their brittle or ductile mechanical behavior. The neat PLA surfaces appear very flat due to the ductile fracture type, typical for an isotropic polymeric material. In contrast, a network-type structure is developed over the entire surface of the MWCNT/PLA composite, due to the interconnection of well-dispersed MWCNTs and to a fine structure of micro-voids that is typical for a more brittle material.

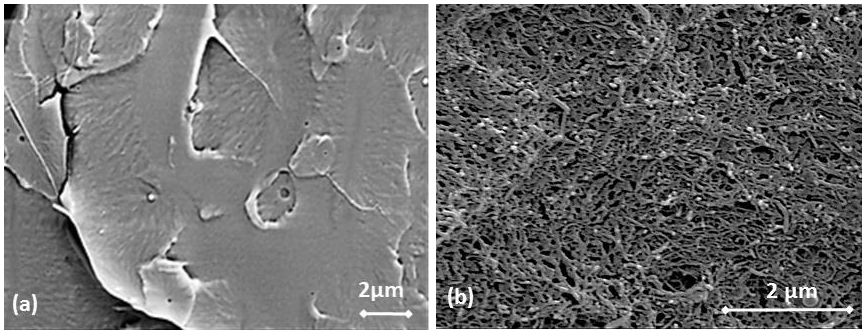

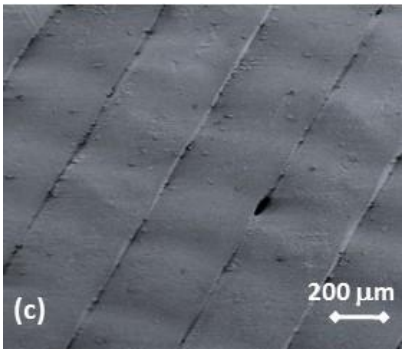

Figure 3.40: Scanning electron microscopy images: the cross-section of the PLA (a) and 12 wt.% MWCNT/PLA (b) filaments; (c) the surface of the 3D printed structure using 12 wt% MWCNT/PLA.

In general, the network filler–polymer microstructure, formed by the strong and conductive MWCNTs in the PLA matrix is typically associated with percolation, which may result in enhanced mechanical and physical properties of nanocomposites compared to the neat PLA. The details of mechanical properties, electrical and thermal conductivity and electromagnetic shielding efficiency of both neat PLA and 12 wt% MWCNT/PLA filaments, obtained from earlier studies[53,214,215] are summarized in Table 3.12. As seen, the addition of 12 wt% MWCNTs enhances significantly mechanical properties of the filament, e.g. tensile elastic modulus and hardness, but decrease twice the elongation at ultimate strength, compared to the neat PLA. Moreover, the composite filament demonstrates twice higher thermal conductivity, compared to the PLA. This confirms the microstructural prediction, that the percolation structure of 12 wt% MWCNTs in the nanocomposite filament is highly conductive, lossy and stronger, but more brittle, than the neat PLA.

The improvement of Young's modulus (21%), hardness (11%) and electrical conductivity (10 decades) could be associated with the dense, conductive network structure formed by the carbon nanotubes above the percolation threshold, which allows a transfer of the extraordinary mechanical and electrical properties of carbon nanotubes through the polymer. In contrast, a twice decrease of % elongation of the composite filament compared to the neat PLA may be attributed to the large surface area of the filler which absorbs most of the polymer at the interfaces, as shown in Figure 3.40b, which leads to increase of the brittleness of the composite material[53,215]. However, the thermal conductivity of 12 wt% MWCNT/PLA filament was observed only

twice higher compared to the neat PLA, in spite of the extremely high thermal conductivity of carbon nanotubes (3000 W/mK). This can be explained by the complex process of thermal diffusion through a polymer, influenced by temperature, crystallinity, macromolecular orientation, etc. Moreover, carbon nanotubes within polymers are usually considered to have many defects that contribute to numerous phonon scattering lowering the thermal conductivity[214].

The fused deposition modeling (FDM-FFF)-type 3D printer X400 PRO German RepRap with an extrusion nozzle with a diameter of 0.5 mm was used. During printing, the filament was heated above its melting temperature and then extruded using a PC-controlled moving nozzle[53]. Thus, the desired 3D-structure is formed as a result of a layered process. The processing parameters of the 3D printing were a temperature of 200 ºC, an extrusion speed of 100 mm/min, and a platform temperature of 60 ºC. Samples were printed with 100% infill, in a rectangular direction from one layer to another, as shown in Figure 3.40c.

Table 3.12: Mechanical and physical properties of the filaments.

Filament type	Tensile strength, MPa	Tensile young's modulus, MPa	Elongation, %	Hardness, MPa	Electrical conductivity, S/m	Thermal conductivity, W/mK
PLA	28.1±3.9	593.6±8.5	8.5±1.6	176±5	$8.3 \cdot 10^{-11}$	0.18±0.03
12 wt. MWCNT	23.3±1.9	719.9±6.2	4.3±0.4	195±9	0.39	0.37±0.02

3.3.3 Optimal pyramid parameters determination

The complex dielectric permittivity and refractive index of the used filament recalculated from experimentally measured S-parameters of the printed plane-parallel layer[216] are presented in Figure 3.41. The filament has a high loss tangent (not less than 0.4 within the whole frequency range). Moreover, the material is dispersive, its dielectric permittivity is generally decreasing with frequency. This type of dispersion is typical for nanocarbon composites with filler content above the percolation threshold in the microwave frequency range[150,209].

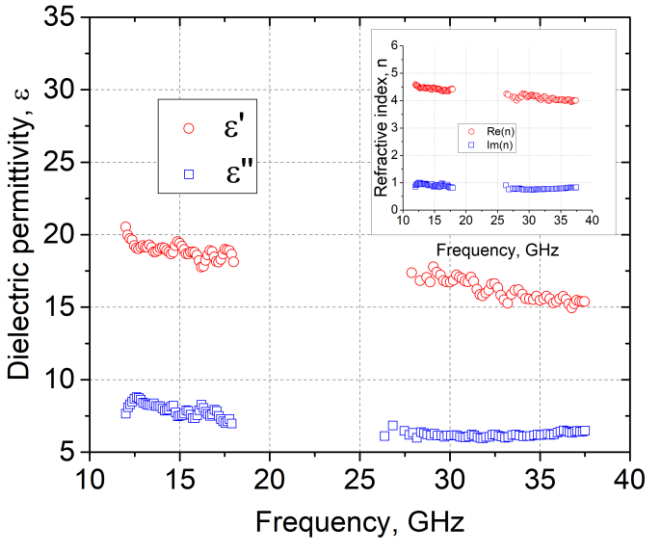

Figure 3.41: Frequency dependencies of dielectric permittivity and refractive index (inset) of the printed material in Ku-and Ka-bands.

The minimal height of pyramids and the substrate thickness were computed using proposed model Equations (3.8)-(3.9). Several simplifications were made. The frequency was fixed as 30 GHz, the effective shielding criteria were introduced as SE_T>20 dB and SE_R>20 dB (this is equivalent to the absorption of more than 99% of the power of incident wave).

For the computations of dh, substrate height was taken as h_0=2 mm. In this case, SE of the pyramid is dependent only on its height and dielectric permittivity of used material. The combinations of dh and ε that satisfy the mentioned criteria for SE are presented as the regions in $\varepsilon''(\varepsilon')$ coordinates in Figure 3.42. The decrease of the dh result in narrowing the region of possible ε combinations. The measured dielectric permittivity of the filament at 30 GHz is ε=16.74−i6.17 (Figure 3.41). The minimal pyramid's height dh, required for the effective shielding is 8–9 mm for the Ka-band. Similarly, dh=22 mm was evaluated for the Ku-band.

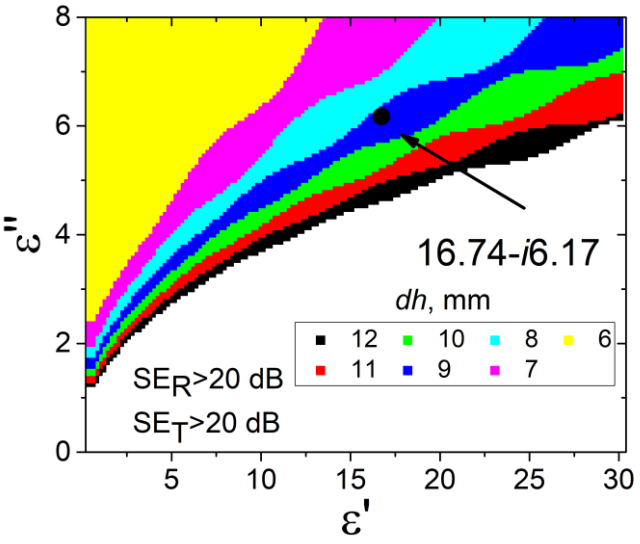

Figure 3.42: The pyramid height dh, required for the effective (20 dB) EMI shielding, presented as the dependence on the dielectric permittivity. Dot stands for the measured ε of used filament at frequency 30 GHz.

For substrate thickness h_0 computations the obtained dh=8 mm was used. The dependencies SE_T and SE_R on the substrate thickness h_0 are presented in Figure 3.43 (filled symbols). The oscillations of SE_R related to the interference, while SE_T increases monotonously. These oscillations may be significantly dumped by increasing the height of the pyramids dh. The SE vs h_0 for the plane-parallel layer (dh=0 mm) are also presented in Figure 3.43 (see open symbols). Both SE_R and SE_T of the plane layer are significantly lower in comparison with the pyramidal structure. The SE_T expectedly increases with the thickness, but the SE_R remains lower than 5 dB. It means that a planar layer cannot simultaneously demonstrate high SE_R and SE_T parameters (or in other words absorption ability) at any substrate thickness.

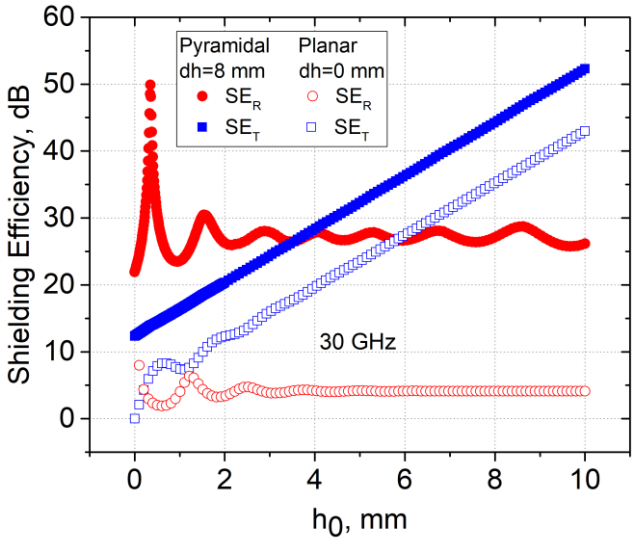

Figure 3.43: The dependence of the SE_T and SE_R on the substrate thickness. Pyramid heights are dh=8 mm (close symbols) and dh=0 mm (open symbols).

The proposed graded index approach is useful for the practical design of pyramidal matched loads. It provides the minimal geometrical parameters required for the effective SE taking into account the dielectric properties of used material. In the particular case of the filament's permittivity, the combinations of h_0=2 mm, dh=8–9 mm (Ka-band) and dh=22 mm (Ku-band) are the minimal parameters, which allow to meet 20 dB level for both SE_T and SE_R.

3.3.4 Microwave measurements

The printed pyramidal samples and the experimentally measured in Ku- and Ka-bands shielding efficiency are presented in Figures 3.44 and 3.45, correspondingly.

Both structures for Ku- and Ka-bands demonstrate a high level of SE_T>20 dB and SE_R>20 dB, even despite some printing issues (see Figure 3.44), and may be used as effective matched loads or absorbers in anechoic chambers. Usage of lossy material with high ε' and ε'' allows to obtain similar shielding performance with smaller pyramids (see Table 3.13).

Even more, in contrast to the results listed in Table 3.13[59,217–221], Figure 3.45 demonstrates that both transmitted and reflected signals are well attenuated. It is possible due to the combination of high Ohmic losses within the material bulk and waves scattering due to the sample's geometry. Important to note, that high Ohmic losses in considered materials were achieved because of forming DC conductive MWCNT-based network within the polymer matrix. Due to depolarization effects[209] the MWCNT agglomerates in the composite below percolation weakly interact with microwave radiation. Nevertheless, when agglomerates are incorporated in the percolative network of DC-conductive composite (which is exactly corresponds to our experimental situation) they contribute to effective scattering and attenuation of the electromagnetic waves.

Table 3.13: Comparison of the shielding performances of the pyramidal structures.

Material parameters	dh, mm	h_0, mm	SE_R, dB	SE_T, dB	Frequency, GHz	Reference
ε=2, tanδ=0.2	90	25	45	n/a	10	[217]
ε=2.492, tanδ=0.956	130	20	42.93	n/a	10-15	[59]*hexagonal
ε=2.9, tanδ=0.084	130	n/a	43.294	n/a	10-15	[218]*triangonal
BlackMagic 3D	2	2	12	n/a	5.5	[219]
VeroBlack	80	20	20	n/a	100	[220]
ε=1.5, tanδ=0.26	40	20	40	n/a	30	[221]
ε=18.66, tanδ=0.38	22	2	40.15	28.09	17.4	this research
ε=15.55, tanδ=0.39	8	2	23.88	39.17	35.7	this research

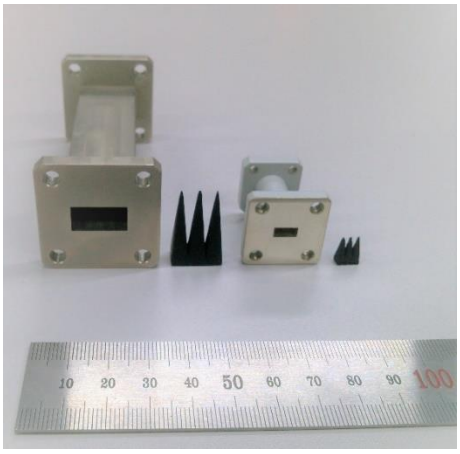

Figure 3.44: 3D printed pyramidal structures and waveguide systems for Ku-band on the left and for Ka-band on the right.

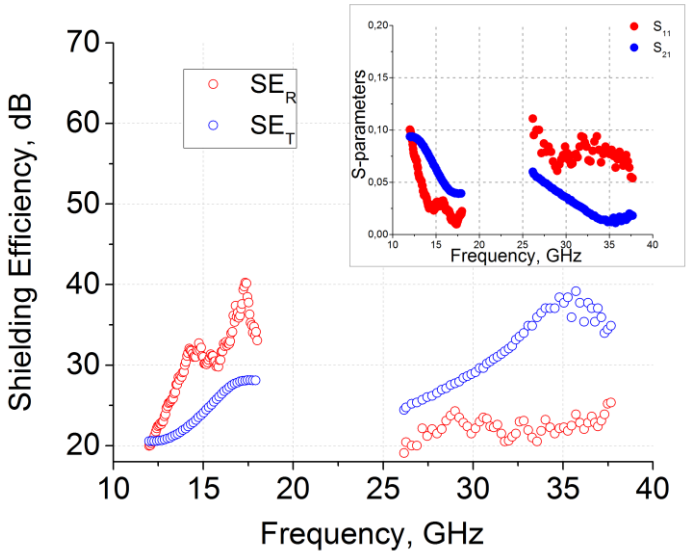

Figure 3.45: Shielding efficiency and S-parameters (inset) of the 3D printed pyramidal samples in Ku- and Ka-bands.

3.3.5 Microwave electromagnetic response predictions

According to the model introduced and successfully applied above, taking into account the material bulk properties (dielectric permittivity or refractive index in general case), the required frequency range and the substrate thickness, it is possible to evaluate the shielding efficiency of pyramidal structures at the pre-experimental step.

Among the epoxy-based composites with magnetic nanoparticles studied in subchapters 3.1-3.2, for the Ni@C system the complex dielectric permittivity remains quite high even in the microwave frequency range. It means these composites are suitable for electromagnetic shielding applications due to the high dielectric/magnetic losses. This fact is proved by the data of the shielding efficiency for a 2 mm-thick Ni@C composite plane-parallel layer presented in Table 3.7 (subchapter 3.1.3). However, these results are still far from perfect ones. By constructing pyramidal structures based on Ni@C composites, the absorption ability can be significantly improved, and the optimization model can help to predict these properties.

Table 3.14 shows absorption ability predictions of the pyramidal structures made from Ni@C composite with a substrate thickness of h_0=2 mm and different pyramid heights dh (from 8 to 15 mm) in waveguide at 30 GHz.

Table 3.14: Absorbance (%) ability predictions of the pyramidal structures made from Ni@C composite with a substrate thickness of h_0=2 mm and different pyramid heights dh in the waveguide at 30 GHz.

Sample	dh, mm								
	0	8	9	10	11	12	13	14	15
15 vol.% Ni@C	29.0	71.9	74.9	77.1	78.8	80.6	82.4	84.1	85.5
25 vol.% Ni@C	44.0	89.6	90.7	92.1	93.6	94.6	95.3	95.9	96.5
30 vol.% Ni@C	62.0	95.6	96.0	96.5	97.5	98.0	98.3	98.6	99.0

First of all, the pyramidal shape of the structure (with any dh in Table 3.14) contributes to a significant increase of absorption coefficient in comparison with the Ni@C composites plane-parallel layer (the first column of Table 3.14 with dh=0 mm corresponds to the data from the Table 3.7). At minimum pyramid height dh=8 mm, the absorption coefficient is lower than for the case of 12 wt.% MWCNT/PLA (99%), but it is still quite high and amounts to 95.6% for a sample with 30 vol.% of Ni@C. With an increase of dh, the coefficient obviously increases and at the dh=15 mm it reaches 99% for 30 vol.% of Ni@C. Thus, pyramid-shaped Ni@C / epoxy composites can also be used as an effective absorber and matched load in the microwave frequency range.

3.3.6 Summary

The pyramidal periodic structure based on conductive lossy material as effective microwave absorber and compact matched load was considered. The 3D printed pyramidal structures were experimentally tested in Ku- and Ka-bands. The pyramid height and the substrate thickness were obtained through the optimization of the shielding efficiency versus the material complex permittivity. The measured shielding efficiency of the printed samples is higher than 20 dB both for reflected and transmitted signals in the investigated frequency ranges. The developed technique for the pyramid parameters evaluation may be effectively used as a pre-experimental step since it takes into account the material properties (both for lossy and lossless), required frequency range, and substrate thickness.

CONCLUSIONS

This thesis is focused on the experimental investigations of dielectric properties of several epoxy-based composites systems: (i) binary with three different types of magnetic nanoparticles ($Fe_2O_3 \cdot H_2O$, $MnFe_2O_4$, Ni@C) and (ii) ternary hybrid with a combination of magnetic nanoparticles and multiwalled carbon nanotubes. Besides, the robust design of compact microwave absorbers and waveguide matched loads based on a conductive lossy composite demonstrates.

The main conclusions of the thesis are following:

1. The dielectric properties of $Fe_2O_3 \cdot H_2O$ nanorods / epoxy resin composites have been studied in a wide frequency range from hertz to terahertz at temperatures of 200-450 K. The percolation threshold in this system is about 40 vol.%.
2. The dielectric properties of $MnFe_2O_4$ / epoxy resin composites with two different sizes of spherical-shaped particles (28 and 60 nm) have been studied in the frequency range from 20 Hz to 1 MHz and temperature range of 150-500 K. It was demonstrated that the percolation thresholds in these composites are 30 and 29.3 vol.% for small and large $MnFe_2O_4$ nanoparticles, respectively. The minor difference in the percolation threshold value is related to the better distribution of larger nanoparticles.
3. The following several common features for $Fe_2O_3 \cdot H_2O$ / epoxy and $MnFe_2O_4$ / epoxy systems are observed:
    - The dielectric behavior of composites below the percolation threshold is mainly determined by relaxation in a pure polymer matrix. The dielectric properties of composites above the percolation threshold are determined by the percolation network, which is formed by the filler particles inside the composite.
    - At low frequencies, the DC conductivity is observed due to the random distribution of electric charge carriers and increases with the filler concentration. At high temperatures, because of the finite conductivity of the epoxy resin, the DC electrical conductivity occurs in the composites both above and below the percolation threshold. The activation energy decreases with fillers concentration indicating that the electrical transport occurs together in fillers and epoxy matrix subsystems.

4. The dielectric/electric properties of the Ni@C / epoxy resin composites have been studied in broad frequency (20 Hz-40 GHz) and temperature (30–500 K) ranges. For such a system, it was possible to roughly estimate the percolation threshold, which is in the range between 10 and 15 vol.%. Additional annealing of these composites up to 500 K substantially decreases the percolation threshold down to below 10 vol.%. However, with a Ni@C concentration increase, the nanoparticles dispersion quality in the polymer is suppressed dramatically. This is proved by the SEM micrographs and the analysis of relaxation time distributions.
5. For Ni@C / epoxy resin composites, the concentration increase leads to substantial attenuation of electromagnetic radiation of microwave frequency range, and the 2 mm-thick sample of maximum concentration (30 vol.% Ni@C) transmits only 17% of the incident wave.
6. Ternary epoxy/MWCNT/$MnFe_2O_4$ and epoxy/MWCNT/Ni@C hybrid composites systems demonstrate a pronounced synergy effects at MWCNT concentrations just below the percolation threshold (in corresponding monofiller composite series) and certain small amounts of the second magnetic filler. For epoxy/MWCNT/$MnFe_2O_4$ composites, the electrical conductivity has a maximum close to 0.025 vol.% of manganese ferrite, which gave up to 10^3 larger conductivity than that of the composite without $MnFe_2O_4$. For epoxy/MWCNT/Ni@C the electrical conductivity has a maximum close to 0.2 vol.% of Ni@C with absolute value several orders of magnitude higher than for sample with MWCNTs only.
7. For composites with MWCNT concentrations above the percolation threshold (for the case of just the polymer comprising MWCNTs), the synergy effect was not observed with any $MnFe_2O_4$ content.
8. The occurrence of synergy effects in the electrical properties of polymer composites is strongly related to the favorable distribution of nanoparticles inside the polymer matrix. The dielectric relaxation spectroscopy processes in multiphase composites at given fixed concentrations of the conductive functional filler and varying content of an additional one could help to optimize the relative amount of the second filler for achieving synergy.
9. The pyramidal periodic structure based on conductive lossy material as effective microwave absorber and compact matched load was considered. The pyramid geometry parameters were obtained through the optimization of the shielding efficiency versus the material complex permittivity. The 3D printed pyramidal structures with estimated parameters were experimentally tested in microwave frequency ranges,

and they demonstrated electromagnetic attenuation higher than 20 dB both for reflected and transmitted signals. The developed technique for the pyramid parameters evaluation may be effectively used as a pre-experimental step since it takes into account the material properties (both for lossy and lossless), required frequency range, and the pyramid sizes.

REFERENCES

1. Komarneni S. Feature article. Nanocomposites. *J Mater Chem*. 1992;2:1219-1230.

2. Ajayan PM, Schadler LS, Braun PV. *Nanocomposite Science and Technology*. Wiley-VCH; 2003.

3. Fu S-Y, Feng X-Q, Lauke B, Mai Y-W. Effects of particle size, particle/matrix interface adhesion and particle loading on mechanical properties of particulate–polymer composites. *Compos Part B Eng*. 2008;39(6):933-961. doi:10.1016/j.compositesb.2008.01.002

4. Bhattacharya M, Bhowmick AK. Polymer–filler interaction in nanocomposites: New interface area function to investigate swelling behavior and Young's modulus. *Polymer*. 2008;49(22):4808-4818.

5. Rahmat M, Hubert P. Carbon nanotube–polymer interactions in nanocomposites: A review. *Compos Sci Technol*. 2011;72(1):72-84.

6. Crosby AJ, Lee J. Polymer Nanocomposites: The "Nano" Effect on Mechanical Properties. *Polym Rev*. 2007;47(2):217-229.

7. Rahman A, Ali I, Al Zahrani SM, Eleithy RH. A REVIEW OF THE APPLICATIONS OF NANOCARBON POLYMER COMPOSITES. *Nano*. 2011;06(03):185-203. doi:10.1142/S179329201100255X

8. Zhang W, Dehghani-Sanij AA, Blackburn RS. Carbon based conductive polymer composites. *J Mater Sci*. 2007;42(10):3408-3418. doi:10.1007/s10853-007-1688-5

9. Li B, Zhong W-H. Review on polymer/graphite nanoplatelet nanocomposites. *J Mater Sci*. 2011;46:5595-5614.

10. Ma P-C, Siddiqui NA, Marom G, Kim J-K. Dispersion and functionalization of carbon nanotubes for polymer-based nanocomposites: A review. *Compos Part Appl Sci Manuf*. 2010;41(10):1345-1367.

11. Macutkevic J, Kuzhir P, Paddubskaya A, et al. Epoxy Resin/Carbon Black Composites Below the Percolation Threshold. *J Nanosci Nanotechnol*. 2013;13(8):5434-5439. doi:10.1166/jnn.2013.7547

12. Macutkevic J, Seliuta D, Valušis G, et al. High dielectric permittivity of percolative composites based on onion-like carbon. *Appl Phys Lett*. 2009;95(11):112901. doi:10.1063/1.3224187

13. Deng H, Skipa T, Bilotti E, et al. Preparation of High-Performance Conductive Polymer Fibers through Morphological Control of Networks Formed by Nanofillers. *Adv Funct Mater*. 2010;20(9):1424-1432. doi:10.1002/adfm.200902207

14. Inzelt G. *Conducting Polymers: A New Era in Electrochemistry*. Springer; 2008.

15. Vinoy KJ. *Radar Absorbing Materials: From Theory to Design and Characterization.* Springer; 2012.

16. Ramasubramaniam R, Chen J, Liu H. Homogeneous carbon nanotube/polymer composites for electrical applications. *Appl Phys Lett*. 2003;83(14):2928-2930. doi:10.1063/1.1616976

17. Essone Mezeme M, Bouazzaoui SE, Achour ME, Brosseau C. Uncovering the intrinsic permittivity of the carbonaceous phase in carbon black filled polymers from broadband dielectric relaxation. 2011;109(7):074107.

18. Bellucci S, Balasubramanian C, De Bellis G, Micciulla F, Rinaldi G. Screening Electromagnetic Interference Effect using Nanocomposites. *Macromol Symp*. 2008;263(1):21-29. doi:10.1002/masy.200850303

19. Qin F, Brosseau C. A review and analysis of microwave absorption in polymer composites filled with carbonaceous particles. *J Appl Phys*. 2012;111(6):061301. doi:10.1063/1.3688435

20. Ahmed SR, Ogale SB, Papaefthymiou GC, Ramesh R, Kofinas P. Magnetic properties of CoFe2O4 nanoparticles synthesized through a block copolymer nanoreactor route. *Appl Phys Lett*. 2002;80(9):1616-1618. doi:10.1063/1.1456258

21. Arulmurugan R, Vaidyanathan G, Sendhilnathan S, Jeyadevan B. Mn–Zn ferrite nanoparticles for ferrofluid preparation: Study on thermal–magnetic properties. *J Magn Magn Mater*. 2006;298(2):83-94. doi:10.1016/j.jmmm.2005.03.002

22. Peng E, Choo ESG, Chandrasekharan P, et al. Synthesis of Manganese Ferrite/Graphene Oxide Nanocomposites for Biomedical Applications. *Small*. 2012;8(23):3620-3630. doi:10.1002/smll.201201427

23. Temizel E, Ayan E, Şenel M, et al. Synthesis, conductivity and magnetic properties of poly(N-pyrrole phosphonic acid)–Fe3O4 nanocomposite. *Mater Chem Phys*. 2011;131(1-2):284-291. doi:10.1016/j.matchemphys.2011.09.043

24. Feng YB, Qiu T, Shen CY. Absorbing properties and structural design of microwave absorbers based on carbonyl iron and barium ferrite. *J Magn Magn Mater*. 2007;318(1-2):8-13. doi:10.1016/j.jmmm.2007.04.012

25. Yong-Jin Kim, Sung-Soo Kim. Microwave absorbing properties of Co-substituted Ni/sub 2/W hexaferrites in Ka-band frequencies (26.5-40 GHz). *IEEE Trans Magn*. 2002;38(5):3108-3110. doi:10.1109/TMAG.2002.802483

26. Jin F, Tong H, Li J, Shen L, Chu PK. Structure and microwave-absorbing properties of Fe-particle containing alumina prepared by micro-arc discharge oxidation. *Surf Coat Technol*. 2006;201(1-2):292-295. doi:10.1016/j.surfcoat.2005.11.116

27. Zhao B, Deng J, Zhang R, et al. Recent Advances on the Electromagnetic Wave Absorption Properties of Ni Based Materials. *Eng Sci*. Published online 2018. doi:10.30919/es8d735

28. Zhang XF, Dong XL, Huang H, et al. Microwave absorption properties of the carbon-coated nickel nanocapsules. *Appl Phys Lett*. 2006;89(5):053115. doi:10.1063/1.2236965

29. Li J, Ma PC, Chow WS, To CK, Tang BZ, Kim J-K. Correlations between Percolation Threshold, Dispersion State, and Aspect Ratio of Carbon Nanotubes. *Adv Funct Mater*. 2007;17(16):3207-3215. doi:10.1002/adfm.200700065

30. Yao S-H, Dang Z-M, Jiang M-J, Xu H-P, Bai J. Influence of aspect ratio of carbon nanotube on percolation threshold in ferroelectric polymer nanocomposite. *Appl Phys Lett*. 2007;91(21):212901. doi:10.1063/1.2817746

31. Shehzad K, Dang Z-M, Ahmad MN, et al. Effects of carbon nanotubes aspect ratio on the qualitative and quantitative aspects of frequency response of electrical conductivity and dielectric permittivity in the carbon nanotube/polymer composites. *Carbon*. 2013;54:105-112. doi:10.1016/j.carbon.2012.10.068

32. Bauhofer W, Kovacs JZ. A review and analysis of electrical percolation in carbon nanotube polymer composites. *Compos Sci Technol*. 2009;69(10):1486-1498. doi:10.1016/j.compscitech.2008.06.018

33. Spitalsky Z, Tasis D, Papagelis K, Galiotis C. Carbon nanotube–polymer composites: Chemistry, processing, mechanical and electrical properties. *Prog Polym Sci*. 2010;35(3):357-401. doi:10.1016/j.progpolymsci.2009.09.003

34. Hu H, Zhao L, Liu J, et al. Enhanced dispersion of carbon nanotube in silicone rubber assisted by graphene. *Polymer*. 2012;53(15):3378-3385. doi:10.1016/j.polymer.2012.05.039

35. Yang S-Y, Lin W-N, Huang Y-L, et al. Synergetic effects of graphene platelets and carbon nanotubes on the mechanical and thermal properties of epoxy composites. *Carbon*. 2011;49(3):793-803. doi:10.1016/j.carbon.2010.10.014

36. Im H, Kim J. Thermal conductivity of a graphene oxide–carbon nanotube hybrid/epoxy composite. *Carbon*. 2012;50(15):5429-5440. doi:10.1016/j.carbon.2012.07.029

37. Chen J, Du X-C, Zhang W-B, et al. Synergistic effect of carbon nanotubes and carbon black on electrical conductivity of PA6/ABS blend. *Compos Sci Technol*. 2013;81:1-8. doi:10.1016/j.compscitech.2013.03.014

38. Thongruang W, Spontak RJ, Balik CM. Correlated electrical conductivity and mechanical property analysis of high-density polyethylene filled with graphite and carbon fiber. *Polymer*. 2002;43(8):2279-2286. doi:10.1016/S0032-3861(02)00043-5

39. Sumfleth J, Adroher XC, Schulte K. Synergistic effects in network formation and electrical properties of hybrid epoxy nanocomposites containing multi-wall carbon nanotubes and carbon black. *J Mater Sci*. 2009;44(12):3241-3247. doi:10.1007/s10853-009-3434-7

40. Kranauskaite I, Macutkevic J, Banys J, et al. Synergy effects in the electrical conductivity behavior of onion-like carbon and multiwalled carbon nanotubes composites: Electrical conductivity behavior of OLC/CNT composites. *Phys Status Solidi B*. 2015;252(8):1799-1803. doi:10.1002/pssb.201451745

41. Shuba MV, Yuko DI, Gorokhov G, et al. Frequency and density dependencies of the electromagnetic parameters of carbon nanotube and graphene nanoplatelet based composites in the microwave and terahertz

ranges. *Mater Res Express*. 2019;6(9):095050. doi:10.1088/2053-1591/ab2edf

42. Kazakova MA, Korovin EYu, Moseenkov SI, et al. Electromagnetic Parameters of Composite Materials Based on Polyethylene and Multi-Walled Carbon Nanotubes Modified by Iron Oxide Nanoparticles. *Russ J Appl Chem*. 2018;91(12):1994-2002. doi:10.1134/S107042721812011X

43. Kazakova MA, Moseenkov SI, Golubtsov GV, et al. Structural and electromagnetic properties of Fe2Co-multi-walled carbon nanotubes-polystyrene based composite. *J Alloys Compd*. 2020;844:156107. doi:10.1016/j.jallcom.2020.156107

44. Wen F, Zhang F, Liu Z. Investigation on Microwave Absorption Properties for Multiwalled Carbon Nanotubes/Fe/Co/Ni Nanopowders as Lightweight Absorbers. *J Phys Chem C*. 2011;115(29):14025-14030. doi:10.1021/jp202078p

45. Lin H, Zhu H, Guo H, Yu L. Investigation of the microwave-absorbing properties of Fe-filled carbon nanotubes. *Mater Lett*. 2007;61(16):3547-3550. doi:10.1016/j.matlet.2007.01.077

46. Che RC, Peng L-M, Duan XF, Chen Q, Liang XL. Microwave Absorption Enhancement and Complex Permittivity and Permeability of Fe Encapsulated within Carbon Nanotubes. *Adv Mater*. 2004;16(5):401-405. doi:10.1002/adma.200306460

47. Wen B, Wang X, Zhang Y. Ultrathin and anisotropic polyvinyl butyral/Ni-graphite/short-cut carbon fibre film with high electromagnetic shielding performance. *Compos Sci Technol*. 2019;169:127-134. doi:10.1016/j.compscitech.2018.11.013

48. Liu L, Grunlan JC. Clay Assisted Dispersion of Carbon Nanotubes in Conductive Epoxy Nanocomposites. *Adv Funct Mater*. 2007;17(14):2343-2348. doi:10.1002/adfm.200600785

49. Levchenko V, Mamunya Ye, Boiteux G, et al. Influence of organo-clay on electrical and mechanical properties of PP/MWCNT/OC nanocomposites. *Eur Polym J*. 2011;47(7):1351-1360. doi:10.1016/j.eurpolymj.2011.03.012

50. Bychanok D, Liubimau A, Piasotski K, et al. Effective Carbon Nanotube/Phenol Formaldehyde Resin Based Double-Layer Absorbers of Microwave Radiation: Design and Modeling. *Phys Status Solidi B*. 2018;255(1):1700224. doi:10.1002/pssb.201700224

51. Bychanok DS, Plyushch AO, Gorokhov GV, Bychanok US, Kuzhir PP, Maksimenko SA. Microwave radiation absorbers based on corrugated composites with carbon fibers. *Tech Phys*. 2016;61(12):1880-1884. doi:10.1134/S1063784216120094

52. Tofail SAM, Koumoulos EP, Bandyopadhyay A, Bose S, O'Donoghue L, Charitidis C. Additive manufacturing: scientific and technological challenges, market uptake and opportunities. *Mater Today*. 2018;21(1):22-37. doi:10.1016/j.mattod.2017.07.001

53. Spinelli G, Lamberti P, Tucci V, et al. Nanocarbon/Poly(Lactic) Acid for 3D Printing: Effect of Fillers Content on Electromagnetic and Thermal Properties. *Materials*. 2019;12(15):2369. doi:10.3390/ma12152369

54. Wang X, Jiang M, Zhou Z, Gou J, Hui D. 3D printing of polymer matrix composites: A review and prospective. *Compos Part B Eng*. 2017;110:442-458. doi:10.1016/j.compositesb.2016.11.034

55. Pozar DM. *Microwave Engineering*. 4th ed. Wiley; 2012.

56. Chung B-K, Chuah H-T. Modeling of RF Absorber for Application in the Design of Anechoic Chamber. *Prog Electromagn Res*. 2003;43:273-285. doi:10.2528/PIER03052601

57. Hindman GE, Newell AC. Reflection suppression to improve anechoic chamber performance. *AMTA Eur*. Published online 2006:297-302.

58. Viskadourakis Z, Vasilopoulos KC, Economou EN, Soukoulis CM, Kenanakis G. Electromagnetic shielding effectiveness of 3D printed polymer composites. *Appl Phys A*. 2017;123(12):736. doi:10.1007/s00339-017-1353-z

59. Nornikman H, Malek F, Soh PJ, Azremi AAH. Reflection loss performance of hexagonal base pyramid microwave absorber using different agricultural waste material. In: *2010 Loughborough Antennas & Propagation Conference*. IEEE; 2010:313-316. doi:10.1109/LAPC.2010.5666029

60. Jenks CHJ. Dielectric pyramid antenna for GPR applications. In: *2016 10th European Conference on Antennas and Propagation (EuCAP)*. IEEE; 2016:1-3. doi:10.1109/EuCAP.2016.7481679

61. Born M, Wolf E. *Principles of Optics: Electromagnetic Theory of Propagation, Interference and Diffraction of Light*. 6th ed. Pergamon Press; 1980.

62. Macleod HA. *Thin-Film Optical Filters*. 4th ed. CRC Press/Taylor & Francis; 2010.

63. Stavenga DG, Foletti S, Palasantzas G, Arikawa K. Light on the moth-eye corneal nipple array of butterflies. *Proc R Soc B Biol Sci*. 2006;273(1587):661-667. doi:10.1098/rspb.2005.3369

64. Sun C-H, Jiang P, Jiang B. Broadband moth-eye antireflection coatings on silicon. *Appl Phys Lett*. 2008;92(6):061112. doi:10.1063/1.2870080

65. Bychanok D, Li S, Sanchez-Sanchez A, et al. Hollow carbon spheres in microwaves: Bio inspired absorbing coating. *Appl Phys Lett*. 2016;108(1):013701. doi:10.1063/1.4938537

66. Stauffer D, Aharony A. *Introduction To Percolation Theory Revised Second Edition*. Taylor and Francis; 2014.

67. Sahimi M. *Applications of Percolation Theory*. Taylor & Francis e-Library; 2009.

68. Nan C-W. Physics of inhomogeneous inorganic materials. *Prog Mater Sci*. 1993;37(1):1-116. doi:10.1016/0079-6425(93)90004-5

69. Nan C-W, Shen Y, Ma J. Physical Properties of Composites Near Percolation. *Annu Rev Mater Res*. 2010;40(1):131-151. doi:10.1146/annurev-matsci-070909-104529

70. Ahmad K, Pan W, Shi S-L. Electrical conductivity and dielectric properties of multiwalled carbon nanotube and alumina composites. *Appl Phys Lett*. 2006;89(13):133122. doi:10.1063/1.2357920

71. Efros AL, Shklovskii BI. Critical Behaviour of Conductivity and Dielectric Constant near the Metal-Non-Metal Transition Threshold. *Phys Status Solidi B*. 1976;76(2):475-485. doi:10.1002/pssb.2220760205

72. van der Putten D, Moonen JT, Brom HB, Brokken-Zijp JCM, Michels MAJ. Evidence for superlocalization on a fractal network in conductive carbon-black–polymer composites. *Phys Rev Lett*. 1992;69(3):494-497. doi:10.1103/PhysRevLett.69.494

73. Mott NF, Davis EA. Conduction in non-crystalline systems: II. The metal-insulator transition in a random array of centres. *Philos Mag*. 1968;17(150):1269-1284. doi:10.1080/14786436808223201

74. Castner TG, Lee NK, Cieloszyk GS, Salinger GL. Dielectric Anomaly and the Metal-Insulator Transition in n -Type Silicon. *Phys Rev Lett*. 1975;34(26):1627-1630. doi:10.1103/PhysRevLett.34.1627

75. Pecharromán C, Moya JS. Experimental Evidence of a Giant Capacitance in Insulator–Conductor Composites at the Percolation Threshold. *Adv Mater*. 2000;12(4):294-297. doi:10.1002/(SICI)1521-4095(200002)12:4<294::AID-ADMA294>3.0.CO;2-D

76. Grannan DM, Garland JC, Tanner DB. Critical Behavior of the Dielectric Constant of a Random Composite near the Percolation Threshold. *Phys Rev Lett*. 1981;46(5):375-378. doi:10.1103/PhysRevLett.46.375

77. Wagner KW. Erklärung der dielektrischen nachwirkungsvorgänge auf grund maxwellscher vorstellungen. *Arch Für Elektrotechnik*. 1914;2(9):371-387.

78. Sillars RW. The properties of a dielectric containing semiconducting particles of various shapes. *J Inst Electr Eng*. 1937;80(484):378-394. doi:10.1049/jiee-1.1937.0058

79. Prodromakis T, Papavassiliou C. Engineering the Maxwell–Wagner polarization effect. *Appl Surf Sci*. 2009;255(15):6989-6994. doi:10.1016/j.apsusc.2009.03.030

80. Kittel C. *Introduction to Solid State Physics*. 8th ed. Wiley; 2005.

81. Macedo P, Moynihan C, Bose R. Dielectric modulus: experiment, application, and interpretation. *J Phy Chem Glas*. 1972;13.

82. Liu J, Duan C-G, Yin W-G, Mei WN, Smith RW, Hardy JR. Large dielectric constant and Maxwell-Wagner relaxation in Bi 2 ⁄ 3 Cu 3 Ti 4 O 12. *Phys Rev B*. 2004;70(14):144106. doi:10.1103/PhysRevB.70.144106

83. Macutkevic J, Banys J, Matulis A. Determination of the Distribution of the Relaxation Times from Dielectric Spectra. *Nonlinear Anal Model Control*. 2004;9(1):75-88. doi:10.15388/NA.2004.9.1.15172

84. Macutkevic J, Banys J, Bussmann-Holder A, Bishop AR. Origin of polar nanoregions in relaxor ferroelectrics: Nonlinearity, discrete breather formation, and charge transfer. *Phys Rev B*. 2011;83(18):184301. doi:10.1103/PhysRevB.83.184301

85. Prochorov AM, ed. *Fizičeskaja ėnciklopedija*. Sovetskaja Ėnciklopedija; 1988.

86. Szeluga U, Kumanek B, Trzebicka B. Synergy in hybrid polymer/nanocarbon composites. A review. *Compos Part Appl Sci Manuf*. 2015;73:204-231. doi:10.1016/j.compositesa.2015.02.021

87. Thwe MM, Liao K. Durability of bamboo-glass fiber reinforced polymer matrix hybrid composites. *Compos Sci Technol*. 2003;63(3-4):375-387. doi:10.1016/S0266-3538(02)00225-7

88. Fu S-Y, Xu G, Mai Y-W. On the elastic modulus of hybrid particle/short-fiber/polymer composites. *Compos Part B Eng*. 2002;33(4):291-299. doi:10.1016/S1359-8368(02)00013-6

89. Wypych G. *Handbook of Fillers*. 4th edition. CP, ChemTec Publishing; 2016.

90. Ke K, Yue L, Shao H, Yang M-B, Yang W, Manas-Zloczower I. Boosting electrical and piezoresistive properties of polymer nanocomposites via hybrid carbon fillers: A review. *Carbon*. 2021;173:1020-1040. doi:10.1016/j.carbon.2020.11.070

91. Chatterjee S, Nafezarefi F, Tai NH, Schlagenhauf L, Nüesch FA, Chu BTT. Size and synergy effects of nanofiller hybrids including graphene nanoplatelets and carbon nanotubes in mechanical properties of epoxy composites. *Carbon*. 2012;50(15):5380-5386. doi:10.1016/j.carbon.2012.07.021

92. You J, Cao J-Y-Q, Chen S-C, Wang Y-Z. Preparation of polymer nanocomposites with enhanced mechanical properties using hybrid of graphene and partially wrapped multi-wall carbon nanotube as nanofiller. *Chin Chem Lett*. 2017;28(2):201-205. doi:10.1016/j.cclet.2016.06.039

93. Zhou T, Wang X, Liu X, Xiong D. Improved thermal conductivity of epoxy composites using a hybrid multi-walled carbon nanotube/micro-SiC filler. *Carbon*. 2010;48(4):1171-1176. doi:10.1016/j.carbon.2009.11.040

94. Marom G, Fischer S, Tuler FR, Wagner HD. Hybrid effects in composites: conditions for positive or negative effects versus rule-of-mixtures behaviour. *J Mater Sci*. 1978;13(7):1419-1426. doi:10.1007/BF00553194

95. Czigány T. Discontinuous Basalt Fiber-Reinforced Hybrid Composites. In: *Polymer Composites*. Springer-Verlag; 2005:309-328. doi:10.1007/0-387-26213-X_17

96. Prawoto Y, Djuansjah JRP, Shaffiar NB. Re-visiting the 'rule of mixture' used in materials with multiple constituting phases: A technical note on morphological considerations in austenite case study. *Comput Mater Sci*. 2012;65:528-535. doi:10.1016/j.commatsci.2012.08.008

97. Thongruang W, Balik CM, Spontak RJ. Volume-exclusion effects in polyethylene blends filled with carbon black, graphite, or carbon fiber. *J Polym Sci Part B Polym Phys*. 2002;40(10):1013-1025. doi:10.1002/polb.10157

98. Bilotti E, Zhang H, Deng H, Zhang R, Fu Q, Peijs T. Controlling the dynamic percolation of carbon nanotube based conductive polymer composites by addition of secondary nanofillers: The effect on electrical conductivity and tuneable sensing behaviour. *Compos Sci Technol*. 2013;74:85-90. doi:10.1016/j.compscitech.2012.10.008

99. Etika KC, Liu L, Hess LA, Grunlan JC. The influence of synergistic stabilization of carbon black and clay on the electrical and mechanical properties of epoxy composites. *Carbon*. 2009;47(13):3128-3136. doi:10.1016/j.carbon.2009.07.031

100. Ma P-C, Liu M-Y, Zhang H, et al. Enhanced Electrical Conductivity of Nanocomposites Containing Hybrid Fillers of Carbon Nanotubes and Carbon Black. *ACS Appl Mater Interfaces*. 2009;1(5):1090-1096. doi:10.1021/am9000503

101. Li C, Thostenson ET, Chou T-W. Dominant role of tunneling resistance in the electrical conductivity of carbon nanotube–based composites. *Appl Phys Lett*. 2007;91(22):223114. doi:10.1063/1.2819690

102. Sun Y, Bao H-D, Guo Z-X, Yu J. Modeling of the Electrical Percolation of Mixed Carbon Fillers in Polymer-Based Composites. *Macromolecules*. 2009;42(1):459-463. doi:10.1021/ma8023188

103. Zhang SM, Lin L, Deng H, et al. Synergistic effect in conductive networks constructed with carbon nanofillers in different dimensions. *Express Polym Lett*. 2012;6(2):159-168. doi:10.3144/expresspolymlett.2012.17

104. Balberg I, Anderson CH, Alexander S, Wagner N. Excluded volume and its relation to the onset of percolation. *Phys Rev B*. 1984;30(7):3933-3943. doi:10.1103/PhysRevB.30.3933

105. Socher R, Krause B, Hermasch S, Wursche R, Pötschke P. Electrical and thermal properties of polyamide 12 composites with hybrid fillers systems of multiwalled carbon nanotubes and carbon black. 2011;71(8):1053-1059. doi:https://doi.org/10.1016/j.compscitech.2011.03.004

106. Xiong Z-Y, Zhang B-Y, Wang L, Yu J, Guo Z-X. Modeling the electrical percolation of mixed carbon fillers in polymer blends. 2014;70:233-240.

107. Drubetski M, Siegmann A, Narkis M. Electrical properties of hybrid carbon black/carbon fiber polypropylene composites. *J Mater Sci*. 2007;42(1):1-8. doi:10.1007/s10853-006-1203-4

108. Yue L, Pircheraghi G, Monemian SA, Manas-Zloczower I. Epoxy composites with carbon nanotubes and graphene nanoplatelets – Dispersion and synergy effects. 2014;78:268-278.

109. Yurkov GYu, Gubin SP, Pankratov DA, et al. Iron(III) Oxide Nanoparticles in a Polyethylene Matrix. *Inorg Mater*. 2002;38(2):137-145. doi:10.1023/A:1014013110541

110. Haun JB, Yoon T-J, Lee H, Weissleder R. Magnetic nanoparticle biosensors: Magnetic nanoparticle biosensors. *Wiley Interdiscip Rev Nanomed Nanobiotechnol*. 2010;2(3):291-304. doi:10.1002/wnan.84

111. Iacob M, Stiubianu G, Tugui C, et al. Goethite nanorods as a cheap and effective filler for siloxane nanocomposite elastomers. *RSC Adv*. 2015;5(56):45439-45445. doi:10.1039/C5RA03765D

112. Yang R-B, Liang W-F, Lin W-S, Lin H-M, Tsay C-Y, Lin C-K. Microwave absorbing properties of iron nanowire at x-band frequencies. *J Appl Phys*. 2011;109(7):07B527. doi:10.1063/1.3561449

113. Krajewski M, Lin WS, Lin HM, et al. Structural and magnetic properties of iron nanowires and iron nanoparticles fabricated through a reduction reaction. *Beilstein J Nanotechnol*. 2015;6:1652-1660. doi:10.3762/bjnano.6.167

114. Wu M, Zhao Z, He H, Yao X. Preparation and microwave characteristics of magnetic iron fibers. *J Magn Magn Mater*. 2000;217(1-3):89-92. doi:10.1016/S0304-8853(00)00323-1

115. Wu M, He H, Zhao Z, Yao X. Electromagnetic and microwave absorbing properties of iron fibre-epoxy resin composites. *J Phys Appl Phys*. 2000;33(19):2398-2401. doi:10.1088/0022-3727/33/19/309

116. Goodarz Naseri M, Saion EB, Ahangar HA, Hashim M, Shaari AH. Synthesis and characterization of manganese ferrite nanoparticles by thermal treatment method. *J Magn Magn Mater*. 2011;323(13):1745-1749. doi:10.1016/j.jmmm.2011.01.016

117. Tang ZX, Sorensen CM, Klabunde KJ, Hadjipanayis GC. Size-dependent magnetic properties of manganese ferrite fine particles. *J Appl Phys*. 1991;69(8):5279-5281. doi:10.1063/1.348048

118. Amighian J, Mozaffari M, Nasr B. Preparation of nano-sized manganese ferrite (MnFe2O4) via coprecipitation method. *Phys Status Solidi C*. 2006;3(9):3188-3192. doi:10.1002/pssc.200567054

119. Mohammed EM, Malini KA, Kurian P, Anantharaman MR. Modification of dielectric and mechanical properties of rubber ferrite composites containing manganese zinc ferrite. *Mater Res Bull*. 2002;37(4):753-768. doi:10.1016/S0025-5408(02)00690-6

120. Sahoo B, Sahu SK, Nayak S, Dhara D, Pramanik P. Fabrication of magnetic mesoporous manganese ferrite nanocomposites as efficient catalyst for degradation of dye pollutants. *Catal Sci Technol*. 2012;2(7):1367. doi:10.1039/c2cy20026k

121. Xiong P, Hu C, Fan Y, Zhang W, Zhu J, Wang X. Ternary manganese ferrite/graphene/polyaniline nanostructure with enhanced electrochemical capacitance performance. *J Power Sources*. 2014;266:384-392. doi:10.1016/j.jpowsour.2014.05.048

122. Chakraborty H, Chabri S, Bhowmik N. Electromagnetic Interference Reflectivity of Nanostructured Manganese Ferrite Reinforced Polypyrrole Composites. 2013;14(6):295-298.

123. Lakshmi RV, Bera P, Chakradhar RPS, et al. Enhanced microwave absorption properties of PMMA modified MnFe2O4 –polyaniline nanocomposites. *Phys Chem Chem Phys*. 2019;21(9):5068-5077. doi:10.1039/C8CP06943C

124. Hosseini SH, Mohseni SH, Asadnia A, Kerdari H. Synthesis and microwave absorbing properties of polyaniline/MnFe2O4 nanocomposite. *J Alloys Compd*. 2011;509(14):4682-4687. doi:10.1016/j.jallcom.2010.11.198

125. Hosseini SH, Asadnia A. Synthesis, Characterization, and Microwave-Absorbing Properties of Polypyrrole/MnFe2O4 Nanocomposite. *J Nanomater*. 2012;2012:1-6. doi:10.1155/2012/198973

126. Srivastava RK, Xavier P, Gupta SN, Kar GP, Bose S, Sood AK. Excellent Electromagnetic Interference Shielding by Graphene-MnFe2O4 -Multiwalled Carbon Nanotube Hybrids at Very Low Weight Percentage in Polymer Matrix. *ChemistrySelect*. 2016;1(18):5995-6003. doi:10.1002/slct.201601302

127. Kruželák J, Kvasničáková A, Hložeková K, Dosoudil R, Gořalík M, Hudec I. Electromagnetic Interference Shielding and Physical-Mechanical Characteristics of Rubber Composites Filled with Manganese-Zinc Ferrite and Carbon Black. *Polymers*. 2021;13(4):616. doi:10.3390/polym13040616

128. Phan CH, Mariatti M, Koh YH. Electromagnetic interference shielding performance of epoxy composites filled with multiwalled carbon nanotubes/manganese zinc ferrite hybrid fillers. *J Magn Magn Mater*. 2016;401:472-478. doi:10.1016/j.jmmm.2015.10.067

129. Zhang D-F, Hao Z-F, Zeng B, Qian Y-N, Huang Y-X, Yang Z-D. Theoretical calculation and experiment of microwave electromagnetic property of Ni(C) nanocapsules. *Chin Phys B*. 2016;25(4):040201. doi:10.1088/1674-1056/25/4/040201

130. Wu N, Liu X, Zhao C, Cui C, Xia A. Effects of particle size on the magnetic and microwave absorption properties of carbon-coated nickel nanocapsules. *J Alloys Compd*. 2016;656:628-634. doi:10.1016/j.jallcom.2015.10.027

131. Saini L, Patra MK, Dhaka MK, et al. Ni/graphitic carbon core–shell nanostructure-based light weight elastomeric composites for Ku-band microwave absorption applications. *CrystEngComm*. 2018;20(32):4630-4640. doi:10.1039/C8CE00620B

132. Li D, Liao H, Kikuchi H, Liu T. Microporous Co@C Nanoparticles Prepared by Dealloying CoAl@C Precursors: Achieving Strong Wideband Microwave Absorption via Controlling Carbon Shell Thickness. *ACS Appl Mater Interfaces*. 2017;9(51):44704-44714. doi:10.1021/acsami.7b13538

133. Zhang D, Xu F, Lin J, Yang Z, Zhang M. Electromagnetic characteristics and microwave absorption properties of carbon-encapsulated cobalt

nanoparticles in 2–18-GHz frequency range. *Carbon*. 2014;80:103-111. doi:10.1016/j.carbon.2014.08.044

134. Liu X, Wu N, Cui C, Li Y, Zhou P, Bi N. Facile preparation of carbon-coated Mg nanocapsules as light microwave absorber. *Mater Lett*. 2015;149:12-14. doi:10.1016/j.matlet.2015.02.095

135. Khani O, Shoushtari MZ, Farbod M. Excellent improvement in the static and dynamic magnetic properties of carbon coated iron nanoparticles for microwave absorption. *Phys B Condens Matter*. 2015;477:33-39. doi:10.1016/j.physb.2015.08.007

136. Zhang XF, Dong XL, Huang H, Lv B, Lei JP, Choi CJ. Microstructure and microwave absorption properties of carbon-coated iron nanocapsules. *J Phys Appl Phys*. 2007;40(17):5383-5387. doi:10.1088/0022-3727/40/17/056

137. Knauth P, Di Vona ML, eds. *Solid State Proton Conductors: Properties and Applications in Fuel Cells*. John Wiley & Sons; 2012.

138. Grigas. *Microwave Dielectric Spectroscopy of Ferroelectrics and Related Materials.* CRC PRESS; 2020.

139. Jackson JD. *Classical Electrodynamics*. Wiley; 1962.

140. Baker-Jarvis J, Vanzura EJ, Kissick WA. Improved technique for determining complex permittivity with the transmission/reflection method. *IEEE Trans Microw Theory Tech*. 1990;38(8):1096-1103. doi:10.1109/22.57336

141. Nielsen ED. Scattering by a Cylindrical Post of Complex Permittivity in a Waveguide. *IEEE Trans Microw Theory Tech*. 1969;17(3):148-153. doi:10.1109/TMTT.1969.1126913

142. Pashkin A, Buixaderas E, Kužel P, Liang M-H, Hu C-T, Lin I-N. THZ transmission spectroscopy applied to dielectrics and microwave ceramics. *Ferroelectrics*. 2001;254(1):113-120. doi:10.1080/00150190108214992

143. Ruan X, Chan CH. Terahertz free-space dielectric property measurements using time- and frequency-domain setups. *Int J RF Microw Comput-Aided Eng*. 2019;29(9). doi:10.1002/mmce.21839

144. Zeng M, Liu J, Yue M, et al. High-frequency electromagnetic properties of the manganese ferrite nanoparticles. *J Appl Phys*. 2015;117(17):17B527. doi:10.1063/1.4917515

145. Fiorillo F, Coïsson M, Beatrice C, Pasquale M. Permeability and losses in ferrites from dc to the microwave regime. *J Appl Phys*. 2009;105(7):07A517. doi:10.1063/1.3068533

146. Bellucci S, Coderoni L, Micciulla F, Rinaldi G, Sacco I. Mechanical and Electrical Characterization of Polymer Nanocomposites with Carbon Nanotubes. *Nanosci Nanotechnol Lett*. 2011;3(6):826-834. doi:10.1166/nnl.2011.1248

147. Erokhin AV, Lokteva ES, Yermakov AYe, et al. Phenylacetylene hydrogenation on Fe@C and Ni@C core–shell nanoparticles: About intrinsic activity of graphene-like carbon layer in H2 activation. *Carbon*. 2014;74:291-301. doi:10.1016/j.carbon.2014.03.034

148. Tsurin VA, Yermakov AYe, Uimin MA, et al. Synthesis, structure, and magnetic properties of iron and nickel nanoparticles encapsulated into carbon. *Phys Solid State*. 2014;56(2):287-301. doi:10.1134/S1063783414020309

149. Bychanok D, Gorokhov G, Meisak D, et al. Design of Carbon Nanotube-Based Broadband Radar Absorber for Ka-Band Frequency Range. *Prog Electromagn Res M*. 2017;53:9-16. doi:10.2528/PIERM16090303

150. Bychanok D, Kuzhir P, Maksimenko S, Bellucci S, Brosseau C. Characterizing epoxy composites filled with carbonaceous nanoparticles from dc to microwave. *J Appl Phys*. 2013;113(12):124103. doi:10.1063/1.4798296

151. Bellucci S, Coderoni L, Micciulla F, Rinaldi G, Sacco I. The Electrical Properties of Epoxy Resin Composites Filled with Cnts and Carbon Black. *J Nanosci Nanotechnol*. 2011;11(10):9110-9117. doi:10.1166/jnn.2011.4281

152. Kirkpatrick S. Percolation Phenomena in Higher Dimensions: Approach to the Mean-Field Limit. *Phys Rev Lett*. 1976;36(2):69-72. doi:10.1103/PhysRevLett.36.69

153. Deng Y, Blöte HWJ. Monte Carlo study of the site-percolation model in two and three dimensions. *Phys Rev E*. 2005;72(1):016126. doi:10.1103/PhysRevE.72.016126

154. Okotrub AV, Bulusheva LG, Kudashov AG, Belavin VV, Komogortsev SV. Arrays of carbon nanotubes aligned perpendicular to the substrate surface: Anisotropy of structure and properties. *Nanotechnologies Russ*. 2008;3(3-4):191-200. doi:10.1134/S1995078008030051

155. Shlyakhova EV, Yudanov NF, Okotrub AV, Shubin YuV, Yudanova LI, Bulusheva LG. Growth of carbon nanotubes via chemical vapor deposition on Co catalyst nanoparticles dispersed in CaO. *Inorg Mater*. 2008;44(3):213-218. doi:10.1134/S0020168508030011

156. Gusel'nikov AV, Safronov AV, Kurenya AG, et al. A Laboratory CVD Reactor for the Synthesis of Vertically Oriented Carbon Nanotube Arrays. *Instrum Exp Tech*. 2018;61(4):604-609. doi:10.1134/S002044121804019X

157. Bertasius P, Meisak D, Macutkevic J, et al. Fine Tuning of Electrical Transport and Dielectric Properties of Epoxy/Carbon Nanotubes Composites via Magnesium Oxide Additives. *Polymers*. 2019;11(12):2044. doi:10.3390/polym11122044

158. Lubin G, Society of Plastics Engineers. *Handbook of Composites*.; 1982.

159. Cheng C, Chen Z, Huang Z, et al. Simultaneously improving mode I and mode II fracture toughness of the carbon fiber/epoxy composite laminates via interleaved with uniformly aligned PES fiber webs. *Compos Part Appl Sci Manuf*. 2020;129:105696. doi:10.1016/j.compositesa.2019.105696

160. Zhang R-H, Shi X-T, Tang L, et al. Thermally Conductive and Insulating Epoxy Composites by Synchronously Incorporating Si-sol Functionalized Glass Fibers and Boron Nitride Fillers. *Chin J Polym Sci*. 2020;38(7):730-739. doi:10.1007/s10118-020-2391-0

161. Fu M, Yu Y, Xie JJ, et al. Significant influence of film thickness on the percolation threshold of multiwall carbon nanotube/low density polyethylene composite films. *Appl Phys Lett*. 2009;94(1):012904. doi:10.1063/1.3056055

162. Ameli A, Jung PU, Park CB. Electrical properties and electromagnetic interference shielding effectiveness of polypropylene/carbon fiber composite foams. *Carbon*. 2013;60:379-391. doi:10.1016/j.carbon.2013.04.050

163. Kuzhir P, Paddubskaya A, Bychanok D, et al. Microwave probing of nanocarbon based epoxy resin composite films: Toward electromagnetic shielding. *Thin Solid Films*. 2011;519(12):4114-4118. doi:10.1016/j.tsf.2011.01.198

164. Plyushch A, Macutkevič J, Banys J, et al. Carbon-Coated Nickel Nanoparticles: Effect on the Magnetic and Electric Properties of

Composite Materials. *Coatings*. 2018;8(5):165. doi:10.3390/coatings8050165

165. Palaimiene E, Macutkevic J, Banys J, et al. Ultra-low percolation threshold in epoxy resin–onion-like carbon composites. *Appl Phys Lett*. 2018;113(3):033105. doi:10.1063/1.5030526

166. Deng H, Lin L, Ji M, Zhang S, Yang M, Fu Q. Progress on the morphological control of conductive network in conductive polymer composites and the use as electroactive multifunctional materials. *Prog Polym Sci*. 2014;39(4):627-655. doi:10.1016/j.progpolymsci.2013.07.007

167. Christensen K. *Percolation Theory*. Vol 1.; 2002.

168. Plyushch A, Macutkevic J, Kuzhir P, et al. Electromagnetic properties of graphene nanoplatelets/epoxy composites. *Compos Sci Technol*. 2016;128:75-83. doi:10.1016/j.compscitech.2016.03.023

169. Brosseau C, Achour ME. Variable-temperature measurements of the dielectric relaxation in carbon black loaded epoxy composites. *J Appl Phys*. 2009;105(12):124102. doi:10.1063/1.3149702

170. Jonscher AK. New interpretation of dielectric loss peaks. *Nature*. 1975;256(5518):566-568. doi:10.1038/256566a0

171. Garca-Coln LS, del Castillo LF, Goldstein P. Theoretical basis for the Vogel-Fulcher-Tammann equation. *Phys Rev B*. 1989;40(10):7040-7044. doi:10.1103/PhysRevB.40.7040

172. Tammann G, Hesse W. Die Abhängigkeit der Viscosität von der Temperatur bie unterkühlten Flüssigkeiten. *Z Für Anorg Allg Chem*. 1926;156(1):245-257. doi:10.1002/zaac.19261560121

173. Fulcher GS. Analysis of recent measurements of the viscosity of glasses. *J Am Ceram Soc*. 1925;8(6):339-355. doi:10.1111/j.1151-2916.1925.tb16731.x

174. Saslow WM. Scenario for the Vogel-Fulcher “law.” *Phys Rev B*. 1988;37(1):676-678. doi:10.1103/PhysRevB.37.676

175. Kim DH, Won Y-Y. In Situ Polymerized Carbon Nanotube/Polyimide Nanocomposites: Effect of Reaction Stoichiometry on the Glass Transition Properties of the Nanocomposites: In Situ-Polymerized

Carbon Nanotube/Polyimide Nanocomposites: Effect …. *Macromol React Eng*. 2012;6(1):45-56. doi:10.1002/mren.201100027

176. Almond D, Duncan G, West A. The determination of hopping rates and carrier concentrations in ionic conductors by a new analysis of ac conductivity. *Solid State Ion*. 1983;8(2):159-164. doi:10.1016/0167-2738(83)90079-6

177. Banys J, Macutkevic J, Samulionis V, Brilingas A, Vysochanskii Yu. Dielectric and ultrasonic investigation of phase transition in cuinp2s6 crystals. *Phase Transit*. 2004;77(4):345-358. doi:10.1080/01411590410001667608

178. Kim HM, Choi M-S, Joo J, Cho SJ, Yoon HS. Complexity in charge transport for multiwalled carbon nanotube and poly(methyl methacrylate) composites. *Phys Rev B*. 2006;74(5):054202. doi:10.1103/PhysRevB.74.054202

179. Barsoukov E, Macdonald JR, eds. *Impedance Spectroscopy: Theory, Experiment, and Applications*. Third edition. Wiley; 2018.

180. Laidler KJ. The development of the Arrhenius equation. *J Chem Educ*. 1984;61(6):494. doi:10.1021/ed061p494

181. Macutkevic J, Kuzhir PP, Paddubskaya AG, et al. Broadband dielectric/electric properties of epoxy thin films filled with multiwalled carbon nanotubes. *J Nanophotonics*. 2013;7(1):073593. doi:10.1117/1.JNP.7.073593

182. Macutkevic J, Kuzhir P, Paddubskaya A, et al. Electrical transport in carbon black-epoxy resin composites at different temperatures. *J Appl Phys*. 2013;114(3):033707. doi:10.1063/1.4815870

183. Plyushch A, Macutkevic J, Kuzhir PP, Banys J, Fierro V, Celzard A. Dielectric properties and electrical conductivity of flat micronic graphite/polyurethane composites. *J Nanophotonics*. 2015;10(1):012511. doi:10.1117/1.JNP.10.012511

184. Baker DR, Paul G, Sreenivasan S, Stanley HE. Continuum percolation threshold for interpenetrating squares and cubes. *Phys Rev E*. 2002;66(4):046136. doi:10.1103/PhysRevE.66.046136

185. Ota T, Fukushima M, Ishigure Y, et al. Control of percolation curve by filler particle shape in Cu- SBR composites. *J Mater Sci Lett*. 1997;16(13):1182-1183. doi:10.1023/A:1018513127504

186. Jing X, Zhao W, Lan L. The effect of particle size on electric conducting percolation threshold in polymer/conducting particle composites. *J Mater Sci Lett*. 2000;19(5):377-379. doi:10.1023/A:1006774318019

187. Karásek L, Meissner B, Asai S, Sumita M. Percolation Concept: Polymer-Filler Gel Formation, Electrical Conductivity and Dynamic Electrical Properties of Carbon-Black-Filled Rubbers. *Polym J*. 1996;28(2):121-126. doi:10.1295/polymj.28.121

188. Mamunya YeP, Muzychenko YuV, Pissis P, Lebedev EV, Shut MI. Percolation phenomena in polymers containing dispersed iron. *Polym Eng Sci*. 2002;42(1):90-100. doi:10.1002/pen.10930

189. Alvarez MP, Poblete VH, Pilleux ME, Fuenzalida VM. Submicron copper-low-density polyethylene conducting composites: Structural, electrical, and percolation threshold. *J Appl Polym Sci*. 2006;99(6):3005-3008. doi:10.1002/app.23013

190. Lonjon A, Demont P, Dantras E, Lacabanne C. Low filled conductive P(VDF-TrFE) composites: Influence of silver particles aspect ratio on percolation threshold from spheres to nanowires. *J Non-Cryst Solids*. 2012;358(23):3074-3078. doi:10.1016/j.jnoncrysol.2012.09.006

191. Brouers F. Percolation threshold and conductivity in metal-insulator composite mean-field theories. *J Phys C Solid State Phys*. 1986;19(36):7183-7193. doi:10.1088/0022-3719/19/36/010

192. Pinto G, Maidana MB. Conducting polymer composites of zinc-filled nylon 6. *J Appl Polym Sci*. 2001;82(6):1449-1454. doi:10.1002/app.1983

193. Balberg I, Azulay D, Goldstein Y, Jedrzejewski J, Ravid G, Savir E. The percolation staircase model and its manifestation in composite materials. *Eur Phys J B*. 2013;86(10):428. doi:10.1140/epjb/e2013-40200-7

194. Grunlan JC, Gerberich WW, Francis LF. Lowering the percolation threshold of conductive composites using particulate polymer microstructure. *J Appl Polym Sci*. 2001;80:692-705.

195. Mamunya EP, Davidenko VV, Lebedev EV. Effect of polymer-filler interface interactions on percolation conductivity of thermoplastics filled with carbon black. *Compos Interfaces*. 1996;4(4):169-176. doi:10.1163/156855497X00145

196. Flandin L, Prasse T, Schueler R, Schulte K, Bauhofer W, Cavaille J-Y. Anomalous percolation transition in carbon-black–epoxy composite

materials. *Phys Rev B*. 1999;59(22):14349-14355. doi:10.1103/PhysRevB.59.14349

197. Ezquerra TA, Martinez-Salazar J, Baltá Calleja FJ. Percolation threshold of conductive polycarbonate/carbon composites as revealed by electron microscopy. *J Mater Sci Lett*. 1986;5(10):1065-1066. doi:10.1007/BF01730285

198. Al-Saleh MH, Sundararaj U. An innovative method to reduce percolation threshold of carbon black filled immiscible polymer blends. *Compos Part Appl Sci Manuf*. 2008;39(2):284-293. doi:10.1016/j.compositesa.2007.10.010

199. Mamunya YeP, Davydenko VV, Pissis P, Lebedev EV. Electrical and thermal conductivity of polymers filled with metal powders. *Eur Polym J*. 2002;38(9):1887-1897. doi:10.1016/S0014-3057(02)00064-2

200. Pötschke P, Dudkin SM, Alig I. Dielectric spectroscopy on melt processed polycarbonate—multiwalled carbon nanotube composites. *Polymer*. 2003;44(17):5023-5030. doi:10.1016/S0032-3861(03)00451-8

201. Kirkpatrick S. Percolation and Conduction. *Rev Mod Phys*. 1973;45(4):574-588. doi:10.1103/RevModPhys.45.574

202. Kostarelos K. The long and short of carbon nanotube toxicity. *Nat Biotechnol*. 2008;26(7):774-776. doi:10.1038/nbt0708-774

203. Andreev AS, Kazakova MA, Ishchenko AV, et al. Magnetic and dielectric properties of carbon nanotubes with embedded cobalt nanoparticles. *Carbon*. 2017;114:39-49. doi:10.1016/j.carbon.2016.11.070

204. Zhan Y, Wang J, Zhang K, et al. Fabrication of a flexible electromagnetic interference shielding Fe3O4@reduced graphene oxide/natural rubber composite with segregated network. *Chem Eng J*. 2018;344:184-193. doi:10.1016/j.cej.2018.03.085

205. Crespo M, Méndez N, González M, Baselga J, Pozuelo J. Synergistic effect of magnetite nanoparticles and carbon nanofibres in electromagnetic absorbing composites. *Carbon*. 2014;74:63-72. doi:10.1016/j.carbon.2014.02.082

206. Pang H, Sahu RP, Duan Y, Puri IK. MnFe2O4-coated carbon nanotubes with enhanced microwave absorption: Effect of CNT content and

hydrothermal reaction time. *Diam Relat Mater*. 2019;96:31-43. doi:10.1016/j.diamond.2019.04.027

207. Sheng P, Sichel EK, Gittleman JI. Fluctuation-Induced Tunneling Conduction in Carbon-Polyvinylchloride Composites. *Phys Rev Lett*. 1978;40(18):1197-1200. doi:10.1103/PhysRevLett.40.1197

208. Jäger K-M, McQueen DH, Vilcáková J. Ac conductance and capacitance of carbon black polymer composites during thermal cycling and isothermal annealing. *J Phys Appl Phys*. 2002;35(10):1068-1075. doi:10.1088/0022-3727/35/10/316

209. Bychanok D, Angelova P, Paddubskaya A, et al. Terahertz absorption in graphite nanoplatelets/polylactic acid composites. *J Phys Appl Phys*. 2018;51(14):145307. doi:10.1088/1361-6463/aab1a5

210. Mirzaee M, Noghanian S, Chang I. Low-profile bowtie antenna with 3D printed substrate. *Microw Opt Technol Lett*. 2017;59(3):706-710. doi:10.1002/mop.30379

211. Gaylor K, Materials Research Laboratory (Australia). *Radar Absorbing Materials - Mechanisms and Materials*. DSTO Materials Research Laboratory; 1989.

212. Crooks LE. Noise reduction techniques in electronic systems (2nd ed.), Henry W. Ott. Wiley-Interscience, New York. 1988. *Magn Reson Med*. 1989;10(3):426-427. doi:10.1002/mrm.1910100315

213. Hund E. *Microwave Communications: Components and Circuits*. McGraw-Hill; 1989.

214. Ivanov E, Kotsilkova R, Xia H, et al. PLA/Graphene/MWCNT Composites with Improved Electrical and Thermal Properties Suitable for FDM 3D Printing Applications. *Appl Sci*. 2019;9(6):1209. doi:10.3390/app9061209

215. Kotsilkova R, Petrova-Doycheva I, Menseidov D, Ivanov E, Paddubskaya A, Kuzhir P. Exploring thermal annealing and graphene-carbon nanotube additives to enhance crystallinity, thermal, electrical and tensile properties of aged poly(lactic) acid-based filament for 3D printing. *Compos Sci Technol*. 2019;181:107712. doi:10.1016/j.compscitech.2019.107712

216. Chung B-K. Dielectric constant measurement for thin material at microwave frequencies. *Prog Electromagn Res*. 2007;75:239-252. doi:10.2528/PIER07052801

217. Méjean C, Pometcu L, Benzerga R, et al. Electromagnetic absorber composite made of carbon fibers loaded epoxy foam for anechoic chamber application. *Mater Sci Eng B*. 2017;220:59-65. doi:10.1016/j.mseb.2017.03.009

218. Nornikman H, Malek F, Soh PJ, Azremi AAH, Ismahayati A. Reflection Loss Performance of Triangular Microwave Absorber. In: *International Symposium on Antennas and Propagation (ISAP 2010)*. ; 2010.

219. Piekarz I, Sorocki J, Slomian I, Wincza K, Gruszczynski S. Experimental Verification of 3D Printed Low-Conductivity Graphene-Enhanced PLA Absorbers for Back Lobe Suppression in Aperture-Coupled Antennas. In: *2018 IEEE-APS Topical Conference on Antennas and Propagation in Wireless Communications (APWC)*. IEEE; 2018:780-782. doi:10.1109/APWC.2018.8503752

220. Adachi S, Hattori M, Kanno F, Kiuchi K, Okada T, Tajima O. Production method of millimeter-wave absorber with 3D-printed mold. *Rev Sci Instrum*. 2020;91(1):016103. doi:10.1063/1.5132871

221. Zhu Y, Liu L, Zhang Y, et al. Development of millimeter-wave EM absorber with homogenization theory. *SN Appl Sci*. 2019;1(5):398. doi:10.1007/s42452-019-0418-3

4. SANTRAUKA LIETUVIŲ KALBA

Objektų, kurių matmenys nanometrų eiles, savybių tyrimai yra perspektyvi, intensyviai besivystanti mokslo kryptis. Viena iš nanodalelių dalelių tyrimų populiarumo priežasčių yra jų galimybė valdyti polimerų savybes į juos įterpiant nedidelį kiekį nanodalelių, o tai lemia naujų kompozicinių medžiagų, turinčių pageidaujamas savybes, sukūrimą. Dar daugiau, mažėjant dalelės dydžiui (nuo kelių mikrometrų iki kelių nanometrų)[1], dalelės paviršiaus plotas didėja, dėl ko didėja sąveika tarp užpildo dalelių ir tarp mišrių fazių[2].

Elektriškai laidūs polimeriniai kompozitai užima ypatinga vieta kompozitų technologijoje dėl ypatingai plataus įvairių taikymų diapazono: antistatinės medžiagos[3], laidus sluoksniai ir dangos[4], saulės elementai ir biosensoriai[5], elektromagnetinio slopinimo medžiagos[6], ir kiti taikymai. Pats paprasčiausias būdas padaryti elektriškai laidų polimerą pridėti į gerai žinomus polimerus anglies nanodalelių, tačiau nanodalelės ne anglies pagrindu (pavyzdžiui goetitai, feritai, metalo nanodalelės) irgi susilaikė dėmesio kaip polimerų priedai. Polimerai su magnetinėmis nanodalelėmis gali būti taikomi kaip laidžios medžiagos, turinčios magnetinių arba feromagnetinių savybių[7].

Kompozitų turinčių unikalias elektromagnetines ir mechanines tobulinimas yra labai sudėtingas dalykas dėl to kad nanodalelės turi tendenciją aglomeruoti[8]. Tačiau panaudojus vienu metu įvairių nanoužpildų kombinacijas gali būti lengva ir daug žadanti strategiją tobulinant kompozitų elektromagnetines savybes. Tokios manipuliacijos leidžia pasiekti ne tik atskirų užpildų mišinio privalumus, bet taip pat ir sinegetinius efektus, kurie atsiranda dėl to kad skirtingo tipo nanodalelės trikdo nanodalelių aglomeraciją ir susiformoja vienas kitą palaikantys skirtingos cheminės sudėties nanodalelių tinklai[9]. Tačiau šis efektas iki šiol nebuvo tyrinėtas.

Šis darbas yra skirtas kelių epoksidinių kompozitų sistemų tyrimams: (i) kompozitai su skirtingomis magnetinėmis dalelėmis ir (ii) trijų komponentų hibridai su magnetiniemis nanodalelėmis ir daugiasieniais anglies nanovamzdeliais (DANV). Eksperimentiniai matavimai skirti šių medžiagų dielektrinių/elektrinių savybių tyrimams plačiame dažnių ir temperatūrų intervaluose. Be to, pademonstruotas naujas kompaktiškų mikrobangų absorberių ir bangolaidžių suderintų apkrovų dizainas, pagrįstas laidžiu nuostolingu kompozitu.

Disertacijos tikslai ir uždaviniai

Pagrindinis šios disertacijos tikslas yra ištirti epoksidinių kompozitų su magnetiniais nanointarpais dielektrines savybes ir rasti sinergijos efektus tarp dviejų užpildų hibridiniuose kompozituose. Kitas tikslas yra rasti ryšį tarp piramidinės periodinės struktūros (pagrįstos laidžiaja nuostolinga medžiaga) mikrobangų elektromagnetinių savybių ir jos geometrijos, kad būtų pasiektas didesnis ekranavimo efektyvumas.

Disertacijos tikslams pasiekti buvo sprendžiami šie uždaviniai:

1. Ištirti epoksidinių kompozitų, užpildytų įvairių rūšių magnetinėmis nanodalelėmis ($Fe_2O_3 \cdot H_2O$, $MnFe_2O_4$, Ni@C (nikelio nanodalelės padengtos anglimi)) dielektrines savybes plačiame dažnių ir temperatūrų intervale.
2. Ištirti hibridinių epoksidinių kompozitų su DANV ir nedidelių kiekių magnetinių nanodalelių dielektrines savybes.
3. Eksperimentiškai ir atlėkant skaitmenines simuliacijas ištirti piramidinės periodinės struktūros, pagrįstos laidžiaja nuostolinga medžiaga, mikrobangų elektromagnetines savybes.

Disertacijos gynamieji teiginiai

1. Sferinių dalelių perkoliacijos slenkstis polimerų matricoje gali labai skirtis: $MnFe_2O_4$ / epoksidinės kompozitų sistemoje perkoliacijos slenkstis yra artimas 30% tūrinės koncentracijos, kas sutampa su teoriniu įvertinimu; o Ni@C / epoksidinės dervos kompozito elektrinės perkoliacijos slenkstis yra tarp 10% ir 15% tūrinės koncentracijos. Polimerų ir užpildų sąveikų skirtumas sąlygoja perkoliacinio tinklo atsiradimą esant mažesnėms Ni@C nanodalelių koncentracijoms.
2. Epoksidinės dervos kompozitų su nedideliu kiekiu DANV, kurių koncentracija yra žemiau perkoliacijos slenkščio, elektromagnetinės savybės gali būti žymiai pagerintos plačiame temperatūrų diapazone, pridedant tam tikrus nedidelius magnetinių intarpų kiekius; šie efektas atsiranda dėl pagerėjusio dalelių pasiskirstymo polimerinėje matricoje sukuriant palankų perkoliacinį tinklą.
3. Piramidinės periodinės struktūros pavyzdžiu pademonstruota laidžių nuostolingų medžiagų panaudojimo perspektyva miniatiurizuojant

mikrobangų įtaisus. Ekranavimo efektyvumo padidinimui pasiūlytas optimalių piramidžių geometrinių parametrų įvertinimo modelis (atsižvelgiant į jo tūrines charakteristikas ir į numatytą dažnių diapazoną).

Mokslinio darbo naujumas ir aktualumas

1. Atliktas kelių epoksidinių kompozitų su skirtingų rūšių magnetinėmis nanodalelėmis ($Fe_2O_3 \cdot H_2O$, $MnFe_2O_4$, Ni@C) dielektrinių savybių eksperimentinis tyrimas plačiame dažnių ir temperatūrų intervaluose. Buvo nustatytos kiekvienos sistemos elektrinės perkoliacijos slenksčiai. Buvo parodytos ir paaiškintos kompozitų dielektrinies skvarbos ir elektrinio laidumo temperatūros ir dažnio spektrų elgsenos ypatumai esant užpildų koncentracijoms tiek žemiau, tiek aukščiau perkoliacijos slenksčio.
2. Atliktas hibridinių epoksidinės dervos / DANV / $MnFe_2O_4$ ir epoksidinės dervos /DANV /Ni@C kompozitų dielektrinių savybių eksperimentinis tyrimas plačiame dažnių ir temperatūrų intervaluose. Abiejose sistemose, kai DANV koncentracija yra žemiau perkoliacijos slenksčio, esant tam tikram mažam magnetinių nanodalelių kiekiui, buvo pademonstruota ryški elektrinių savybių sinergija. Sinergijos efektas buvo paaiškintas DANV pasiskirstymo pagerėjimu dėl dviejų tipų užpildų palankiai suformoto bendrojo elektros perkoliacinio tinklo.
3. Buvo pasiulyta piramidinė periodinė struktūra, pagrįsta elektrai laidžia medžiaga, kaip efektyvus kompaktiškas mikrobangų absorberis ir bangolaidžių suderintą apkrovą. Priešeksperimentiniame etape piramidžių parametrams įvertinti buvo sėkmingai naudojamas ekranavimo efektyvumo optimizavimo metodas, kuriame atsižvelgiama į medžiagos savybes, reikiamą dažnių diapazoną ir struktūros geometriją. Eksperimentiškai įrodyta, kad piramidžių su apskaičiuotais optimaliais parametrais slopinimo efektyvumas yra 20 dB tiek atspindėtiems, tiek perduotiems signalams mikrobangų dažnių diapazone.

Autories indėlis

Darbe pateiktus dielektrinius tyrimus disertacijos autorė atliko pati asmeniškai, prižiūrima vado dr. Jan Macutkevič. Ji taip pat pati pagamino visus epoksidinius kompozitus Baltarusijos valstybinio universiteto

Branduolinių problemų instituto nanoelektromagnetizmo laboratorijoje. Piramidinių struktūrų elektromagnetinių savybių modelis buvo sukurtas dr. Dz. Bychanok. Paskelbtus straipsnius autorė parašė diskutojant su J. Macutkevič, P. Kuzhir, J. Banys, D. Bychanok ir kitais bendraautoriais.

Disertacijos struktūra

Disertacija yra sudaryta iš trijų skyrių, išvadų ir santraukos, cituojamos literatūros sąrašo. Cituojamos literatūros sąraše yra 221 nuorodą.

4.1 Apžvalga

Kompozitinė medžiaga (arba kompozitas) yra heterogeninė sistema sudaryta iš dvėjų arba daugiau skirtingų fazių su reikšminga tarpafazinė sąveika. Kompozitas gali pasižymėtis savybėmis kurios yra skirtingos negu jį sudarančių komponenčių savybės. Polimerinių kompozitų su įvairiais intarpais tyrimai yra labai populiarus, kadangi palyginus su kitomis medžiagomis jie yra lengvi, nebijo korozijos, pigūs, lengvai pagaminami ir jų savybės gali būti lengvai keičiamos[10]. Dažniausiai kompozitų savybės yra apsrendžiamos ne nanodalelių savybėmis, bet jų klasterių savybėmis, nes nanodalelės yra linkę aglomeruoti polimerinės matricos viduje[11]. Vienas iš svarbesniu plačiajuosčių elektrinių tyrimų kompozitų su nanodalelėmis uždavinių yra nustatyti sąryšį tarp nanodalelių (arba jų klasterių) savybių, šių dalelių pasiskirstymo ir kompozitų elektrinių savybių plačiame dažnių ir temperatūrų intervale. Kompozitų elektrinių savybių temperatūrinės priklausomybės yra lemiamos neigiamo arba teigiamo varžos efekto, kuris gali būti sąlygotas dalelių persiskirstymo, polimerinės matricos elektrinio laidumo arba matricos šiluminių savybių, elektronų tunelivimo tarp laidžių klasterių arba jų tuneliavimo į laidžią polimerinę matricą[12].

Perkoliacijos teorija

Kompozitinių medžiagų fizikinių savybių dramatiniai pokyčiai atsiranda kai užpildo dalelės suformuoja perkoliacinį tinklą (sudarant elektrinius kontaktus tarp dalelių). Perkoliacija atsiranda esant tam tikrai minimaliai tūrinei užpildo dalelių koncentracijai p, kuri yra vadinama perkoliacijos slenksčiu p_c. Arti perkoliacijos slenksčio dielektrinės skvarbos priklausomybė nuo tūrinės užpildo koncentracijos aprašo laipsninė funkcija[13]:

$$\varepsilon' \propto (p_c - p)^{-t} \tag{4.1}$$

čia ε' yra dielektrinė skvarba, t konstanta. Šis perkoliacijos modelis nepriklauso nuo užpildo dalelių bei matricos fizikinės prigimties ir gali būti pritaikytas įvairiems kompozitams kur matrica yra izoliatorius, o užpildas elektriškai laidžios dalelės.

Maksvelo-Vagnerio relaksacija

Elektrinės perkoliacijos aplinkoje kompozitų plačiajuostės elektrinės savybės dažniausiai yra apsprendžiamos Maksvelo-Vagnerio relaksacijos[14]. Tokiu atveju yra labai naudingas elektrinio impedanso formalizmas. Kompleksinis elektrinis impedansas yra atvirkštinis dydis kompleksiniam elektriniam laidumui. Medžiagų kompleksinis impedansas Z^* gali būti modeliuojamas ekvivalentinėmis grandinėmis. Pavyzdžiui, kompleksinį impedansą galima aprašyti begaline seka RC grandinių sujungtų nuosekliai:

$$Z^*(\omega) = Z_\infty + \Delta Z \int_{-\infty}^{\infty} \frac{f(\tau)}{1+i\omega\tau} d(\lg\tau) \tag{4.2}$$

kur $\tau = RC$, o $f(\tau)$ yra relaksacijos trukmių pasiskirstymo funkcija, Z_∞ yra aukštadažnis, nuo dažnio nepriklausantis, impedansas, ΔZ yra skirtumas tarp impedanso nuolatinei srovei ir aukštadažnio impedanso. Lygtis (4.2) funkcijos $f(\tau)$ atžvilgiu yra pirmos rūšies Fredholmo integralinė lygtis. Relaksacijos trukmių pasiskirstymo funkcija $f(\tau)$ gali būti apskaičiuota pasinaudojus Tichonovo reguliarizacijos metodu[15].

Daugiasluoksnės sistemos elektromagnetinės savybės

Kai elektromagnetinė banga krenta statmenai plokštumai lygiagrečiai daugiasluoksnei sistemai atsiranda atspindžiai nuo kiekvieno sluoksnio ribos, ir daugiasluoksnės sistemos savybės gali būti nustatytos sumojant visus atspindžius. Toks nagrinėjimas apribotas plonų sluoksnių priartėjimu, kai praeitų kelių skirtumas yra mažesnis negu elektromagnetinės bangos ilgis.

Jeigu yra sistema sudaryta iš N sluoksnių, elektromagnetines savybes (atspindžio ir pralaidumo koeficientai R ir T, atitinkamai) gali būti nustatytos pasinaudojus daugiasluoksnių metodų, išvystytu optikoje[16]:

$$R = S_{11}^2 = \frac{(n_0 - \frac{C}{B})^2}{(n_0 + \frac{C}{B})^2} \tag{4.3}$$

$$T = S_{21}^2 = \frac{4n_0^2}{(n_0 + \frac{C}{B})^2} \tag{4.4}$$

kur

$$\begin{bmatrix} B \\ C \end{bmatrix} = \left\{ \prod_{t=1}^{N} \begin{bmatrix} \cos(k_t\tau) & i\frac{k_0}{k_t} sin(k_t\tau) \\ i\frac{k_t}{k_0} sin(k_t\tau) & \cos(k_t\tau) \end{bmatrix} \right\} \begin{bmatrix} 1 \\ n_0 \end{bmatrix} \tag{4.5}$$

ir S_{11} ir S_{21} yra santykinės amplitudės atspindėto ir praėjusio signalo, atitnkamai, k_t ir k_0 yra banginiai skaičiai t -sluoksnio kurio storis τ ir lūžio rodiklis n_t (oro lūžio rodiklis $n_0 = 1$). Laisvoje ėrdveje banginiai skaičiai yra $k_t = \frac{2\pi n_t}{\lambda}$ ir $k_0 = \frac{2\pi n_0}{\lambda}$, tuo tarpu bangolaidžio kurio plotis a viduje $k_t = \frac{2\pi}{\lambda a}\sqrt{{n_t}^2 a^2 - \frac{\lambda^2}{4}}$ ir $k_0 = \frac{2\pi}{\lambda a}\sqrt{n_0^2 a^2 - \frac{\lambda^2}{4}}$, čia λ bangos ilgis; c = 3·10 m/s yra šviesos greitis vakuume. Lygtis (4.5) yra tam tikras atvėjis kai n_0 yra oro lūžio rodiklis, tačiau bendruoju atveju tai yra viršutinio sluoksnio lūžio rodiklis.

4.2 Tyrimų metodika

Matavimų metodai

Disertacijoje yra aprašyti eksperimentiniai ir teoriniai plačiajuostės dielektrinės spektroskopijos tyrimų metodai, kuriuos autorė pritaikė ruošiant disertaciją. Žemuose (20 Hz – 1 MHz) dažniuose kompleksinė dielektrinė skvarba buvo nustatyta iš bandinio talpos ir nuostolių tangento. Šie parametrai buvo matuojami LCR matuokliu HP4284A. Aukštesniuose dažniuose (1 MHz – 3 GHz) buvo matuojamas kompleksinis atspindžio koeficientas. Dielektrinė skvarba buvo apskaičiuojama atsižvelgiant į elektromagnetinio lauko pasiskirstymą išilgai bandinėlio[17]. Mikrobanginiame dažnių diapazone (8-53 GHz) buvo naudojami plono cilindrinio strypo arba visiško vidaus užpildymo metodai[17]. Teraherciniame dažnių diapazone (100 GHz – 2 THz) dielektrinėms savybėms tirti buvo pritaikyta laikinės skyros spektroskopija. Šiame dažnių diapazone buvo naudojamas Ekspla komercinis spektrometras,

kurio pagrindiniai dalys yra femtosekundinis lazeris, teraherciniai emiteris ir detektorius (GaBiAs sluoksnių pagrindu) bei vėlinimo linijos. Teraherciniame dažnių diapazone buvo matuojamas kompleksinis pralaidumo koeficientas ir kompleksinė dielektrinė skvarba nustatyta panaudojus Frenelio formulės.

Kompozitų gamyba

Kompozitams paruošti buvo naudojama komercinė Epikote 828 epoksidinė derva, kurios tankis 1.16 g/cm^3, ir trietilenetetramino kietiklis (TETA). Naudojamas polimeras leidžia lengvai disperguoti įvairius priedus ir pasižymi dideliu mechaniniu ir cheminiu atsparumu[18].

Trys komerciškai prieinamų magnetinių nanodalelių tipai, kuriuos pateikė „US Research Nanomaterials, Inc.“, buvo naudojami kaip užpildai atitinkamose kompozituose:

1. *Goetito* ($Fe_2O_3 \cdot H_2O$ alpha, 98%, 50 nm × 10 nm) *nanostulpelių milteliai* (https://www.us-nano.com/inc/sdetail/42381). Tai yra geltonos spalvos lazdelės formos milteliai, plačiai naudojami dengimo, plastiko, dažų ir farmacijos srityse. Nanostulpelių kraštinių santykis yra artimas 5, ką įrodo SEM vaizdas (žr. 4.1a pav.). Nano miltelių tankis yra 4.4 g/cm^3.
2. *Mangano ferito* ($MnFe_2O_4$) *nanomilteliai* su sferinėmis nanodalelėmis 28 ir 60 nm dydžio (https://www.us-nano.com/inc/sdetail/7019 ir https://www.us-nano.com/inc/sdetail/595) abejų miltelių tankis 5.4 g/cm^3.
3. *Ni@C šerdis-apvalkalo nanodalelės* (https://www.us-nano.com/inc/sdetail/171), kurios yra 20 nm storio Ni dalelės, padengtos keliais glaudžiai sutankintais kelių nanometrų storio anglies sluoksniais. Tankis yra 8.9 g/cm^3. Ni@C nanodalelių mikrostruktūra pavaizduota 4.1b paveiksle.

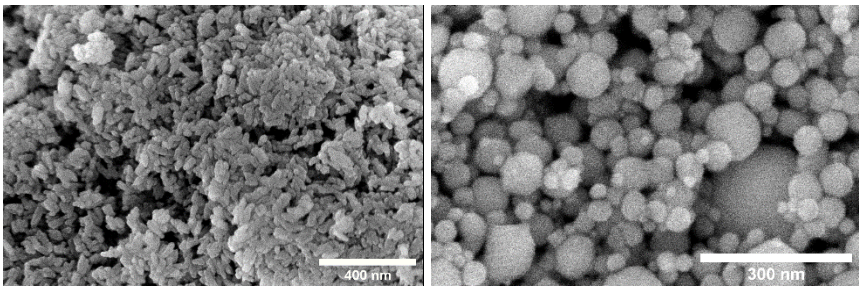

a b

Pav. 4.1: Kompozitų gamybai naudotų goetito nanostulpelių (a) ir Ni@C nanodalelių (b) SEM nuotraukos.

Kiekviena aukščiau paminėtų magnetinių nanodalelių rūšis lengvai disperguojasi polimero matricoje ir leidžia gaminti didelės koncentracijos kompozitus. Kompozitai su vienos rūšies nanodalelėmis buvo paruošti pagal standartinę procedūrą, skirtą įvairių nanodalelių dispergavimui polimerinėje matricoje[19]. Paruošimo procesai kompozitams su goetito nanostulpeliais ir mangano ferito nanodalelėmis visiškai sutampa, o Ni@C pagrindu pagamintiems kompozitams tam tikri procedūros etapai turi nedidelius skirtumus. Pirmame etape reikalingas nanodalelių kiekis buvo mechaniškai susmulkinamas ir maišomas etanolyje ($Fe_2O_3 \cdot H_2O$ ir $MnFe_2O_4$ atveju) arba isopropanolyje (Ni@C atveju) 30 minučių. Tada nanodalelės/alkoholio suspensijos buvo apdorotos 1 valanda ultragarsu: ultragarsinėje vonioje su etanoliu ir zondu izopropanolyje. Vėliau gauti mišiniai buvo sujungti su epoksidine derva ir 1-2 valandas buvo papildomai veikiami ultragarsiniu zondu. Išgarinus alkoholį, į dervos ir nanodalelių mišinį buvo pridėta kietiklio ir rankiniu būdu maišoma 5-7 minutės. Kietiklis pridėtas santykiu 1:10 su epoksidine derva. Mišinys supilamas į formas ir paliekamas 20 valandų kietėjimo procesui kambario temperatūroje, o po to 2 valandas - krosnyje 100 ^oC temperatūroje galutiniam polimerizacijos etapui. Tokie paruošimo procedūros parametrai buvo eksperimentiškai nustatyti kaip optimalūs, kad kiekvienos rūšies nanodalelės būtų geriau disperguojamos epoksidinės dervos matricoje.

Po aukščiau minėtos gaminimo proceduros kompozitų su epoksidines dervos matrica sąrašas yra toks:

1. 0, 5, 10, 20, 30 ir 40% $Fe_2O_3 \cdot H_2O$ užpildų tūrinės koncentracijos;
2. 0, 10, 20, 23, 25, 28 ir 30% $MnFe_2O_4$ užpildų tūrinės koncentracijos;
3. 0, 10, 15, 25 ir 30 vol.% Ni@C užpildų tūrinės koncentracijos.

Užpildų koncentracijos kiekvienam kompozitui buvo parinktos arti teorinės vertės perkoliacijos slenksčio (žemiau ir aukščiau jo)[20]. Tūrinės užpildų koncentracijos buvo apskaičiuotos iš masinių koncentracijų pasinaudojus žinomais medžiagų tankiais.

4.3 Epoksidinės dervos ir magnetinių nanodalelių kompozitų dielektrinės savybės

Goetitio nanostulpelių kompozitai

$Fe_2O_3 \cdot H_2O$/epoksidinių dervos kompozitų dielektrinės skvarbos priklausomybė nuo koncentracijos kambario temperatūroje ir esant 129 Hz dažniui parodyta 4.2a paveiksle. Didėjant nanostulpelių koncentracijai dielektrinė skvarba didėja pagal perkoliacijos dėsnį (Lygtis (4.1)). Aproksimacija šiuo dėsniu parodo, kad $Fe_2O_3 \cdot H_2O$/epoksidinės dervos kompozitų elektrinė perkoliacija yra kai užpildo tūrinė koncentracija yra 40% (žr. 4.2b pav.). Tai patvirtina ir plato laidumo spektruose, tuo tarpu esant mažesnėms užpildo koncentracijoms jokio plato laidumo spektruose nėra. Norint padidinti p_c nustatymo tikslumą, reikia daug daugiau mėginių, kurių skirtingos goetito nanostulpelių koncentracijos yra artimos kritinei vertei.

$Fe_2O_3 \cdot H_2O$ nanostulpelių/epoksidinės dervos kompozitų kai užpildo tūrinė koncentracija 5% kompleksinės dielektrinės skvarbos priklausomybė nuo temperatūros esant skirtingiems dažniams parodyta 4.3 paveiksle. Menama kompleksinės dielektrinės skvarbos dalis turi maksimumą, kurio padėtis priklauso nuo dažnio. Kai dažnis didėja, maksimumas išsiplečia ir pasislenka aukštesnių temperatūrų link. Dielektrinė skvarba mažėja didėjant dažniui. Tokią dielektrinę dispersiją lemia epoksidinės dervos molekulių dinamika[6]. Esant aukštai temperatūrai (aukštesnei negu 350 K), dėl elektrinio laidumo atsiradimo kompleksinis dielektrinė skvarba ir nuostolių tangentas $\varepsilon''/\varepsilon'$ staigiai padidėja.

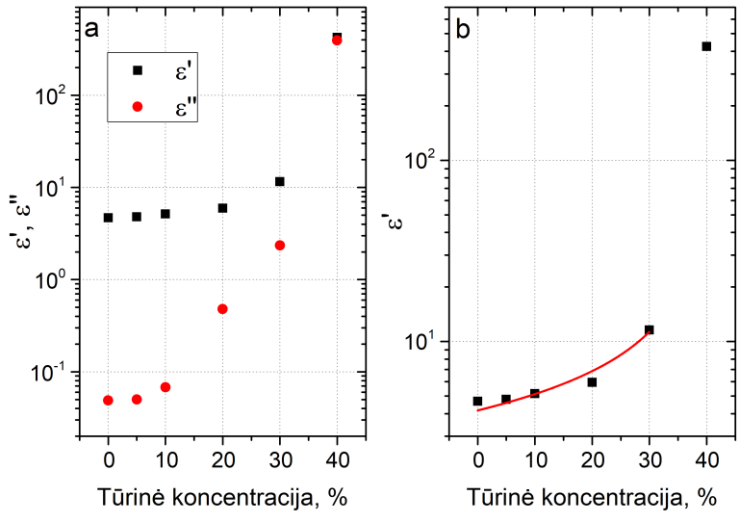

Pav. 4.2: (a) $Fe_2O_3 \cdot H_2O$/epoksidinių dervos kompozitų kompleksinies dielektrinės skvarbos priklausomybė nuo koncentracijos kambario temperatūroje ir esant 129 Hz dažniu; (b) $Fe_2O_3 \cdot H_2O$/epoksidinės dervos kompozitų dielektrinės skvarbos perkoliacijos dėsnis $\varepsilon' \propto (40 - p)^{-0.72}$.

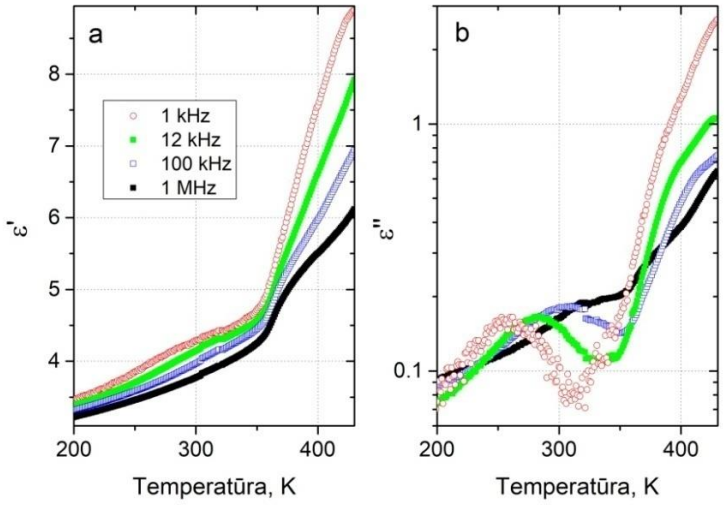

Pav. 4.3: $Fe_2O_3 \cdot H_2O$ nanostulpelių/epoksidinės dervos kompozitų kai užpildo tūrinė koncentracija 5% kompleksinės dielektrinės skvarbos priklausomybė nuo temperatūros esant skirtingiems dažniams.

$Fe_2O_3 \cdot H_2O$ nanostulpelių/epoksidinės dervos kompozitų kai užpildo tūrinė koncentracija 5% kompleksinės dielektrinės skvarbos priklausomybė nuo dažnio esant skirtingoms temperatūroms parodyta 4.4 paveiksle. Esant aukštesnei nei 25 °C temperatūrai, menamos kompleksinės dielektrinės skvarbos dalies spektrai turi maksimumus, atitinkantys absorbcijos smailę. Fizinis procesas, sąlygojantis absorbcijos smailę, yra dipolių persiorientavimas. Šis elgesys būdingas epoksidinės dervos kompozitams, esantiems žemiau perkoliacijos slenksčio[6].

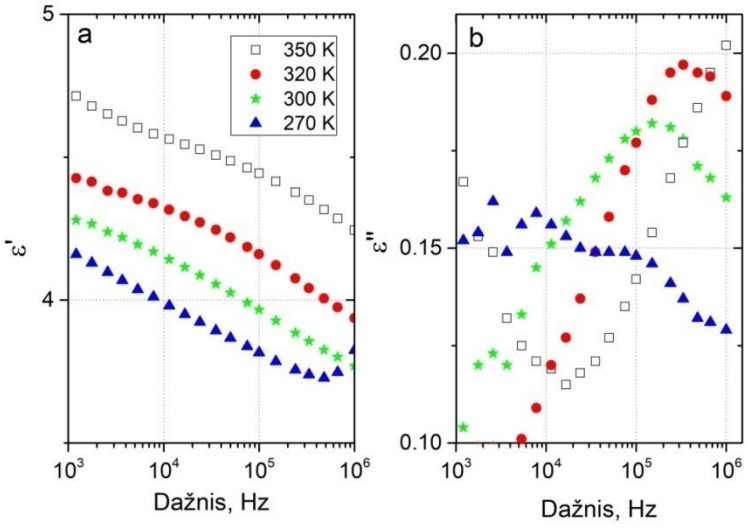

Pav. 4.4: $Fe_2O_3 \cdot H_2O$ nanostulpelių/epoksidinės dervos kompozitų, kai užpildo tūrinė koncentracija 5%, kompleksinės dielektrinės skvarbos priklausomybė nuo dažnio esant skirtingoms temperatūroms.

Aušinant maksimalus ε'' plečiasi ir slenka link žemų dažnių, o esant žemai temperatūrai (žemiau 270 K), jis išnyksta. Kompleksinė dielektrinės skvarbos menamos dalies maksimumo dažnis (ν_{max}) fiksuotoje temperatūroje leidžia nustatyti vidutinę relaksacijos trukmę naudojant šią lygtį: $\tau = 1/\nu_{max}$. Relaksacijos trukmė kinta pagal Vogel-Fulcher dėsnį[21] (žr. 4.5 pav.):

$$\tau = \tau_0 e^{\frac{E_B}{k_B(T-T_0)}} \quad (4.6)$$

kur τ_0 yra relaksacijos trukmė esant labai aukštai temperatūrai, E_B yra aktyvacijos energija, k_B yra Boltzmanno konstanta ir T_0 yra stiklėjimo temperatūra. Gauti parametrai pateikti 4.1 lentelėje. Kompozituose stiklėjimo temperatūra padidėja keičiant goetito nanostulpelių koncentraciją. Šį

padidėjimas yra sąlygotas stiprios sąveikos tarp goetito nanostulpelių ir epoksidinės dervos matricos. Be to, remiantis teoriniais skaičiavimais, kompozito tankis gali būti didesnis už gryno polimero tankį, todėl stiklėjimo temperatūros padidėjimas gali būti paaiškintas kompozito lokalių tankiu padidėjimu[6].

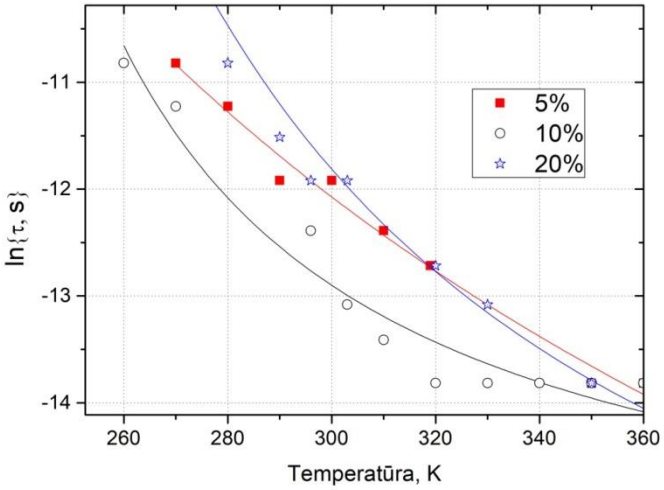

Pav. 4.5: $Fe_2O_3 \cdot H_2O$ nanostulpelių / epoksidinės dervos kompozitų vidutinės relaksacijos trukmės priklausomybė nuo temperatūros. Ištisinės linijos aproksimacijos Vogel-Fulcher dėsniu.

Lentelė 4.1: Fogelio-Vulcherio dėsnio aproksimacijos parametrai duomenims atvaizduotais Pav. 4.5.

Tūrinė koncentracija %	$\ln\{\tau_0, s\}$	E_B/k_B, K	T_0, K
0	-27.4	2689	142
5	-20	1649	91
10	-18	773	152
20	-18	805	180

Epoksidinės dervos kompozitų su įvairaus dydžio $MnFe_2O_4$ nanodalėmis dielektrinė skvarba yra pavaizduota Pav. 4.6. Dielektrinė skvarba didėja didėjant $MnFe_2O_4$ koncentracijai, o ypač staigus padidėjimas buvo pastebėtas ties 30% tūrinė koncentracija. Ši priklausomybė buvo aprašyta klasikiniu perkoliacijos dėsniu (Lygtis (4.1)). Apskaičiuoti parametrai pateikti 4.2 Lentelėje.

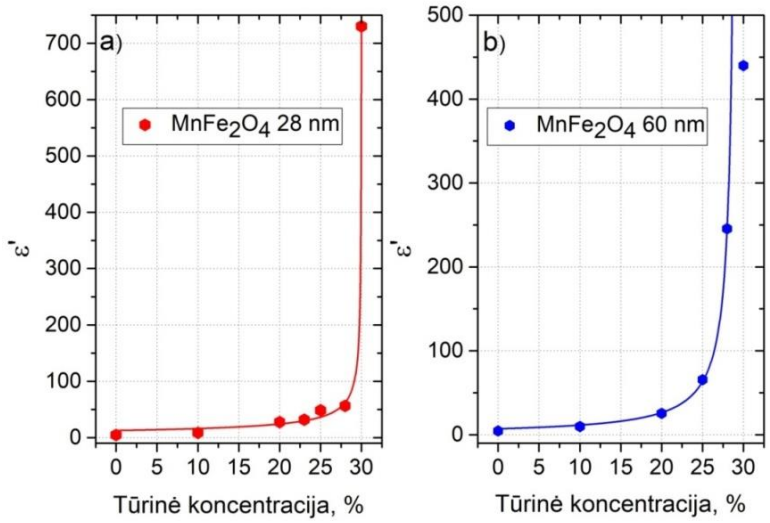

Pav. 4.6: $MnFe_2O_4$ epoksidinės dervos kompozitų dielektrinės skvarbos priklausomybė nuo užpildų koncentracijos dalelių dydis (a) 28 nm, (b) 60 nm.

Lentelė 4.2: Epoksidinių kompozitų su $MnFe_2O_4$ intarpais perkoliacijos dėsnio parametrai.

	p_c, vol.%	t
28 nm	30	0.58
60 nm	29.3	1.13

Perkoliacijos slenkstis praktiškai nepriklauso nuo $MnFe_2O_4$ nanodalelės dydžio ir yra artimas vertei nustatytai išstumtojo tūrio teorijoje[22].

Kompozitams, esantiems žemiau perkoliacijos slenksčio esant aukštai temperatūrai (virš 380 K), menama kompleksinės dielektrinies skvarbos dalis stipriai padidėja ir tampa didesnė už realios dielektrinės skvarbos dalį, o tai reiškia, kad kompozitas tapo laidžiu. Iš tiesų, esant aukštai temperatūrai

elektrinio laidumo priklausomybėje nuo dažnio stebima nuo dažnio nepriklausomą plokščią dalis, kuri atitinka nuolatinės srovės laidumą ir sritį, kur laidumas didėja didėjant dažniui aukštuose dažniuose (atitinka kintamosios srovės laidumą). Todėl elektrinį laidumą nuolatinei elektrinei srovei galima nustatyti iš laidumo spektrų (tai yra dažninių spektrų). Visų tirtų $MnFe_2O_4$/epoksidinės dervos kompozitų, kurių dalelių dydis 28 nm, nuolatinės srovės laidumo vertės parodytos 4.7 paveiksle.

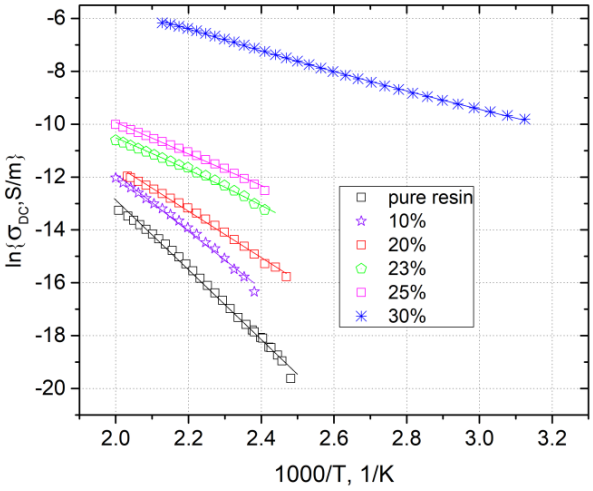

Pav. 4.7: Epoksidinės dervos kompozitų su $MnFe_2O_4$ nanodaleliemis (jų dydis 28 nm) laidumo nuolatinio elektros srovei priklausomybė nuo temperatūros.

Kompozitams esantiems žemiau perkoliacijos slenksčio (10–25% tūrinės koncentracijos) ir grynai epoksidinei dervai nuolatinės srovės laidumas stebimas tik aukštesnėje temperatūroje (virš 380 K). Tokią nuolatinės srovės laidumo elgseną lemia tai, kad epoksidinė derva tampa laidi aukštoje temperatūroje. Nuolatinės srovės laidumo temperatūrinė priklausomybė buvo aproksimuota pagal Areniuso dėsnį[23]:

$$\sigma_{DC} = \sigma_0 \exp\left(-\frac{E_A}{k_B T}\right) \tag{4.7}$$

čia σ_0 yra priešeksponentinis daugiklis, o E_A yra laidumo aktyvacijos energija. Gauti parametrai išvardyti 4.3 lentelėje. Kaip matyti, laidumo aktyvacijos energija mažėja, kai užpildų koncentracija mažėja. Kompozitams, viršijantiems perkoliacijos slenkstį (30% tūrinės koncentracijos), nuolatinės

srovės laidumas stebimas kambario temperatūroje, temperatūrai augant jo vertė didėja.

Panašus laidumo elgesys buvo pastebėtas ir visiems kitiems tirtiems $MnFe_2O_4$/epoksidinės dervos kompozitams, kurių dalelių dydis buvo 60 nm.

Lentelė 4.3: Areniuso dėsnio aproksimacijos parametrai elektrinio laidumo nuolatinei srovėi temperatūrinėms prikalusomybėms pavaizduotoms Pav. 4.7.

Tūrinė koncentracija%	σ_0, S/m	E_A/k_B, K
0	$0.7 \cdot 10^6$	13185
10	$0.2 \cdot 10^5$	10841
20	$0.4 \cdot 10^3$	8745
23	7.31	6247
25	7.30	5961
30	6.67	3791

Epoksidinė dervos su Ni@C nanodalelėmis dielektrinės savybės

Ni@C / epoksidinės dervos kompozitų dielektrinės skvarbos ir elektrinio laidumo priklausomybės nuo dažnio kambario temperatūroje pateiktos 4.8 paveiksle. Bandiniui, kurio Ni@C koncentracija yra mažiausia (10% tūrinės koncentracijos, tamsiai žalios spalvos užpildyti simboliai), dielektrinė skvarba silpnai priklauso nuo dažnio, o nuolatinės srovės laidumo plokščios dalies nėra (panašiai kaip tuščios epoksidinės dervos). Tuo tarpu kiti bandiniai demonstruoja elektrinį laidumą nuolatiniam elektriniam laukui ir stipria dielektrinės skvarbos priklausomybę nuo dažnio. Didėjant įterptų Ni@C nanodalelių koncentracijai, nuolatinės srovės laidumo absoliučioji vertė didėja. Toks rezultatas rodo, kad Ni@C / epoksidinės dervos kompozitų perkoliacijos slenkstis yra nuo 10% iki 15% tūrinės koncentracijos.

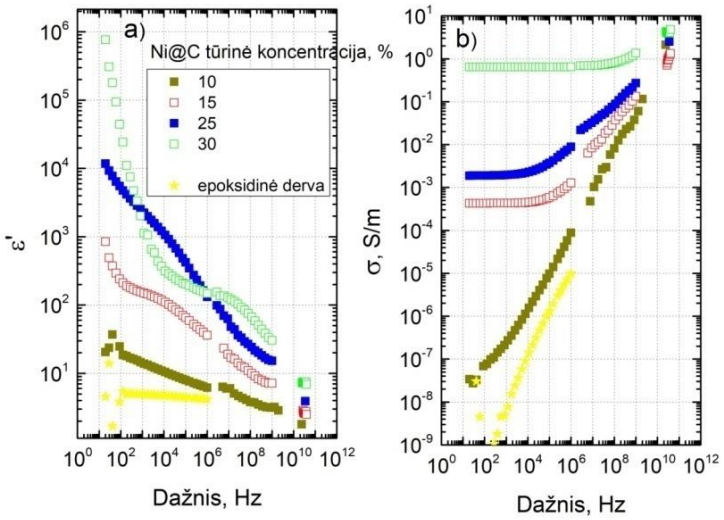

Pav. 4.8: Ni@C / epoksidinės dervos kompozitų dielektrinės skvarbos (a) ir elektrinio laidumo (b) dažnio priklausomybės kambario temperatūroje bei plačiame dažnių intervale.

Be to, kompozitams, virš perkoliacijos slenksčio, dielektrinė skvarba (ε') ir elektrinis laidumas (σ) yra pakankami dideli (ε'=10^5 ir σ=0.6 S/m esant 100 Hz, jei kompozitai turi 30% tūrinės koncentracijos Ni@C). Elektromagnetinių bangų dažniui didėjant dielektrinė skvarba mažėja, o elektrinis laidumas didėja. Tačiau kompleksinė dielektrinės skvarba išlieka gana didelė net mikrobangų dažnių diapazone, todėl šie kompozitai yra tinkami naudoti elektromagnetiniam ekranavimui.

Ni@C / epoksidinės dervos kompozitų laidumo nuolatinės srovėi priklausomybė nuo temperatūros plačiame temperatūros diapazone pateikiama 4.9 paveiksle. Kompozitui kuris yra žemiau perkoliacijos slenksčio (Ni@C dalelių tūrinė koncentracija yra 10%) elektrinis laidumas stebimas esant aukštesnioms temperatūroms (virš 400 K) dėl elektrinio laidumo epoksidinės dervos matricoje. Kompozitams kurie yra laidus kambario temperatūroje yra stebimas nedidelis nuolatinės srovės laidumo sumažejimas didėjant temperatūrai nuo žemiausių eksperimentiškai pasiekiamų verčių iki 310 K, šis sumažėjimas akivaizdžiai yra susietas su polimero matricos šilumine plėtra. Kaitinant kompozitus kitame temperatūrų intervale iki maksimalios temperatūros (500 K), monotoniškai padidėja nuolatinės srovės laidumo vertės (maždaug 10^2-10^3 karto), šis padidėjimas yra

sąlygotas epoksidinės dervos laidumo. Kaitinant kompozitus virš 450 K esant tam tikrom nanodalelių koncentracijoms yra stebimas staigus elektrinio laidumo padidėjimas arba sumažejimas, kuris yra susietas su perkoliacinio tinklo persitvarkymu ir naujo daugiau ar mažiau laidesnio perkoliacinio tinklo atsiradimo. Persiskirstymo efektai tampa dar labiau akivaizdus rezultatuose atitinkačiuose šaldymo ciklą: kompozitų elektrinis laidumas padidėja ir tampa nepriklausantis nuo temperatūros. Net gi kompozitui kuriam nebuvo stebima elektrinė perkoliacija iki kaitinimo (10% tūrinės koncentracijos) elektrinis laidumas nuolatinei srovėi buvo pastebėtas po kaitinimo-šaldymo ciklo. Šis efektas gali būti paaiškintas dalelių persiskirtymu atkaitinus kompozitą iki 500 K. Tai reiškia kad atkaitinimas virš 500 K gali būti veiksmingas būdas sumažinti perkoliacijos slenkstį nagrinėjamuose kompozituose. Mažiausias elektrinio laidumo padidėjimas po atkaitinimo stebimas kompozitams, kurių Ni@C koncentracija yra didžiausia, akivaizdžiai dėl mažiausių atstumų tarp laidžių klasterių ir stabiliausio pradinio perkoliacijos tinklo, susidariusio prieš terminį apdorojimą.

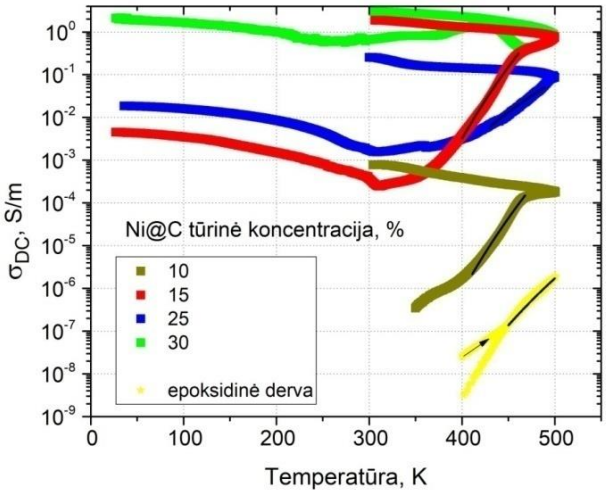

Pav. 4.9: Ni@C / epoksidinės dervos kompozitų laidumo nuolatinėi srovėi priklausomybė nuo temperatūros. Ištisinės linijos aukštoje temperatūroje atitinka Areniuso dėsnio aproksimaciją.

4.4 Hibridinių kompozitų dielektrinės savybės

$MnFe_2O_4$/DANV hibridinių kompozitų dielektrinės savybės

Epoksidinės dervos/DANV/$MnFe_2O_4$ hibridinių kompozitų elektrinio laidumo ir dielektrinės skvarbos priklausomybės nuo dažnio kambario temperatūroje yra pateiktos Pav. 4.10.

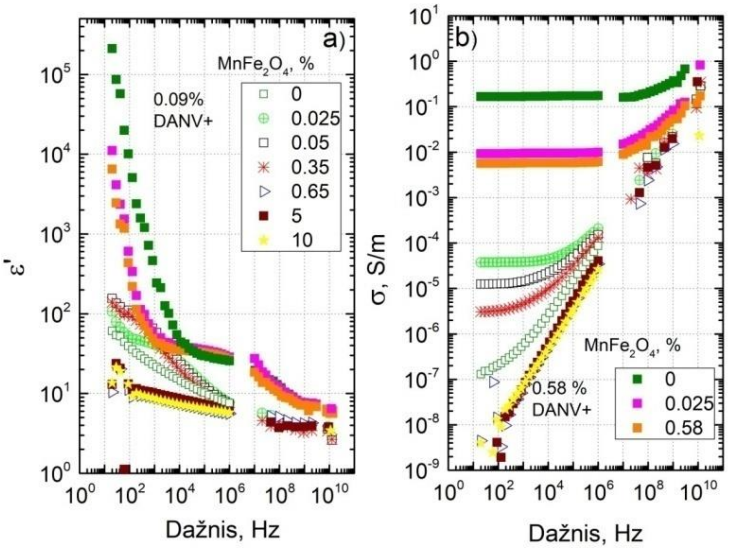

Pav. 4.10: Epoksidinies dervos / DANV / $MnFe_2O_4$ hibridinių kompozitų elektrinio laidumo ir dielektrinės skvarbos priklausomybės nuo dažnio kambario temperatūroje (nanodalelių koncentracija nurodyta tūrinė).

Esant žemiems dažniams (žemiau 1 MHz), kompozitų dielektrinė skvarba ir elektrinis laidumas stipriai priklauso nuo $MnFe_2O_4$ nanodalelių koncentracijos. Hibridiniuose kompozituose, kurių DANV tūrinė koncentracija yra 0.09%, pridėjus nedidelį kiekį $MnFe_2O_4$ (0.025% tūrinės koncentracijos) nelaidus kompozitas (atviri žalieji simboliai, 4.10 pav.), hibridinis kompozitas tampa laidžiu, o jo laidumo vertė padidėjo net 10^3 karto. Esant didesnėms $MnFe_2O_4$ tūrinėms koncentracijoms (0.05% ir 0.35%) kompozitų elektrinis laidumas yra mažesnis. O esant didžiausioms $MnFe_2O_4$ tūrinėms koncentracijoms (0.65%, 5% ir 10%) kompozitai yra visiškai nelaidūs nuolatinei srovei (laidumo spektruose nėra būdingojo plato), o laidumas kintamai elektrinei srovei yra daug mažesnės nei kompozitams be $MnFe_2O_4$ intarpų. Elektrinio laidumo maksimumas, stebimas esant 0.025%

$MnFe_2O_4$ tūrinei koncentracijai, buvo vizualiai išreikštas atsižvelgiant į atitinkamą koncentracinę priklausomybę kambario temperatūroje ir esant 129 Hz dažniui, kaip parodyta 4.11 paveiksle (dielektrinės skvarbos ir elektrinio laidumo rezultatai pateikiami prieš ir po atkaitinimo 500 K temperatūroje).

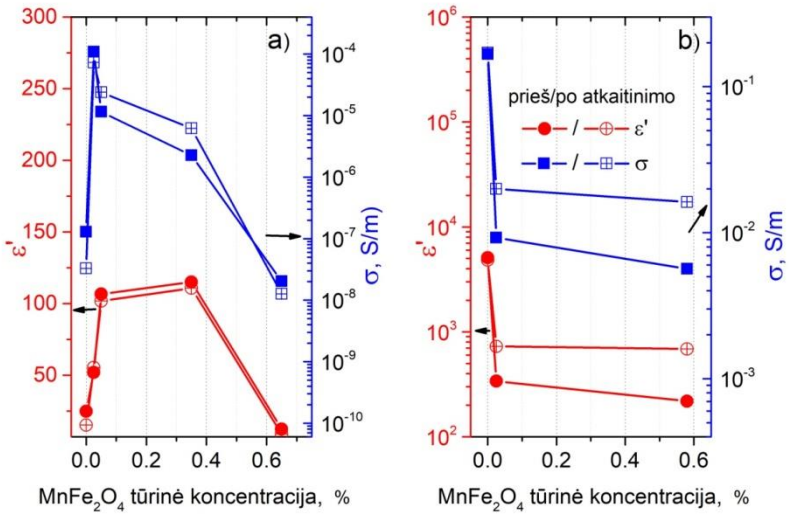

Pav. 4.11: Epoksidinės dervos DANV ir $MnFe_2O_4$ nanodalelių hibridinių kompozitų dielektrinės skvarbos ir elektrinio laidumo priklausomybė nuo užpildo koncentracijos, esant dažniui 129 Hz ir kambario temperatūrai, DANV tūrinė koncentacija (a) 0.09%, (b) 0.58%.

Taigi, šioje kompozitų serijoje su žemiau perkoliacijos esančios DANV koncentracijai galima pastebėti dviejų užpildų sinergijos efektą, kuris stebimas tik esant tam tikriems mažoms $MnFe_2O_4$ koncentracijoms. Šį rezultatą iš dalies galima paaiškinti analizuojant elektroninės mikroskopijos nuotraukas. Geriausias DANV pasiskirstymas buvo stebimas bandiniui, kurio $MnFe_2O_4$ koncentracija buvo mažiausia. Be to, tarp DANV ir $MnFe_2O_4$ klasterių gali vykti elektrinis transportas, ir šis mechanizmas turėtų lemti bendrą kompozito laidumo padidėjimą. Tačiau jo indėlis į bendrą laidumą akivaizdžiai yra daug mažesnis nei tunelinis laidumas tarp DANV klasterių.

Antrosios DANV serijos, kurios DANV tūrinė koncentracija yra pakankamai didelė – 0.58%, į pradinį laidųjį kompozitą pridėjus bet kokį nedidelį $MnFe_2O_4$ kiekį (iki 0.58% tūrinės koncentracijos) absoliučios elektrinio laidumo vertės tapo mažesnės (žr. 4.10b ir 4.11b pav.). Taigi, esant gerai suformuotam DANV perkoliacijos tinklui, bet koks magnetinių

$MnFe_2O_4$ dalelių kiekis lemia elektrinio laidumo sumažėjimą. Tai reiškia, kad šiai bandinių serijai sinergijos efektas nėra stebimas. Pastebėtas efektas gali būti paaiškinamas blogesniu DANV pasiskirstymu dėl $MnFe_2O_4$ nanodalelių pridėjimo.

Ni@C/DANV hibridinių kompozitų dielektrinės savybės

Siekiant pamatyti DANV makroskopinį pasiskirstymą, panoraminiai epoksidinės dervos / DANV /Ni@C hibridinių kompozitų SEM vaizdai pateikti 4.12 paveiksle (DANV klasteriai matomi kaip juodos dėmės, kurias patvirtina didesnės skiriamosios gebos SEM nuotraukos). DANV tinklas aiškiai pastebimas kompozituose, kuriuose yra 0.6% Ni@C (4.12b pav.), kompozituose, kuriuose 1% Ni@C tūriinės koncentracijos DANV klasteriai yra tolygiai pasiskirstę, o kompozituose be Ni@C nėra DANV makroskopinės struktūros. Tai gerai sutampa su aukščiau aptartais rezultatais, kad DANV klasteriai gali sumažinti perkoliacijos slenkstinę vertę[24]. Mažesni Ni@C klasteriai veikia kaip DANV klasterių separatoriai (4.12 pav.) ir palaiko tam tikrą makroskopinią DANV tinklo struktūrą (4.12b,c pav.).

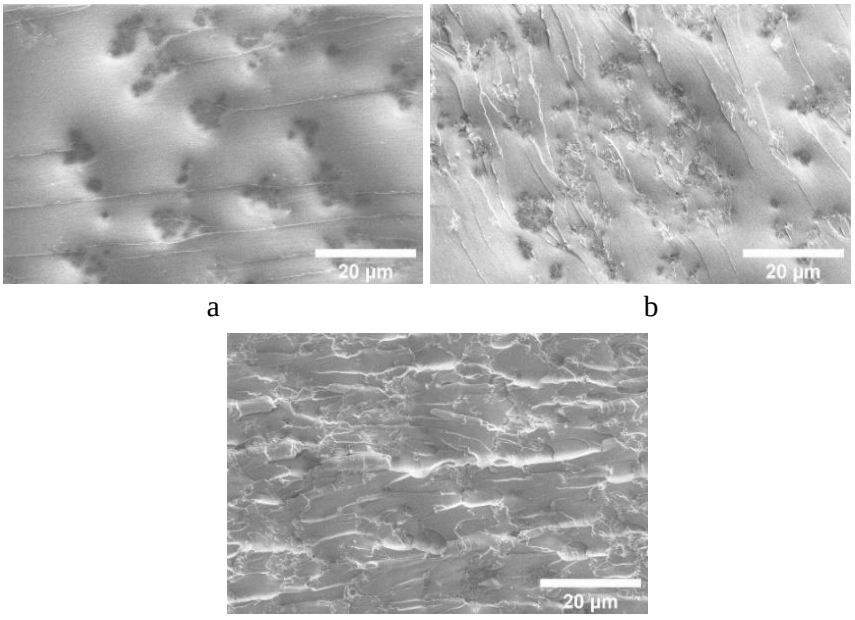

a b

c

Pav. 4.12: Epoksidinės dervos DANV ir Ni@C nanodalelių hibridinių kompozitų skenuojančio elektroninio mikroskopo (SEM) nuotraukos, (a) 0, (b) 0.6, ir (c) 1% Ni@C tūrinės koncentracijos.

Hybridinių DANV/Ni@C kompozitų dielektrinės skvarbos ir elektrinio laidumo dažninės ir koncentracinės (esant fiksuotam 129 Hz dažniui) priklausomybės kambario temperatūroje yra pavaizduotos atitinkamai 4.13 ir 4.14 paveiksluose. Ni@C pridėjimas į nelaidų kompozitą su DANV (kuris yra žemiau perkoliacijos slenksčio) sąlygoja elektrinio laidumo nuolatinėi srovėi atsiradimą. Nuolatinės srovės laidumas kinta nemonotoniškai, didėjant Ni@C nanodalelių koncentracijai. Pirma, σ_{DC} padidėja, tada, pasiekęs maksimalią vertę, kai Ni@C tūrinė koncentracija yra 0.2%, ji pradeda mažėti. Tai rodo sinergijos efektą tarp dviejų užpildų esant mažam Ni@C kiekiui. Galbūt nedideli Ni@C klasteriai, esantys tarp nanovamzdelių, padeda jiems užbaigti DANV perkoliacijos tinklo formavimąsi. Maži Ni@C kiekiai iki 0.2% tūrinės koncentracijos pagerina DANV dispersiją polimero matricoje, tuo tarpu esant didesnei Ni@C koncentracijai, padidėja aglomeratų skaičius ir dėl to pastebimas DANV pasiskirstymo pablogėjimas (žr. SEM vaizdus 4.12 paveiksle).

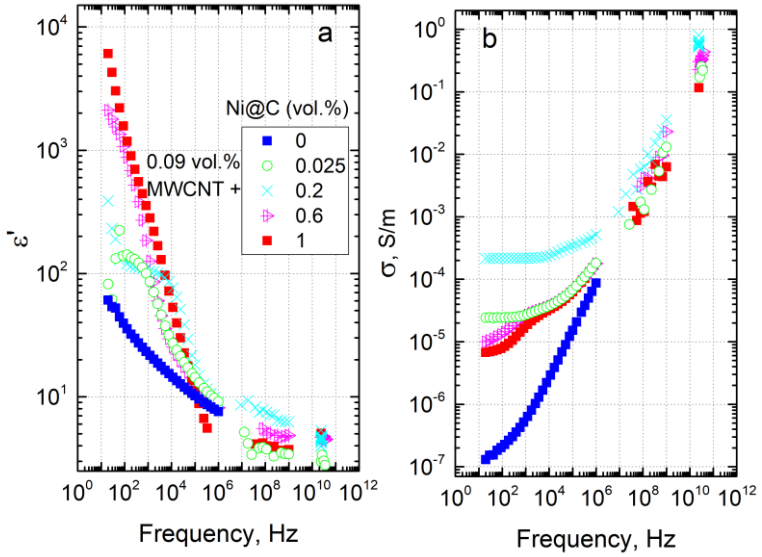

Pav. 4.13: Hibridinių DANV/Ni@C kompozitų dielektrinės skvarbos ir elektrinio laidumo dažninės priklausomybės kambario temperatūroje.

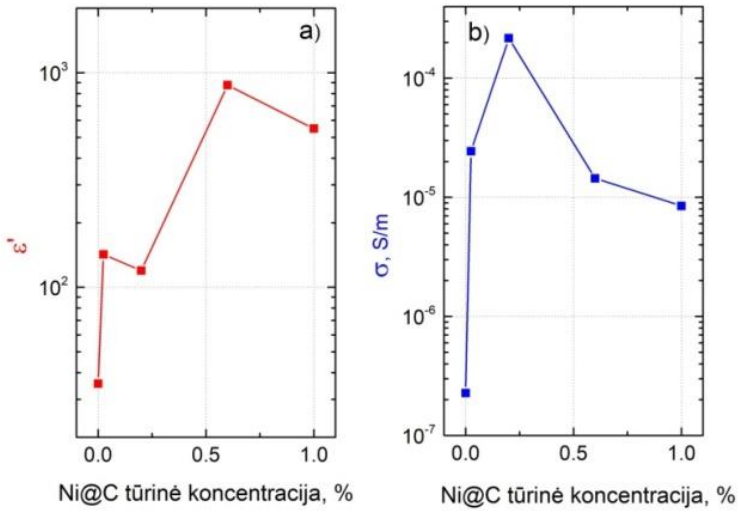

Pav. 4.14: Hibridinių DANV/Ni@C kompozitų dielektrinės skvarbos ir elektrinio laidumo koncentrancinės priklausomybės kambario temperatūroje.

4.5 Mikrobangių absorberių ir suderintų bangolaidinių apkrovų dizainas pritaikius medžiagas su elektriniais nuostoliais

Efektyvus elektromagnetinės spinduliuotės absorberiai yra labai svarbus daugeliui praktinių problemų, susijusių su elektromagnetiniu suderinamumu[25]. Bangolaidžio suderinta apkrova yra įprastas prietaiso pavyzdys, kuris sugeria elektromagnetinę energiją beveik neatspindėdamas krintančios elektromagnetinės bangos. Paprastai tokių komponentų dizainas yra pagrįstas ilgu pleištu arba piramide, įdėta į bangolaidžio centrą[26]. Pleištas pagamintas iš nuostolingos medžiagos (pvz., karbonilo geležies dalelių ir epoksidinės dervos kompozitas), o jo viršus orientuotas į krintančios bangos šaltinį. Anksčiau buvo parodyta optimalaus kompleksinės dielektrinės skvarbos (arba elektrinio laidumo diapazono keli S/m mikrobangų dažnių diapazone) vertė, norint efektyviai absorbuoti elektromagnetines bangas[19]. Nepaisant to, praktikoje dažnai sunku pasiekti optimalią dielektrinę skvarbą ir vienu metu kontroliuoti medžiagų nuostolius ir jų mechanines savybes. Turimų įprastų medžiagų nuostoliai dažnai yra mažesni už optimalias vertes,

todėl pleišto ilgis padidėja, kad būtų pasiektas būtinas elektromagnetinio susilpninimo lygis.

Periodinės piramidinės struktūros yra naudojamos kaip plačiajuosčio ryšio absorbentai beaidėms kameroms[27]. Viskadourakis ir kt. tyrė be nuostolių piramidinės struktūros ekranavimo efektyvumą 3.5–7 GHz dažnių diapazone[28], Nornikmanas ir kt. - šešiakampes piramides 1–20 GHz dažnių diapazone[29], piramidines struktūras pritaikė kaip anteną 3.3–8.0 GHz dažnių diapazone[30]. Tačiau visi minėti komponentai buvo pagaminti iš nelaidžių polimerų. Kuriant piramidines struktūras, pagrįstas nuostolingomis medžiagomis, atsiveria naujos galimybės elektromagnetinių trukdžių (ETI) ekranavimo srityje. Visų pirma, šie sprendimai leidžia miniatiūrizuoti mikrobangų komponentus, tokius kaip absorberiai ir apkrovos. Pigi ir laiko taupanti galimybė gaminti sudėtingos formos įtaisus ir konstrukcijas yra 3D spausdinimas. Bus parodyta, kad vidutinio elektros laidumo nuolatinės srovės laidumo gija (t. y. ≃ 1 S/m) yra universalus mikrobangų slopinimo elementų, suprojektuotų 3D spausdinant, vidurkis.

Šis skyrius skirtas periodinių piramidinių konstrukcijų, pagrįstų nuostolingomis medžiagomis, kaip ekranavimo komponentų ir suderintų apkrovų projektavimo, taikymo pranašumams tirti. Bus pateiktas skaitinis elektromagnetinių savybių modeliavimo metodas ir optimalus geometrinių parametrų įvertinimas. Metodo efektyvumas bus patikrintas eksperimentiškai tiriant 3D spausdintų nanoanglies pagrindu pagamintų nuostolingų piramidinių struktūrų ekranavimo efektyvumą 12–18 GHz (Ku-juostos) ir 26–37 GHz (Ka-juostos) dažnių diapazonuose.

Piramidinių struktūrų elektromagnetinių savybių simuliacijos

Klasikinis suderinto apkrovos darbo principas grindžiamas suglotnintu perėjimu iš tuščio bangolaidžio į bangolaidį, užpildytą nuostolinga medžiaga. Paprastai nuostolingas regionas yra padarytas ilgo pleišto ar piramidės pavidalu ir dedamas į bangolaidžio centrą, kuris viršuje orientuotas į krintančią elektromagnetinę bangą (4.15 pav. (Įterpimas)). Piramidės pagrindo koordinatė priskiriama (x=0), dh yra piramidės aukštis, h_0 yra padėklo (piramidės pagrindo) storis. Atlikus homogenizavimo procedūrą, efektyviojo lūžio rodiklio n priklausomybė nuo piramidinės struktūros koordinatės x yra tokia:

$$n(x) = n_p\big(1 - S(x)\big) + n_0 S(x) \tag{4.8}$$

kur

$$S(x) = \begin{cases} 1, & x < -(h_0 + dh) \\ 1 - \left(\frac{h_0 + dh + x}{dh}\right)^2, & -(h_0 + dh) < x < -h_0 \\ 0, & -h_0 < x < 0 \\ 1, & x > 0 \end{cases} \quad (4.9)$$

ir n_p yra lūžio rodiklis medžiagos iš kurios padaryta piramidė, n_0 oro lūžio rodiklis. Erdvinis lūžio rodiklio pasiskirstymas atitinkantis lygtį (4.8) yra pavaizduotas Pav. 4.15.

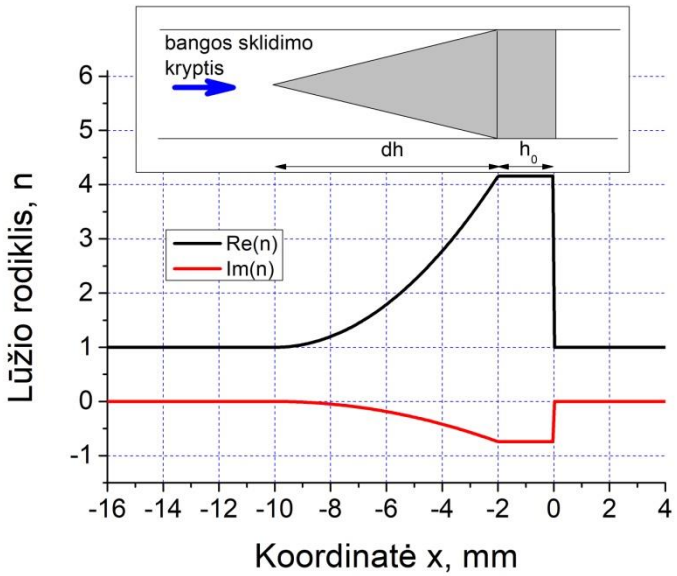

Pav. 4.15: Erdvinis lūžio rodiklio pasiskirstymas piramidinėje struktūroje atlikus homogenizacijos procedūrą (viduje: piramidės patalpintos bangolaidyje vaizdas iš šono).

Santykinė amplitudė atspindėto signalo S_{11} ir praėjusio S_{21} per piramidė galima lengvai apskaičiuoti panaudojus daugiasluoksnį metodą išvystytą Lygtys (4.3)-(4.4). Slopinimas SE yra apibrėžiamas taip $SE_T = -20log_{10}S_{21}$. Panašiai slopinimas dėl atspindžio apibrėžiamas kaip $SE_R = -20log_{10}S_{11}$.

Naudotos 3D spausdinimo gijos kompleksinės dielektrinės skvarbos ir lūžio rodiklio (tai yra polilaktido matricos kompozitas su 12% DANV masinės koncentracijos) priklausomybės nuo dažnio, perskaičiuotų iš eksperimentiškai išmatuotų spausdinto lygiagretaus sluoksnio S-parametrų[31], pateikti 4.16 paveiksle. Kaitinimo siūlas turi didelių nuostolių tangentą (ne mažiau

kaip 0.4 visame dažnių diapazone). Be to, medžiaga turi dielektrinę dispersiją, jos dielektrinė skvarba mažėja didėjant dažniui. Tokia dielektrinė dispersija yra būdinga DANV kompozitams, kurių užpildų kiekis viršija perkoliacijos slenkstį, mikrobangų dažnio diapazone[6].

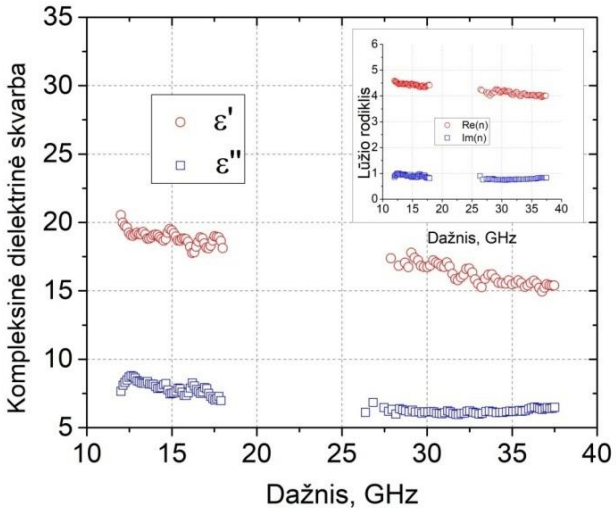

Pav. 4.16: Spausdintos medžiagos kompleksinės dielektrinės skvarbos ir kompleksinio lūžio rodiklio dažnio priklausomybės Ku- ir Ka-dažnių diapazone.

Mažiausias piramidžių aukštis ir padėklo storis buvo apskaičiuoti naudojant siūlomą modelio lygtis (4.8)-(4.9). Buvo padaryti keli supaprastinimai. Dažnis buvo parinktas 30 GHz, efektyvieji ekranavimo kriterijai buvo parinkti taip SE_T>20 dB ir SE_R>20 dB (tai atitinka daugiau nei 99% krintančios bangos galios absorbciją).

Skaičiuojant dh, padėklo aukštis buvo h_0=2 mm. Šiuo atveju piramidės elektromagnetinis slopinimas priklauso tik nuo jos aukščio ir panaudotos medžiagos dielektrinies skvarbos. Tada dh ir ε deriniai, atitinkantys minėtus elektromagnetinio slopinimo kriterijus, pateikiami kaip regionai $\varepsilon''(\varepsilon')$ koordinatėmis 4.17 paveiksle. dh sumažėjimas lemia galimų ε derinių srities susiaurėjimą. Išmatuotas kaitinimo siūlelio kompleksinė dielektrinė skvarba esant 30 GHz dažniui yra ε=16.74−i6.17 (4.16 pav.). Mažiausias piramidės aukštis dh, reikalingas efektyviam ekranavimui, yra 8–9 mm Ka juostai. Panašiai buvo įvertintas Ku-juostos dh=22 mm.

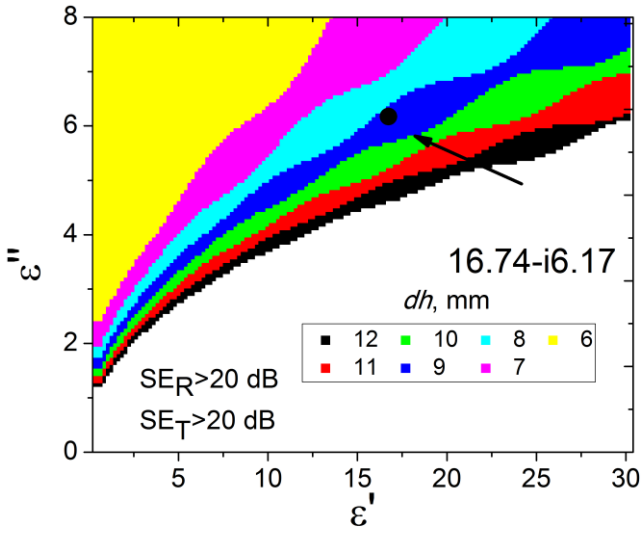

Pav. 4.17: Piramidės aukštis reikalingas efektyviam elektromagnetinių bangų slopinimui (20 dB) kaip kompleksinės dielektrinės skvarbos funkcija.

Pagrindo storio h_0 skaičiavimams naudotas gautas dh=8 mm. Priklausomybės SE_T ir SE_R nuo pagrindo storio h_0 pateiktos 4.18 paveiksle (užpildyti simboliai). SE_R svyravimai, susiję su trukdžiais, o SE_T didėja monotoniškai. Šie svyravimai gali būti eliminuoti padidinus piramidžių aukštį dh. Lygiagrečiojo sluoksnio (dh=0 mm) SE ir h_0 taip pat pateikti 4.18 paveiksle (žr. atvirus simbolius). Tiek plokštumos sluoksnio SE_R tiek SE_T yra žymiai mažesni, palyginti su piramidine struktūra. Tikimasi, kad SE_T didės kartu su storiu, tačiau SE_R išlieka mažesnis nei 5 dB. Tai reiškia, kad plokščiasis sluoksnis negali vienu metu pademonstruoti didelių SE_T ir SE_R parametrų verčių (arba, kitaip tariant, absorbcijos gebos) esant bet kokiam pagrindo storiui.

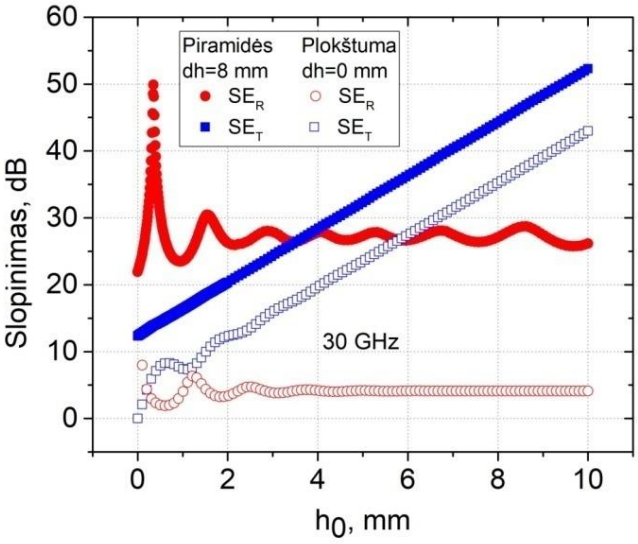

Pav. 4.18: SE_T ir SE_R parametrų priklausomybės nuo padėklo storio.

Siūlomas laipsniškai kintančio lūžio rodiklio metodas yra naudingas praktiškai projektuojant piramidines suderintas apkrovas. Jame pateikiami minimalūs geometriniai parametrai, reikalingi efektyviam elektromagnetiniam slopinimui, atsižvelgiant į naudojamos medžiagos dielektrines savybes. Tam tikru kaitinamojo siūlo laidumo atveju h_0=2 mm, dh=8–9 mm (Ka-dažnių diapazonas) ir dh=22 mm (Ku-dažnių diapazonas) deriniai yra minimalūs parametrai, leidžiantys pasiekti 20 dB lygį tiek SE_T, tiek SE_R lygius.

Mikrobangiai matavimai

Atspausdinti piramidiniai mėginiai ir eksperimentiškai išmatuoti Ku- ir Ka-dažnių diapazonų ekranavimo efektyvumas pateikti atitinkamai 4.19 ir 4.20 paveiksluose. Abi Ku- ir Ka- dažnių diapazonų struktūros, nepaisant kai kurių spausdinimo problemų, rodo aukštą SE_T>20 dB ir SE_R>20 dB lygį ir gali būti naudojamos kaip efektyvios suderintos apkrovos arba absorberiai beaidėse kamerose. Medžiagų su nuostoliais, kai yra didelė kompleksinė skvarba, naudojimas leidžia pasiekti panašų ekranavimo efektyvumą su mažesnėmis piramidėmis (žr. 4.4 lentelę). Dar daugiau, priešingai nei literatūroje vardinami rezultatai[29,32-36], 4.20 paveiksle parodyta, kad tiek

perduodami, tiek atspindėti signalai yra gerai susilpninti. Tai įmanoma dėl didelių ominių nuostolių medžiagų masėje ir bangų, išsisklaidančių dėl bandinio geometrijos, derinio. Svarbu pažymėti, kad dideli ominiai nuostoliai nagrinėjamose medžiagose buvo pasiekti dėl polimerų matricoje susidariusio nuolatinės srovės laidumo DANV pagrindu sukurto tinklo. Dėl depoliarizacijos poveikio DANV aglomeratai, esantys žemiau perkoliacija esančiame kompozite, silpnai sąveikauja su mikrobangų spinduliuote. Nepaisant to, aglomeratai įtraukiami į nuolatinės srovės laidumo kompozito perkoliacinį tinklą (kuris tiksliai atitinka mūsų eksperimentinę situaciją), jie prisideda prie efektyvaus elektromagnetinių bangų sklaidos ir silpninimo.

Lentelė 4.4: Piramidinių struktūrų elektromagnetinio slopinimo palyginimas.

Medžiagos parametrai	dh, mm	h_0, mm	SE_R, dB	SE_T, dB	Dažnis, GHz	Nuorodos
ε=2, tanδ=0.2	90	25	45	n/a	10	[32]
ε=2.492, tanδ=0.956	130	20	42.93	n/a	10-15	[29]heksagoninė
ε=2.9, tanδ=0.084	130	n/a	43.294	n/a	10-15	[33]trigoninė
BlackMagic 3D	2	2	12	n/a	5.5	[34]
VeroBlack	80	20	20	n/a	100	[35]
ε=1.5, tanδ=0.26	40	20	40	n/a	30	[36]
ε=18.66, tanδ=0.38	22	2	40.15	28.09	17.4	Šis darbas
ε=15.55, tanδ=0.39	8	2	23.88	39.17	35.7	Šis darbas

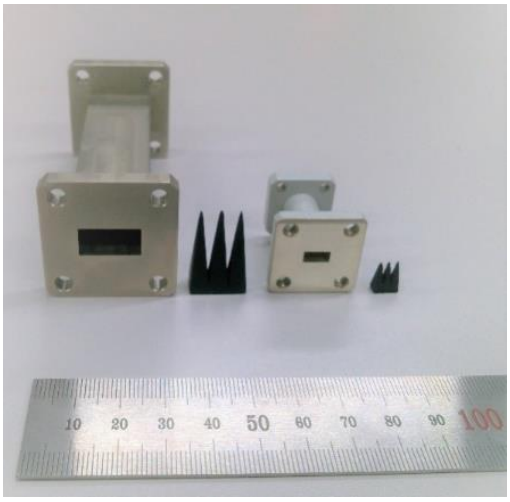

Pav. 4.19: 3D spausdintos piramidės ir bangolaidinės sistėmos kairėje Ku dažnių diapazone, dešinėje Ka dažnių diapazone.

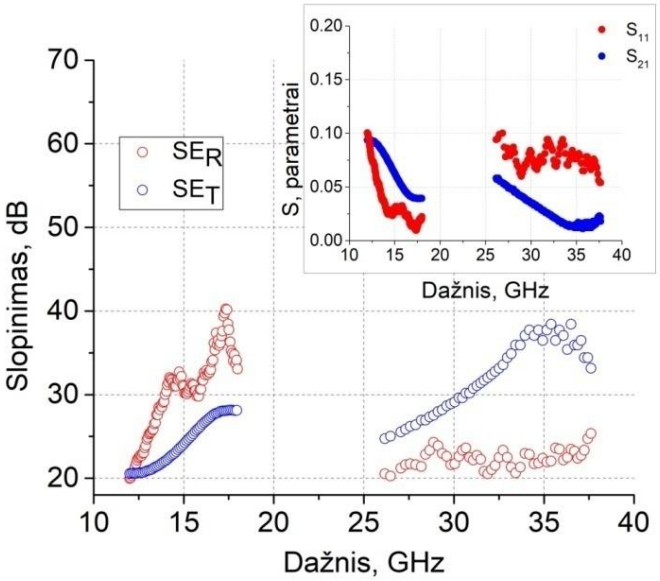

Pav. 4.20: Slopinimo ir S parametrai (viduje) 3D spausdintos piramidės Ku ir Ka dažnių diapazone.

Mikrobangų elektromagnetinio slopinimo modeliavimas

Pagal aukščiau pateiktą ir sėkmingai pritaikytą modelį, atsižvelgiant į medžiagų savybes (kompleksinę dielektrinę skvarbą arba kompleksinį lūžio rodiklį), reikiamą dažnių diapazoną ir pagrindo storį, galima įvertinti piramidinių struktūrų ekranavimo efektyvumą iki eksperimento.

Tarp epoksidinių kompozitų su magnetinėmis nanodalelėmis, ištirtų aukščiau, Ni@C sistemai kompleksinė dielektrinė skvarba išlieka gana didelė net mikrobangų dažnių diapazone. Tai reiškia, kad šie kompozitai yra tinkami elektromagnetiniam ekranavimui dėl didelių dielektrinių/magnetinių nuostolių. Konstruojant piramidines struktūras, pagrįstas Ni@C kompozitais, absorbcijos gebėjimą galima žymiai pagerinti, o optimizavimo modelis gali padėti numatyti šias savybes. 4.5 lentelėje pateikiamos piramidinių struktūrų, pagamintų iš Ni@C kompozito, kurio pagrindo storis h_0=2 mm, ir skirtingų piramidės aukščių dh (nuo 8 iki 15 mm), bangolaidyje, esant 30 GHz, absorbcijos gebėjimų prognozės.

Lentelė 4.5: Piramidinių struktūrų, pagamintų iš Ni@C kompozito, kurio pagrindo storis h_0=2 mm ir skirtingi piramidės aukščiai dh, absorbcijos (%) prognozavimas bangolaidyje esant 30 GHz dažniui.

Tūrine koncentracija	dh, mm								
	0	8	9	10	11	12	13	14	15
15 % Ni@C	29.0	71.9	74.9	77.1	78.8	80.6	82.4	84.1	85.5
25 % Ni@C	44.0	89.6	90.7	92.1	93.6	94.6	95.3	95.9	96.5
30% Ni@C	62.0	95.6	96.0	96.5	97.5	98.0	98.3	98.6	99.0

4.6 Išvados

1. $Fe_2O_3 \cdot H_2O$ nanostulpelių / epoksidinės dervos kompozitų dielektrinės savybės buvo tiriamos plačiame dažnių diapazone nuo hercų iki terahercų 200–450 K temperatūroje. Šioje sistemoje perkoliacijos slenkstis yra arti 40% tūrinės koncentracijos.
2. $MnFe_2O_4$ ir epoksidinės dervos kompozitų, turinčių dviejų skirtingų dydžių sferinės formos nanodalelės (28 ir 60 nm), dielektrinės savybės buvo ištirtos dažnių diapazone nuo 20 Hz iki 1 MHz ir temperatūros diapazone nuo 150 iki 500 K. Parodyta, kad kompozitų su mažomis ir didelėmis $MnFe_2O_4$ nanodalelėlimis perkoliacijos slenksčiai yra 30% ir 29.3% tūrinės koncentracijos, atitnkamai. Nedidelis perkoliacijos slenksčio vertės skirtumas yra susijęs su geresniu didesnių nanodalelių pasiskirstymu.
3. Pastebėti keli bendri $Fe_2O_3 \cdot H_2O$ / epoksidinės ir $MnFe_2O_4$ / epoksidinės sistemos bruožai:
   - Kompozitų dielektrinį elgesį žemiau perkoliacijos slenksčio daugiausia lemia relaksacija grynoje polimero matricoje. Kompozitų virš perkoliacijos slenksčio dielektrinės savybės lemia perkoliacinis tinklas, kurį sudaro kompozito viduje esančios nanodalelės.
   - Nuolatinės srovės laidumas žemuose dažniuose stebimas dėl atsitiktiniu būdu pasiskirsčiųsių elektrinių krūvių ir didėja didėjant užpildo koncentracijai. Esant pakankamai aukštai temperatūrai, dėl baigtinio epoksidinės dervos laidumo, nuolatinės srovės laidumas kompozituose atsiranda tiek virš, tiek žemiau perkoliacijos slenksčio. Aktyvacijos energija mažėja, kai užpildų

koncentracija didėja, tai rodo, kad elektrinis transportas vyksta bendrai užpildų ir epoksidinės matricos posistemiuose.

4. Ištirtos Ni@C / epoksidinės dervos kompozitų dielektrinės ir elektrinės savybės plačiame dažnių (20 Hz – 40 GHz) ir temperatūros (30–500 K) intervaluose. Šios sistemos perkoliacijos slenkstis yra tarp 10% ir 15% tūrinės koncentracijos. Papildomas šių kompozitų atkaitinimas iki 500 K žymiai sumažina perkoliacijos slenkstį, žemiau negu 10% tūrinės koncentracijos. Tačiau padidėjus Ni@C koncentracijai, nanodalelių dispersijos kokybė polimere smarkiai blogėja. Tai įrodo SEM nuotraukos ir relaksacijos trukmių pasiskirstymų analizė.
5. Ni@C / epoksidinės dervos kompozitai smarkiai slopina mikrobangų dažnių diapazono elektromagnetinę spinduliuotę, pavyzdžiui, 2 mm storio didžiausios koncentracijos bandinys (30% tūrinės koncentracijos Ni@C) praleidžia tik 17% krentančios bangos galios.
6. Hybridinių epoksidinės dervos / DANV / $MnFe_2O_4$ ir epoksidinės dervos /DANV/ Ni@C kompozitai demonstruoja ryškų sinergijos efektą, kai DANV koncentracija yra šiek tiek žemesnė nei perkoliacijos slenkstis (atitinkamuose kompozituose su vienos rūšies užpildu) ir kai antrojo magnetinio užpildo koncentracija yra nedidelė (palyginama su DANV koncentracija). Epoksidinės dervos / DANV /$MnFe_2O_4$ hybridinių kompozitų elektrinio laidumas maksimumas stebimas arti 0.025% tūrinės mangano ferito koncentracijos, jo vertė yra apie 10^3 didesnė negu laidumas kompozitų be $MnFe_2O_4$ intarpų. Epoksidinės dervos / DANV / Ni@C kompozitų elektrinis laidumas yra didžiausias esant 0.2% Ni@C tūrinei koncentracijai, o laidumo vertė šiam kompozitui yra bent 10^3 didesnė negu kompozitų turinčių tik DANV.
7. Kompozitams, kurių DANV koncentracija viršija perkoliacijos slenkstį sinergijos efekto nepastebėta jokiam $MnFe_2O_4$ kiekiui.
8. Sinergijos efektų atsiradimas polimerų kompozitų elektrinėse savybėse yra stipriai susijęs su palankiu nanodalelių pasiskirstymu polimero matricoje. Dielektrinės relaksacijos spektroskopijos procesai daugiafaziuose kompozituose, esant tam tikrai fiksuotai laidaus funkcinio užpildo koncentracijai ir skirtingai papildomo užpildo koncentraciaji, gali padėti optimizuoti užpildų pasiskirstymą sinergijai pasiekti.
9. Buvo apsvarstyta periodinė piramidinė struktūra, pagrįsta laidžia nuostolinga medžiaga, kaip efektyvus mikrobangų absorberis ir

kompaktiška suderinta apkrova. Piramidės geometrijos parametrai buvo gauti optimizuojant ekranavimo efektyvumą, palyginti su medžiagos kompleksinėmis dielektrinėmis savybėmis. 3D spausdintos piramidinės struktūros su apskaičiuotais parametrais buvo eksperimentiškai išbandytos mikrobangų dažnių diapazonuose, ir jos parodė, kad tiek atspindėtų, tiek perduodamų signalų elektromagnetinis slopinimas viršija 20 dB. Sukurta piramidės parametrų vertinimo technika gali būti veiksmingai naudojama prieš eksperimentą, nes joje atsižvelgiama į medžiagos kompleksines dielektrines savybes, reikiamą dažnių diapazoną ir piramidės dydžius.

4.7 Nuorodos

1. Komarneni S. Feature article. Nanocomposites. *J Mater Chem*. 1992;2:1219-1230.
2. Fu S-Y, Feng X-Q, Lauke B, Mai Y-W. Effects of particle size, particle/matrix interface adhesion and particle loading on mechanical properties of particulate–polymer composites. *Compos Part B Eng*. 2008;39(6):933-961. doi:10.1016/j.compositesb.2008.01.002
3. Macutkevic J, Kuzhir P, Paddubskaya A, et al. Epoxy Resin/Carbon Black Composites Below the Percolation Threshold. *J Nanosci Nanotechnol*. 2013;13(8):5434-5439. doi:10.1166/jnn.2013.7547
4. Deng H, Skipa T, Bilotti E, et al. Preparation of High-Performance Conductive Polymer Fibers through Morphological Control of Networks Formed by Nanofillers. *Adv Funct Mater*. 2010;20(9):1424-1432. doi:10.1002/adfm.200902207
5. Inzelt G. *Conducting Polymers: A New Era in Electrochemistry*. Springer; 2008.
6. Qin F, Brosseau C. A review and analysis of microwave absorption in polymer composites filled with carbonaceous particles. *J Appl Phys*. 2012;111(6):061301. doi:10.1063/1.3688435
7. Ahmed SR, Ogale SB, Papaefthymiou GC, Ramesh R, Kofinas P. Magnetic properties of CoFe2O4 nanoparticles synthesized through a block copolymer nanoreactor route. *Appl Phys Lett*. 2002;80(9):1616-1618. doi:10.1063/1.1456258

8. Hu H, Zhao L, Liu J, et al. Enhanced dispersion of carbon nanotube in silicone rubber assisted by graphene. *Polymer*. 2012;53(15):3378-3385. doi:10.1016/j.polymer.2012.05.039
9. Chen J, Du X-C, Zhang W-B, et al. Synergistic effect of carbon nanotubes and carbon black on electrical conductivity of PA6/ABS blend. *Compos Sci Technol*. 2013;81:1-8. doi:10.1016/j.compscitech.2013.03.014
10. Stankovich S, Dikin DA, Dommett GHB, et al. Graphene-based composite materials. *Nature*. 2006;442(7100):282-286. doi:10.1038/nature04969
11. Han Z, Fina A. Thermal conductivity of carbon nanotubes and their polymer nanocomposites: A review. *Prog Polym Sci*. 2011;36(7):914-944. doi:10.1016/j.progpolymsci.2010.11.004
12. Moniruzzaman M, Winey KI. Polymer Nanocomposites Containing Carbon Nanotubes. *Macromolecules*. 2006;39(16):5194-5205. doi:10.1021/ma060733p
13. Stauffer D, Aharony A. *Introduction To Percolation Theory Revised Second Edition*. Taylor and Francis; 2014.
14. Liu J, Duan C-G, Yin W-G, Mei WN, Smith RW, Hardy JR. Large dielectric constant and Maxwell-Wagner relaxation in Bi2⁄3Cu3Ti4O12. *Phys Rev B*. 2004;70(14):144106. doi:10.1103/PhysRevB.70.144106
15. Macutkevic J, Banys J, Matulis A. Determination of the Distribution of the Relaxation Times from Dielectric Spectra. *Nonlinear Anal Model Control*. 2004;9(1):75-88. doi:10.15388/NA.2004.9.1.15172
16. Born M, Wolf E. *Principles of Optics: Electromagnetic Theory of Propagation, Interference and Diffraction of Light*. 6th ed. Pergamon Press; 1980.
17. Grigas. Microwave dielectric spectroscopy of ferroelectrics and related materials. CRC PRESS; 2020.
18. Bellucci S, Coderoni L, Micciulla F, Rinaldi G, Sacco I. Mechanical and Electrical Characterization of Polymer Nanocomposites with Carbon Nanotubes. *Nanosci Nanotechnol Lett*. 2011;3(6):826-834. doi:10.1166/nnl.2011.1248
19. Bychanok D, Gorokhov G, Meisak D, et al. Design of Carbon Nanotube-Based Broadband Radar Absorber for Ka-Band Frequency Range. *Prog Electromagn Res M*. 2017;53:9-16. doi:10.2528/PIERM16090303

20. Kirkpatrick S. Percolation Phenomena in Higher Dimensions: Approach to the Mean-Field Limit. *Phys Rev Lett*. 1976;36(2):69-72. doi:10.1103/PhysRevLett.36.69
21. Fulcher GS. Analysis of recent measurements of the viscosity of glasses. *J Am Ceram Soc*. 1925;8(6):339-355. doi:10.1111/j.1151-2916.1925.tb16731.x
22. Kirkpatrick S. Percolation and Conduction. *Rev Mod Phys*. 1973;45(4):574-588. doi:10.1103/RevModPhys.45.574
23. Laidler KJ. The development of the Arrhenius equation. *J Chem Educ*. 1984;61(6):494. doi:10.1021/ed061p494
24. Bertasius P, Meisak D, Macutkevic J, et al. Fine Tuning of Electrical Transport and Dielectric Properties of Epoxy/Carbon Nanotubes Composites via Magnesium Oxide Additives. *Polymers*. 2019;11(12):2044. doi:10.3390/polym11122044
25. Mirzaee M, Noghanian S, Chang I. Low-profile bowtie antenna with 3D printed substrate. *Microw Opt Technol Lett*. 2017;59(3):706-710. doi:10.1002/mop.30379
26. Pozar DM. *Microwave Engineering*. 4th ed. Wiley; 2012.
27. Hindman GE, Newell AC. Reflection suppression to improve anechoic chamber performance. *AMTA Eur*. Published online 2006:297-302.
28. Viskadourakis Z, Vasilopoulos KC, Economou EN, Soukoulis CM, Kenanakis G. Electromagnetic shielding effectiveness of 3D printed polymer composites. *Appl Phys A*. 2017;123(12):736. doi:10.1007/s00339-017-1353-z
29. Nornikman H, Malek F, Soh PJ, Azremi AAH. Reflection loss performance of hexagonal base pyramid microwave absorber using different agricultural waste material. In: *2010 Loughborough Antennas & Propagation Conference*. IEEE; 2010:313-316. doi:10.1109/LAPC.2010.5666029
30. Jenks CHJ. Dielectric pyramid antenna for GPR applications. In: *2016 10th European Conference on Antennas and Propagation (EuCAP)*. IEEE; 2016:1-3. doi:10.1109/EuCAP.2016.7481679
31. Chung B-K. Dielectric constant measurement for thin materials at microwave frequencies. *Prog Electromagn Res*. 2007;75:239-252. doi:10.2528/PIER07052801
32. Méjean C, Pometcu L, Benzerga R, et al. Electromagnetic absorber composite made of carbon fibers loaded epoxy foam for anechoic chamber application. *Mater Sci Eng B*. 2017;220:59-65. doi:10.1016/j.mseb.2017.03.009

33. Nornikman H, Malek F, Soh PJ, Azremi AAH, Ismahayati A. Reflection Loss Performance of Triangular Microwave Absorber. In: *International Symposium on Antennas and Propagation (ISAP 2010)*. ; 2010.
34. Piekarz I, Sorocki J, Slomian I, Wincza K, Gruszczynski S. Experimental Verification of 3D Printed Low-Conductivity Graphene-Enhanced PLA Absorbers for Back Lobe Suppression in Aperture-Coupled Antennas. In: *2018 IEEE-APS Topical Conference on Antennas and Propagation in Wireless Communications (APWC)*. IEEE; 2018:780-782. doi:10.1109/APWC.2018.8503752
35. Adachi S, Hattori M, Kanno F, Kiuchi K, Okada T, Tajima O. Production method of millimeter-wave absorber with 3D-printed mold. *Rev Sci Instrum*. 2020;91(1):016103. doi:10.1063/1.5132871
36. Zhu Y, Liu L, Zhang Y, et al. Development of millimeter-wave EM absorber with homogenization theory. *SN Appl Sci*. 2019;1(5):398. doi:10.1007/s42452-019-0418-3

4.8 Trumpos žinios apie disertantą

Vardas Pavardė: Darya Meisak

Išsilavinimas

2011-2016 m. studijavo Baltarusijos valstybiniame universitete ir įgijo fiziko tyrėjo kvalifikaciją;

2016-2017 m. studijavo Baltarusijos valstybiniame universitete ir įgijo fizinių-matematinių mokslų magistro kvalifikaciją;

2017-2021 m. studijavo Vilniaus universiteto Medžiagų inžinerijos mokslo krypties doktorantūroje.

kontaktams dariameysak@gmail.com

PUBLIKACIJŲ SĄRAŠAS

1. **D. Meisak**, J. Macutkevic, D. Bychanok, A. Selskis, J. Banys, P. Kuzhir, Broadband dielectic properties of Fe_2O_3 H_2O nanorods/epoxy resin composites, Journal of Nanomaterials 2019 (2019), 9756920.
2. **D. Meisak**, J. Macutkevic, A. Selskis, J. Banys, P. Kuzhir, Dielectric properties and electrical percolation in $MnFe_2O_4$/epoxy resin composites, Physica Status Solidi (a) 217(6) (2019), 1900526.
3. **D. Meisak**, J. Macutkevic, A. Plyushch, P. Kuzhir, A. Selskis, J. Banys, Dielectric relaxation in the hybrid epoxy/MWCNT/$MnFe_2O_4$ composites, Polymers 12(3) (2020), 697.
4. **D. Meisak**, E. Gurnevich, A. Plyushch, D. Bychanok, V. Georgiev, R. Kotsilkova, P. Kuzhir, Robust design of compact microwave absorbers and matched loads based on DC-conductive 3D-printable filament, Journal of Physics D: Applied Physics 53(30) (2020), 305301.
5. **D. Meisak**, J. Macutkevic, A. Selskis, P. Kuzhir, J. Banys, Dielectric relaxation spectroscopy and synergy effects in epoxy/MWCNT/Ni@C composites, Nanomaterials 11(2) (2021), 555.

1 publikacija / 1st publication

Broadband dielectic properties of Fe_2O_3 H_2O nanorods/epoxy resin composites

D. Meisak, J. Macutkevic, D. Bychanok, A. Selskis, J. Banys, P. Kuzhir

Journal of Nanomaterials **2019**, 9756920 (2019)

DOI: 10.1155/2019/9756920

https://www.hindawi.com/journals/jnm/2019/9756920/

2 publikacija / 2nd publication

Dielectric properties and electrical percolation in $MnFe_2O_4$/epoxy resin composites

D. Meisak, J. Macutkevic, A. Selskis, J. Banys, P. Kuzhir

Physica Status Solidi (a) **217**(6), 1900526 (2019).

DOI: 10.1002/pssa.201900526

https://onlinelibrary.wiley.com/doi/full/10.1002/pssa.201900526

3 publikacija / 3rd publication

Dielectric relaxation in the hybrid epoxy/MWCNT/$MnFe_2O_4$ composites

D. Meisak, J. Macutkevic, A. Plyushch, P. Kuzhir, A. Selskis, J. Banys

Polymers **12**(3), 697 (2020).

DOI: 10.3390/polym12030697

https://www.mdpi.com/2073-4360/12/3/697

4 publikacija / 4th publication

Robust design of compact microwave absorbers and matched loads based on DC-conductive 3D-printable filament

D. Meisak, E. Gurnevich, A. Plyushch, D. Bychanok, V. Georgiev, R. Kotsilkova, P. Kuzhir

Journal of Physics D: Applied Physics **53**(30), 305301 (2020).

DOI: 10.1088/1361-6463/ab86e6

https://iopscience.iop.org/article/10.1088/1361-6463/ab86e6/meta

5 publikacija / 5th publication

Dielectric relaxation spectroscopy and synergy effects in epoxy/MWCNT/Ni@C composites

D. Meisak, J. Macutkevic, A. Selskis, P. Kuzhir, J. Banys

Nanomaterials **11** (2), 555 (2021).

DOI: 10.3390/nano11020555

https://www.mdpi.com/2079-4991/11/2/555

Vilnius University Press
9 Saulėtekio Ave., Building III, LT-10222 Vilnius
Email: info@leidykla.vu.lt, www.leidykla.vu.lt
Print run copies 17